

The KEDR Detector

V. V. Anashin^a, V. M. Aulchenko^{a, b}, E. M. Baldin^{a, b}, A. K. Barladyan^a, A. Yu. Barnyakov^a, M. Yu. Barnyakov^a, S. E. Baru^{a, b}, I. Yu. Basok^a, I. V. Bedny^a, O. L. Beloborodova^{a, b}, A. E. Blinov^a, V. E. Blinov^{a, b}, A. V. Bobrov^a, V. S. Bobrovnikov^a, A. E. Bondar^{a, b}, A. R. Buzykaev^a, A. I. Vorobiov^a, V. V. Gulevich^a, L. V. Dneprovsky^a, V. N. Zhilich^a, V. V. Zhulanov^{a, b}, G. V. Karpov^a, S. V. Karpov^a, S. A. Kononov^{a, b}, K. Yu. Kotov^a, E. A. Kravchenko^{a, b}, V. N. Kudryavtsev^a, A. S. Kuzmin^a, V. F. Kulikov^{a, b}, E. A. Kuper^{a, b}, E. B. Levichev^{a, c}, D. A. Maksimov^a, V. M. Malyshev^a, A. L. Maslennikov^a, A. S. Medvedko^{a, b}, N. Yu. Muchnoi^a, S. A. Nikitin^a, I. B. Nikolaev^{a, b}, A. P. Onuchin^{a, c}, S. B. Oreshkin^a, I. O. Orlov^{a, b}, A. A. Osipov^a, S. V. Peleganchuk^a, S. G. Pivovarov^{a, c}, A. O. Poluektov^a, G. E. Pospelov^a, V. G. Prisekin^a, V. A. Rodyakin^a, A. A. Ruban^a, G. A. Savinov^a, Yu. I. Skovpen^{a, b}, A. N. Skrinsky^a, V. V. Smalyuk^a, R. G. Snopkov^a, A. V. Sokolov^a, A. M. Sukharev^a, A. A. Talyshev^{a, b}, V. A. Tayursky^a, V. I. Telnov^{a, b}, Yu. A. Tikhonov^{a, b}, K. Yu. Todyshev^a, Yu. V. Usov^a, T. A. Kharlamova^{a, b}, A. G. Shamov^a, B. A. Shwartz^{a, b}, L. I. Shekhtman^a, A. I. Shusharo^a, and A. N. Yushkov^a

^aBudker Institute of Nuclear Physics, Siberian Branch, Russian Academy of Sciences, Novosibirsk, 630090 Russia

^bNovosibirsk State University, Novosibirsk, 630090 Russia

^cNovosibirsk State Technical University, Novosibirsk, 630092 Russia

Abstract—The KEDR detector is a universal magnetic detector designed for studying the c - and b -quarks and two-photon physics, and is employed at the VEPP-4M e^+e^- collider. A specific feature of the experiment is the measurement of absolute beam energy using two methods: the resonant depolarization and the faster but less precise Compton backscattering of laser photons. This allowed a large series of measurements to be performed, in which the accuracy of determination of such fundamental parameters of particles as mass and total and leptonic widths was improved.

DOI: 10.1134/S1063779613040035

INTRODUCTION

The KEDR detector (Fig. 1) has been in operation since 2002 in the energy region $2E = 2\text{--}4$ GeV at the VEPP-4M e^+e^- collider at the Budker Institute of Nuclear Physics (BINP) in Novosibirsk. The VEPP-4M collider has an energy region of 2–11 GeV in the center-of-mass system (the region is unique for the existing e^+e^- colliders), which allows experiments to be conducted both in the low-energy region, where the ψ -meson family and the threshold of τ lepton production are located, and in the high-energy region, where the Y mesons are produced.

Now in the low-energy region, the BES-III detector operates (at $2E = 2\text{--}4.2$ GeV) at the BEPC-II e^+e^- collider with a design luminosity of 10^{33} cm⁻² s⁻¹. The CLEO- c detector that worked in this region at the CESR- c collider with an order of magnitude lower luminosity stopped operating in 2008.

The KEDR detector is comparable in its parameters with the BES-III and CLEO- c detectors; however, the luminosity of the VEPP-4M collider is one to two orders of magnitude below the luminosity of CESR- c and BEPC-II.

In the high-energy region ($\sqrt{s} = 10.58$ GeV), the Belle detector at the B-Factory at KEK continues working with a luminosity of around 10^{34} cm⁻² s⁻¹; the BaBar detector at the B-Factory at SLAC completed data acquisition in 2008. Integrated luminosities of 500–1000 fb⁻¹ were recorded at these detectors.

The KEDR detector includes the following systems: vertex detector, drift chamber, aerogel Cherenkov counters, time-of-flight scintillation counters, barrel electromagnetic calorimeter based on liquid krypton, endcap electromagnetic calorimeter based on CsI crystals, superconductive magnetic solenoid, and muon system (they are shown in Fig. 1), as well as the system of the scattered electrons and positrons tagging (SSET) and the luminosity monitor.

The physics program of the KEDR detector is constructed in such a way that we could benefit from a number of our advantages in comparison with other machines and detectors.

The VEPP-4M collider is equipped with two mutually complementary techniques of precision measuring and monitoring of the beam energy (this has not

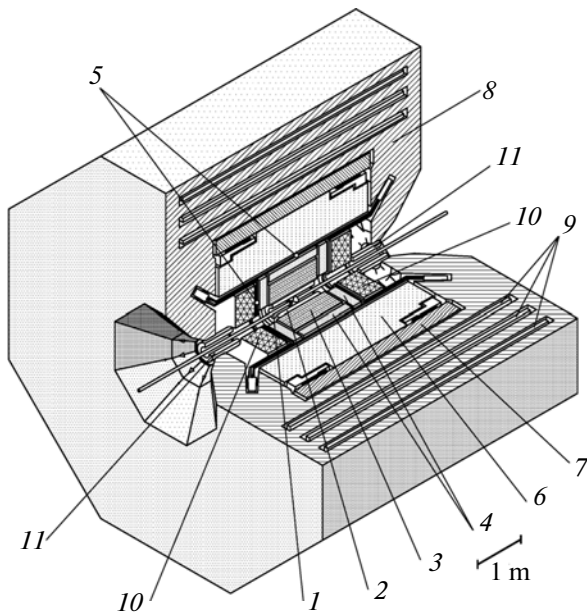


Fig. 1. The central part of the KEDR detector: vacuum chamber of the collider (1); vertex detector (2); drift chamber (3); aerogel threshold Cherenkov counters (4); time-of-flight counters (5); liquid-krypton barrel calorimeter (6); superconductive solenoid (7), magnet yoke (8); muon chambers (9); endcap CsI calorimeter (10); compensating coil (11).

been yet implemented elsewhere in the world): the resonant-depolarization method with a relative accuracy of 10^{-6} and the energy-monitoring method based on measurements of the edge position of the energy spectrum of γ quanta produced at the Compton scattering of monochromatic laser radiation by the electron beam (relative accuracy is 3×10^{-5}). Therefore, a large part of the program consists of precision measuring elementary particle masses, for which the high-precision knowledge of beam energy is important. In the low-energy region, these are masses of the J/ψ , ψ' , $\psi(3770)$, D^0 , D^\pm mesons and of the τ lepton. This program has been completed by now. In the high-energy region, values of Υ mesons may be refined and masses of certain other states will probably be measured.

Another important task is to measure a value of the cross section of $e^+e^- \rightarrow \text{hadrons}$ (of the R quantity) in the energy region $2E = 2\text{--}11$ GeV in a single experiment with a single detector, which has not been performed so far. The region from 5 to 7 GeV is of the greatest interest for R measurements. Earlier it was measured in two experiments: MARK-1 and Crystal Ball. However, the MARK-1 results differ appreciably from the later measurements and they now are considered to be erroneous, while the Crystal Ball result was not published in the reviewed journals. So, in a sense, this energy region remains uninvestigated.

The presence of (i) the electromagnetic calorimeter based on liquid krypton in the detector with a high-

energy resolution and ability of measuring coordinates of the point of the γ -quantum conversion to an accuracy of ~ 1 mm and (ii) the system of the aerogel threshold Cherenkov counters, providing the opportunity to discriminate between the π and K mesons within a range of momenta from 600 to 1500 MeV/c, allows a number of experiments for measuring probabilities of decay of particles of the ψ - and Υ -families to be accomplished, from which the significant physical results may be obtained.

The KEDR detector is equipped with a unique system for detection of scattered electrons and positrons to study the two-photon processes $e^+e^- \rightarrow \gamma^*\gamma^* \rightarrow e^+e^- X$. The system allows the invariant mass $M_{\gamma\gamma}$ of the produced state X to be determined to a relative accuracy $\leq 1\%$ for $M_{\gamma\gamma} = 0.5\text{--}4$ GeV. Due to this, the efficiency of recording the two-photon processes increases by several tenfold as compared with the detectors non-equipped with the similar system. Experiments in two-photon physics are planned to conduct mainly at high energy. Here a substantially lower integral of luminosity can be obtained as compared with the B-Factories. However, owing to the advantage in efficiency of recording of two-photon processes and smaller systematic errors, it is expected that we will be able to measure cross sections of two-photon processes with the comparable or even better accuracy.

A brief description of the KEDR detector was published at the beginning of experiments with it in 2002 [1]. The preprint with the detector description was published in 2010 [2]. In this paper that basically coincides with [2], the detailed description of the design of the KEDR detector systems is presented, and their current state is given. The techniques of precision measurements of the energy of VEPP-4M beams are also described.

1. VEPP-4M. MEASURING OF BEAM ENERGY

The VEPP-4M electron-positron collider (Fig. 2) is designed for experiments in high-energy physics, photo-nuclear studies and experiments with synchrotron radiation [3–5].

The VEPP-4M collider is the updated version of VEPP-4 with beam energy from 1 to 5.5 GeV. The facility operates in the mode of 2×2 bunch. Two pairs of dipole magnets located in the experimental straight section and the quadrupole lenses of final focus installed near the intersection region of the electron and positron beams form the high-resolution strong focusing spectrometer for the SSET of the KEDR detector. Two dipole wigglers to control the beam size are set symmetrically at the ends of experimental straight section. In the technical straight section, there are two gradient wigglers installed at the points with zero dispersion to control decrements of damping.

Basic parameters of the VEPP-4M collider are presented in Table 1. The design parameters of the VEPP-4M beam are given in Table 2.

1.1. Measuring Beam Energy Using the Resonant Depolarization Method

The method of resonant depolarization (RD) is used for precision measurements of beam energy at the VEPP-4M, which was proposed and first implemented at the BINP in the 1970s [6, 7]. Since then, it is widely used at the BINP and other world laboratories. The RD method, the basis of which is the precision measurements of the spin precession frequency Ω , is the most accurate method of absolute calibration of beam energy in the e^+e^- storage ring. In brief, its essence is as follows.

A mean frequency of spin precession around the direction of the guiding magnetic field in the storage ring with a planar orbit is given by the expression

$$\Omega = \omega_0 \left(1 + \gamma \frac{\mu'}{\mu_0} \right), \quad (1)$$

where ω_0 is the revolution frequency; μ'/μ_0 is the ratio of the anomalous part of the electron magnetic moment to its normal part; γ is the relativistic factor. With introduction of the external electromagnetic field with the frequency Ω_d satisfying the condition of external spin resonance

$$\Omega \pm \Omega_d = n\omega_0 \quad (n \text{ is any integer}),$$

the depolarization occurs. The fact of depolarization can be established by recording a suitable polarization-sensitive process. Introducing the normalized spin frequency

$$\nu = \frac{\Omega}{\omega_0} - 1 = \gamma \frac{\mu'}{\mu_0},$$

we derive from (1) the expression for the beam energy E_b :

$$E_b [\text{MeV}] = \nu \frac{m_e c^2}{(\mu'/\mu_0)} \quad (2)$$

$$= (440.648428 \pm 1.1 \times 10^{-5})\nu,$$

where the values of μ'/μ_0 and electron mass in MeV [8], known to high precision, are substituted: $\mu'/\mu_0 = 1.15965218073 \times 10^{-3} \pm 2.8 \times 10^{-13}$ and $m_e c^2 = (0.510998910 \pm 1.3 \times 10^{-8}) \text{ MeV}$.

From (2) the principle possibility follows to find the particle energy from the measured spin precession frequency with a limiting relative accuracy of 2.5×10^{-8} . It is important to note that it is not necessary to accurately measure the absolute value of the frequency Ω , but only ν , which is its ratio to the frequency ω_0 .

When the particle moves in the collider ring, its magnetic moment is precessing around the magnetic

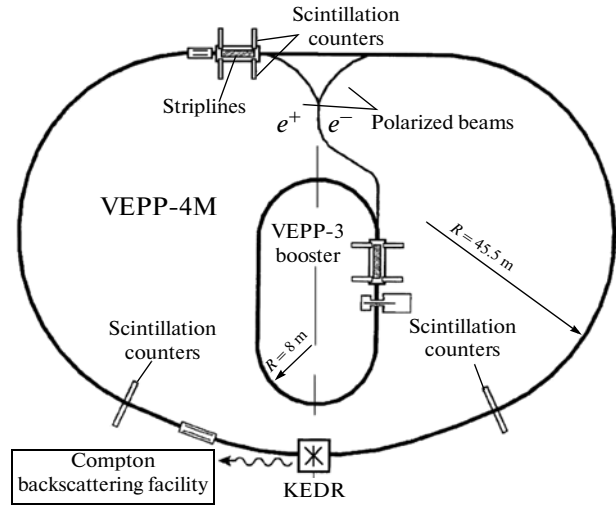


Fig. 2. The VEPP-4M layout with equipment for measuring beam energy.

field vector and the magnetic moment component that is orthogonal to the field reduces due to the magnetic-dipole radiation. As a result, the spin orients itself along the magnetic field (the Sokolov–Ternov effect). The characteristic polarization time in the approxima-

Table 1. Main parameters of VEPP-M [5]

Circumference	366 m
Revolution frequency	818.924 kHz
Betatron tunes, horizontal/vertical	8.54/7.57
Orbit compression factor	0.0168
Natural chromaticity, horizontal/vertical	-14.5/-20.3
Aperture at semi-rings, $2A_x \times 2A_y$	60 × 30 mm ²
Lattice functions at the intersection region $\beta_x/\beta_y/\eta_x$	75 cm/5 cm/80 cm

Table 2. Calculated parameters of VEPP-4M beam [5]

Beam energy E_b , GeV	1.5	1.8	4.0	5.5
Synchrotron frequency	0.011	0.012	0.017	0.021
Horizontal emittance, nm rad	17	25	121	230
Energy spread $\sigma_E/E_b \times 10^4$	2.5	2.9	6.6	9
Energy loss per turn, keV	14	29	173	2550
Bunch length, cm	5	5	5	5
Damping time (horiz./vertic.), ms	260/130	150/75	13.8/6.8	5.3/2.6

tion of a circular orbit with the radius R in the homogeneous magnetic field is [9]

$$\tau_{\text{pol}} [\text{s}] = \frac{8\sqrt{3}}{15} \frac{R^3}{\gamma^5 \lambda_e c r_0} \approx \frac{2.8 \times 10^{18} R^3 [\text{m}]}{\gamma^5}, \quad (3)$$

where $\lambda_e = 3.86 \times 10^{-11}$ cm is the Compton wavelength of the electron, $r_0 = 2.82 \times 10^{-13}$ cm is the classical electron radius, c is the speed of light.

In the VEPP-4M collider ring, $\tau_{\text{pol}} \approx 100$ h at the energy $E = 1.8$ GeV. However, the VEPP-3 booster storage ring with the substantially smaller orbit radius R and the polarization time around half an hour at 1.8 GeV allows one to obtain the polarized beams which are then injected and used in VEPP-4M.

At VEPP-4M in the beam-energy region below 2 GeV, the effect of intra-bunch scattering of particles (the Touschek effect) is used for registration of the fact of depolarization [10]. A counting rate of scattered particles, which is dependent of spin, is measured by three pairs of scintillation counters [7]. Two pairs are installed at the ends of the experimental straight section, while one pair is in the technical straight section (see Fig. 2). The counters of each pair are introduced inside the aperture in the horizontal plane from both sides and record the Touschek electrons scattered along the ring circumference. Two electrons during the act of scattering acquire momentum increments that are equal in magnitude but opposite in sign and, as a result, begin moving along the trajectories deviated symmetrically in the median plane from the closed orbit. The counting rate of scattered particles is equal approximately to [11]

$$\dot{N} \approx \frac{\sqrt{\pi} r_0^2 c N_b^2}{\gamma^5 V_b (c \sigma_p / E_b)^3} (a + b \zeta^2); \quad (4)$$

$$a, b = a, b(\varepsilon_1, \varepsilon_2); \quad \varepsilon_{1,2} = [\Delta p_{1,2} / (\gamma \sigma_p)]^2;$$

$$\Delta p_1 = \Delta p_1(A); \quad \Delta p_2 = \Delta p_2(A_g).$$

Here N_b is the number of particles in the bunch; V_b is the bunch volume; σ_p is the spread of the transverse momentum in the beam; ζ is the beam polarization degree; a and b are the calculated functions depending on the lower (Δp_1) and upper (Δp_2) limits for momentum transfer, in this case $b < 0$; A is the distance from the counter to the orbit; A_g is the geometric aperture of the storage ring along the radius.

Under our conditions, the intra-bunch scattering dominates over processes of scattering by the residual gas in the VEPP-4M vacuum chamber. More than 60% of the load of counters is due to Touschek particles. Therefore, there is no particular need to suppress the uncorrelated background. Additionally, the use of the total counting rate allows the statistical error to be reduced. With a current of 1 mA per bunch, the count-

ing rate in two pairs of counters in the experimental straight section reaches 2 MHz.

As a result of depolarization, a relative increase in the counting rate of scattered electrons by the quantity $|b\zeta^2/a|$ occurs (the electric repulsion of electrons in the polarized bunch during the scattering is relaxed due to their magnetic interaction, which reduces the intensity of Touschek particle yield within a fixed interval or finite momenta). The polarization contribution to the counting rate is proportional to the square degree of polarization. It drops as the beam energy increases and also as its vertical size grows [11–13]. A change in the counting rate at VEPP-4M is 1–3% in different cases. To decrease the effect of the beam-position instabilities, its sizes and lifetime, a ratio between the scattered-electron counting rates of the polarized (W_1) and non-polarized (W_2) bunches that are separated in time by half-period of revolution is measured:

$$\delta = 1 - W_2/W_1.$$

The beam depolarization is performed using a pair of matched conductive strips spaced vertically inside the vacuum chamber. The travelling TEM wave is created, which propagates towards the beam to be depolarized. A wave frequency is linearly rearranged in the band that involves the expected value of frequency of the external spin resonance.

According to the other option of connection of the strips to the rf generator, the depolarizer acts on electrons and positrons using the alternating transverse magnetic field created by a current passing through the strips.

A sinusoidal signal of the depolarizer is generated by the precision synthesizer [14] developed at the BINP, with which a resolution in the frequency rearrangement step of 10^{-4} Hz is achieved. The Ch1-69 rubidium frequency standard with an accuracy of 10^{-10} serves as a reference generator for the synthesizer and simultaneously for the rf system of VEPP-4M. This ensures the stability of the revolution frequency $\Delta\omega_0/\omega_0 \sim 10^{-10}$ and quite sufficient stability of the beam energy in periods between calibrations using the RD method, which is connected with the stability $\Delta\omega_0/\omega_0$. In addition to that, the matching of depolarizer frequencies and the revolution frequency to the unified standard during the calibration excludes the differently directed drift of these frequencies and the appearance of a systematic error in energy determination.

The forced resonant depolarization in the RD method takes much time as compared with periods of orbital motion. Therefore an error of measuring the mean spin frequency $\langle v \rangle$ is much less than a value of instantaneous spread of spin frequencies ($\sigma_v \sim 5 \times 10^{-4}$), which arises due to the particle energy spread in the beam ($\sigma_E \sim 1$ MeV). Consequently, an error of measuring the mean energy of particles $\langle E \rangle$ that corre-

sponds to $\langle v \rangle$ is much less than the energy spread of the beam σ_E .

A limiting accuracy of absolute calibration of beam energy using the RD method is determined by the intrinsic thickness of spin line ε_v . Its value is connected with the averaging of spin motion over the synchrotron and betatron oscillations and may differ appreciably from zero due to the square nonlinearity of the guiding field. Taking into account the sextupole correction of the guiding field at VEPP-4M, the value $\varepsilon_v \sim 5 \times 10^{-7}$, which corresponds to the limiting accuracy of the beam energy calibration, is around 1 keV.

Figure 3 displays a typical time diagram of relative counting rate of Touschek electrons in scanning the depolarizer frequency. A scanning rate in energy units is 0.3 keV/s. Amplitude of the signal on strips is several tens of volts. The calculated depolarization time is ~ 1 s. An accuracy of the mean energy determination in a single measurement from fitting the depolarization jump is $\sim 10^{-6}$ (around 2 keV), which is substantially better than the relative energy spread in a beam $\sigma_E/E_b \sim 5 \times 10^{-4}$. Since calibrations are conducted between the runs for data acquisition, the interpolation leads to the error 7–30 keV in the mean beam energy that is assigned to the experimental run.

1.2. The Compton Monitor of Energy and Energy Spread

In addition to the RD method at the VEPP-4M collider, the method of routine monitoring of beam energy and energy spread in the process of data taking is implemented, in which the Compton backscattering is used [7, 17, 18].

The principle of operation in the method is based on measuring the position and width of the spectrum edge of Compton γ -quanta produced in the scattering of monochromatic laser radiation on the electron beam. During the scattering of laser photons at the energy ω by the colliding electron beam at the energy E_b , the backscattered γ quanta form the energy spectrum with the shape shown in Fig. 4 (narrow peaks in the spectrum are related to the irradiation of the detector by isotopes for the energy scale calibration). As it can be seen from Fig. 4, the scattered photons at the maximum energy ω'_{\max} form a sharp edge in the energy spectrum. The electron-beam energy is connected with the value ω'_{\max} by the simple relationship

$$E_b = \frac{\omega'_{\max}}{2} \left(1 + \sqrt{1 + \frac{m_e^2 c^4}{\omega \omega'_{\max}}} \right). \quad (5)$$

A visible width of the measured spectrum edge is caused mainly by the energy resolution of the photon detector and the energy spread of electrons in a beam. Thus, by measuring the energy spectrum and finding the edge position, it is possible to obtain the electron-

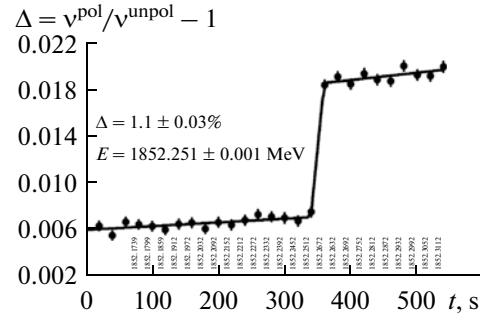


Fig. 3. Resonant depolarization. An accuracy of energy determination is $\sim 10^{-6}$. Time of measurements is 9 min.

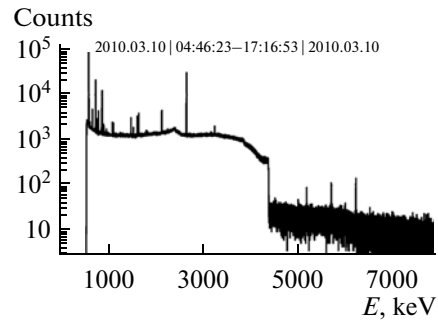


Fig. 4. Spectrum of the Compton γ quanta measured by the HPGe detector in 2010. The beam energy is 1553.5 MeV. Acquisition time is 2.5 h.

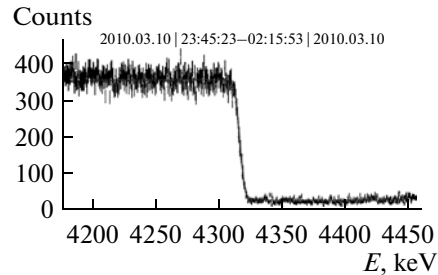


Fig. 5. Fragment of spectrum given in Fig. 4 (in the vicinity of ω'_{\max}), the line is the result of fitting. The measured beam energy is 1553.466 ± 0.018 MeV. The energy spread of the beam is 505 ± 25 keV.

beam energy. A value of beam-energy spread is determined using the measured width of the spectrum edge and the energy resolution of the detector.

The COHERENT GEM Select 50 infrared CO_2 laser with the photon energy $\omega = 0.117065223$ eV was chosen as a source of monochromatic radiation. With a change in the electron-beam energy from 1.5 to 2 GeV, a value of ω'_{\max} falls in the range of 4–7 MeV. An energy spectrum of scattered photons (Fig. 5) is measured by the coaxial detector made of super-pure germanium with an active volume of 120 cm^3 and the

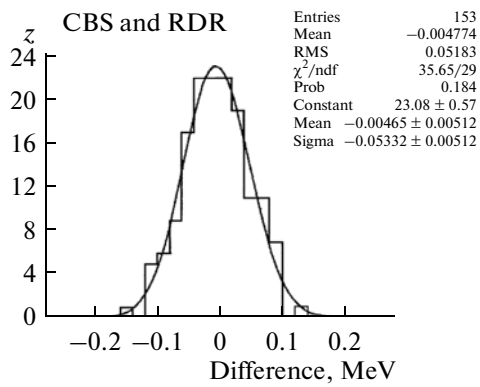


Fig. 6. Histogram of difference of energy values measured using the Compton backscattering (CBS) method and the RD method at beam energy of 1.7–1.9 GeV, $\sigma = 53.3 \pm 1.5$ keV.

full absorption efficiency around 5% for the 6-MeV γ -quanta.

For a single measurement (during 20–40 min), a statistical accuracy of the electron-beam energy is $\approx 3 \times 10^{-5}$ while an accuracy of the energy-spread determination is around 12%. In order to assign the energy to a run, several measurements are summed. For absolute calibration of energy scale of the germanium detector and its energy resolution, the acquisition of etalon lines of the gamma-active isotopes at energies from 0.6 to 6.13 MeV is performed simultaneously with the Compton spectrum accumulation.

The systematic error of the method was estimated by comparing of results of the measurements with the beam energy measured using the RD method. During

the experiment for measuring the tau-lepton mass, 153 simultaneous energy measurements were taken using two methods; the histogram of differences of the measured values is shown in Fig. 6. The excess of the distribution width in Fig. 6 (50 keV) over the mean statistical error of measurements in these runs (30 keV) enables the systematic error of the method to be estimated at a level of 40 keV or 2.5×10^{-5} of the electron-beam energy. A basic source of the systematic error, most probably, is the instability of the orbit position of the electron beam in the region of interaction with the laser radiation.

2. MAGNETIC SYSTEM

The magnetic system consists of one main and two identical compensating superconducting solenoids (Fig. 7 and Table 3) located inside the iron yoke [19].

2.1. Main Solenoid

The constant homogeneous magnetic field of 0.6 T along the beam trajectories in the detector is created by the main superconducting (SC) solenoid 1.84 m long with an inner diameter of 3.24 m and a thickness of 4.5 mm (14 mm, taking the bandage into account).

The SC winding of the main solenoid comprises 568 turns of the SC cable with rectangular section 1.6×3.8 mm. It is formed out of eight (twisted and soldered along the entire length in the 2×4 configuration) NbTi/Cu wires 0.85 mm in diameter with a superconductor-to-copper ratio of 2 : 3, each containing 2970 NbTi filaments. The turns are laid in pairs into the helical groove with a size of 3.5×4.5 mm,

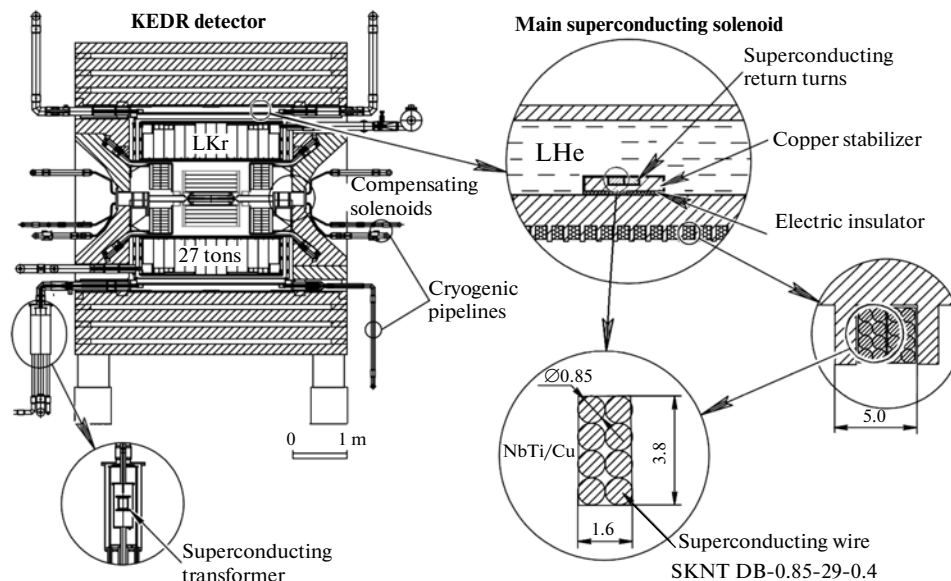


Fig. 7. Construction of superconductive solenoid.

Table 3. Parameters of SC solenoids of the KEDR detector

Parameter	Central solenoid	Compensating solenoid
Magnetic field (operating)	0.6 T	2.2 T
Magnetic field (design)	1.83 T	6.55 T
Ratio I/I_c	0.56	0.45–0.46
Current (design)	8 kA	292 A
Stored energy (design)	39 MJ	124 kJ
Number of winding layers	1 + 1 (return turns)	17
Number of turns	560 + 8 (return)	7726
Inductance	1.22 H	2.9 H
Winding thickness	4.5 mm	15.7 mm
Winding length	2.84 m	0.433 m
Cryostat length	3.16 m	0.560 m
Outer cryostat diameter	3.57 m	0.246 m
Inner cryostat diameter	3.12 m	0.120 m
Inner diameter of SC winding	3.24 m	0.146 m
Total mass of coil with cryostat	12000 kg	90 kg
Mass of helium vessel with winding	7000 kg	–
Coil radiative thickness	$0.95X_0$	–
E/M (design)	7.8 MJ/kg	–
Inductance of return turns	0.28×10^{-3} H	–
Resistance of shunting of turns	6×10^{-6} Ω	–

which is turned down with a pitch of 5 mm outside the inner wall of the ring-shaped helium vessel made of stainless steel, and soldered with the POS-61 solder.

The metallic housing of the helium vessel is a banded for the winding and, at the same time, it ensures the distributed electric shunting of each turn of it, protecting it in case of a quench from destruction by the stored energy of magnetic field, which releases in the form of the heat.

The return turns of the main SC solenoid are soldered into the massive copper bus fastened at the insulators inside the helium vessel. These turns are cooled directly by liquid helium whereas the main winding turns are cooled through the 10-mm wall of the helium vessel made of the stainless steel.

The helium vessel has a vacuum-tight thermal insulation and a heat shield made of aluminum foil with a copper tube welded to it for liquid-nitrogen circulation.

2.2. Power Supply of the Main Solenoid

The power supply of the main SC solenoid consists of a SC transformer and two SC temperature-controlled cables (resistive switches) forming the computer-controlled full-wave rectifier. An advantage of this design is its compactness, low cost, ability to

ensure input, output, and stabilization of the magnetic field with the relative accuracy of 10^{-4} .

On completion of low-energy experiments, it is planned to increase the working value of magnetic field in the KEDR detector up to 1 T due to using new SC switches. The higher magnetic field need to provide experiments at the higher energy of VEPP-4M beams without losing efficiency.

2.3. Compensating Solenoids

The purpose of compensating solenoids is to reduce to zero the magnetic field integral along the beam motion trajectory in the detector.

The magnets are located at the centers of the yoke poles. The VEPP-4M vacuum chamber united with the vacuum heat-insulating cavities of its cryostats, ensuring the part of surface of its helium vessels for additional cryosorption pumping out.

The winding of the compensating solenoid comprises two identical multi-layer coils connected in series. For winding the coils, the NbTi/Cu wires are used with a diameter of 1.0 mm (inner layers) and 0.7 mm (outer layers).

The DC current is supplied through the resistive current leads designed as the cells of tubes soldered side by side for a current up to 300 A. (Similar current

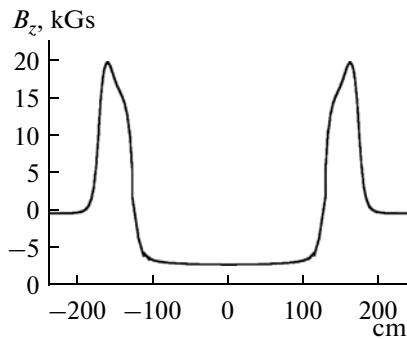


Fig. 8. The magnetic field z -component along the detector axis (computation).

leads tubes are also used for power supply of the main SC magnet.)

The compensating solenoids have been successfully tested up to the design value 6.55 T. Now they are operated with a working current of 98 A, which corresponds to the 0.6 T main solenoid field.

2.4. Yoke

The iron yoke with a mass of 740 tons closes the magnetic flux of the main solenoid, ensuring the homogeneity of the magnetic field inside the detector.

The yoke consists of eight sections, embracing the detector in the form of a regular octahedral prism, and two cylindrical poles. A section presents a set of parallel iron plates with air gaps between them, which are intended for arrangement of muon chambers.

Thus, the yoke serves as a supporting frame for all detector components and performs a function of an absorber for muon chambers.

2.5. Monitoring of Magnetic Field

The magnetic field in the detector is measured with an accuracy of 10^{-5} by two NMR sensors located on the right and the left of the intersection region near the VEPP-4M vacuum chamber [2].

Readings of these sensors are used for stabilizing the magnetic field in the detector during the experiment.

To measure the magnetic field in the area of the detector drift chamber, 12 Hall probes are arranged near it, which measure the radial and axial field components with an accuracy of 5×10^{-4} .

Ten Hall probes with an accuracy 10^{-3} monitor the radial and axial field components in the immediate vicinity of the main solenoid, with being located above and below the upper wall of its cryostat (outside).

Figure 8 displays the result of calculation of the field z - component (the computation was performed using the Mermaid3d code [20], with a current value in the compensating solenoids of 105 A).

3. CRYOGENIC SYSTEM

The cryogenic components of the KEDR detector include (i) the central electromagnetic calorimeter, filled with 27 tons of liquid krypton, and (ii) SC solenoids of the magnetic system, cooled with liquid helium.

A working temperature of the liquid-krypton calorimeter is near 119.5 K, while the temperature of the SC magnetic system is 4.5 K. Both systems work under normal pressure and in the mode without drainage in the atmosphere.

Liquid nitrogen (a working temperature is 85 K), the reserve of which (up to 101 000 kg) is stored in two tanks and supplied under the excess pressure up to 0.5 MPa.

Liquid nitrogen is mainly used for cooling the vacuum shields of cryostats and nitrogen heat-exchangers.

Gaseous nitrogen, warmed up to the ambient temperature, is used for forced cooling the drift chamber from outside, which significantly improves its characteristics.

One of the two identical nitrogen tanks is constantly used as a working accumulator-distributor of liquid and gaseous nitrogen, whereas another serves for liquid nitrogen accumulation from transported tanks and for the liquid subsequent expelling into the operating tank via the transfer line of the liquid nitrogen supply. This technique makes it possible to prevent the diffusion of oxygen from the atmosphere into the gaseous volume of the working tank and further into the drift chamber environment. Its second advantage is the possibility of non-interrupted delivery of liquid and gaseous nitrogen to consumers in any modes of nitrogen system.

Five identical storages (three upper and two lower ones relative to the calorimeter) are provided for accumulating, storing, and delivering liquid krypton. These are cryogenic vessels, each with a working pressure of 0.6 MPa and a volume of 8 m^3 (filling with liquid up to 6 m^3). All storages are equipped with nitrogen heat-exchangers for condensation of gaseous krypton on them and with evaporators for self-pressurization and displacement of liquid krypton to the distributing collector.

A ring-shaped cylindrical krypton vessel of the calorimeter is made of aluminum alloy and designed for the working and excess pressures up to 0.03 MPa. Therefore liquid krypton is supplied to it from the upper storages and evacuated into the lower storages by the force of gravity.

The krypton system is equipped with a regenerated unit for purifying gaseous krypton from electrically negative impurities (oxygen) [21]. The needed purity is 1 ppm (10^{-6}).

Thermostating of the calorimeter is ensured by the periodic supply of liquid nitrogen to the heat-

exchanger welded on the top surface of aluminum housing of the calorimeter's krypton vessel.

Absolute working pressure is sustained in the calorimeter within a range of 0.105–0.120 MPa, with temperature varying in the 118.5–120.5 K interval.

For thermostating of SC magnets, the satellite helium refrigerator is applied with the cooling power of 600 W at the temperature of 4.5 K, which works according to the mean pressure cycle (2.5 MPa) with the excess reverse flow and liquid helium injection from the exterior source in amounts of 4–10% of the circulation flowrate. The helium refrigerator's compressor and gas-holders are installed at the cryogenic plant that is 600 m apart from the detector.

The reserve up to a level of 2 m³ of liquid helium is accumulated permanently in the horizontal-ring-shaped vessel of the special helium cryostat with liquid helium produced by liquefiers at the cryogenic plant and delivered in Dewar vessels with auto transport. Above the liquid helium's level in the cryostat, there are three pairs of the current leads, stored inside separated channels (tubes) and cooled by helium vapors. Each channel used to supply one of SC magnets with liquid helium by the force of gravity. For guaranteed cooling of the current leads, helium vapors are circulated through them forcibly due to pumping out by an ejector pump with individual control valves above each channel.

The cold helium vapors from the SC magnets make their way to the refrigerator, where their enthalpy is used for cooling the incoming (direct) flow of gaseous helium with a mass flowrate of 80–100 kg/h. The reverse helium flow from the refrigerator (under the pressure no more than 0.07 MPa and at the temperature above 0°C (273 K)) enters in gas-holders of the cryogenic plant, passes through the cryogenic purification units and again is involved by the compressor in the working cycle.

A total daily consumption of the exterior liquid helium in the system amounts to 1100 L when the refrigerator operates in the throttling mode. Due to utilization of a piston-type expander, the flowrate reduces to less than 500 L per day.

Cryogenic pipelines, tanks, and original cryostats have the vacuum-tight thermal insulation. The protective vacuum for krypton calorimeter (no worse than 10⁻³–10⁻⁴ Pa) is ensured by continuous work of the magnetic-discharge pump at the 2 × 10⁻⁴ Pa level. Vacuum no worse than 7 × 10⁻³ Pa for helium objects is created using turbomolecular pumps and aggregates.

Control of cryogenic systems is performed remotely using a personal computer with the Linux operating system and the electronic equipment of our production in CAMAC and VISHNYa crates. The facility comprises more than 300 sensors (of pressure, flowrate, level, temperature, coordinates, position, etc.) and 100 valves of different types.

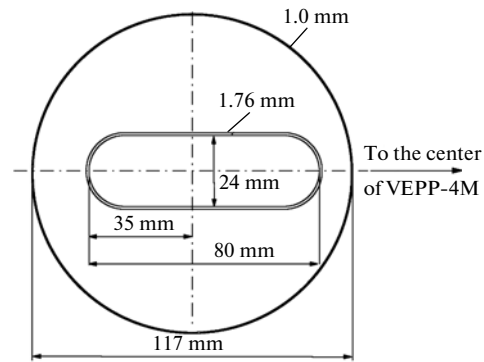


Fig. 9. Layout of the vacuum chamber inside the detector.

The important contribution to the cryogenic system development was made by specialists of the Moscow-region enterprise OAO Kriogenmash (Balashikha, Moscow region) [22].

4. VACUUM CHAMBER

The VEPP-4M vacuum chamber (VC) in the beam intersection region consists of two parts: the inner chamber, having a rectangular section with curves, and the outer barrel chamber (Fig. 9).

For reducing the multiple Coulomb scattering, both parts of the chamber are made of beryllium. The wall thickness of the inner chamber is 1.76 mm; that of the outer chamber is 1 mm. The transverse sizes of the inner chamber are 24 × 80 mm; the outer chamber diameter is 117 mm. A length of beryllium part of the inner chamber is 250 mm; that of outer chamber is 600 mm.

The inner chamber is shifted relative to the outer chamber in the direction to the center of the VEPP-4M ring by 5 mm. The vacuum chamber is wrapped outside with a stainless-steel foil 100 μm thick coated with a 10 μm thick tin layer. All these measures serve for reducing the background from the synchrotron radiation.

Such a VC design is intended for installing between its inner and outer parts the micro-vertex detector based on micro-strip silicon plates. To ensure the sufficient cooling of micro-vertex detector, the space between its inner and outer chambers is filled with the air under atmospheric pressure. Later it was decided not to install the micro-vertex detector in the KEDR detector.

A total VC thickness for a normal incident particle is 1.4% of X_0 .

5. VERTEX DETECTOR

5.1. Construction

The vertex detector (VD) is located between the vacuum tube of the storage ring and the drift chamber and covers a solid angle up to 98% × 4π. Main geomet-

Table 4. Main parameters of the vertex detector

Solid angle	$0.98 \times 4\pi$
Tube diameter	10 mm
Length of sensitive region	670 mm
Anode wire (W)	20 μm
Radius of first layer	67.1 mm
Radius of last layer	116.84 mm
Number of layers	6
Total number of tubes	312

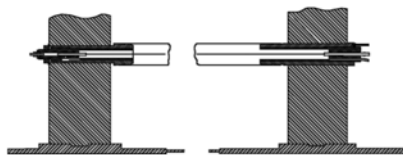
ric VD parameters [23–26] are given in Table 4. For increasing an efficiency of the track registration, the neighboring VD layers are laid with a half-step offset.

The drift tube consists of a cylindrical cathode and a central anode wire fixed in the end plugs by means of crimping in pins. An internal volume of each tube is flushed independently by the working gas mixture. The tubes operate in the proportional mode and make it possible to measure a distance from the charged-particle track to the tube center by means of the measuring of the ionization drift time.

The tube cathode is made of single-layer aluminized mylar 20 μm thick with a thickness of aluminum of 0.1 μm . A peculiarity of this VD construction is a small amount of material on the way of a particle. Owing to the fact that the tubes themselves can withstand the excess pressure, there is no need for an additional sealed volume that increase of the amount of material in the detector. A total thickness of VD material is around 0.2% of X_0 , which is significantly less than the substance thickness of the vacuum chamber.

The tubes are made of the aluminized mylar film with a width of 5 cm, which is first wound as a spiral on the mandrel, before the joints are welded using the ultrasonic tool. The tube keeps tightness under excess pressure up to 3 atm. A construction of the VD drift tube is shown in Fig. 10. The mylar tube is attached to plugs that ensure the tube fixation in the VD flange. Pins for the anode-wire and also gas outlets are pressed into the plug. The gold-plated wire of tungsten-rhenium alloy 20 μm in diameter is used as anode.

Structurally the VD consists of two detachable semi-cylinders. The tubes are fixed in the flanges in the form of semi-rings, which are attached to the vacuum chamber of the storage ring (Fig. 11). A flange

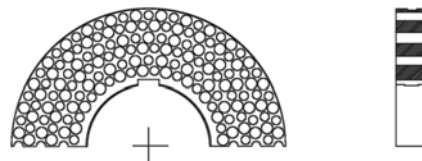
**Fig. 10.** Construction of the VD drift tube.

thickness is 28 mm, which ensures a sufficient depth of mounting holes for plugs and the stability against the moment of forces that arise during the stretching of the tubes. All the tubes are fixed in the flanges independently; the gas is fed in each tube individually. The VD construction provides for the possibility of individual replacement of each tube. The cylindrical form of the tubes is ensured due to an accurate fit of plugs in the flanges and the additional axial stretching of the tubes. The mobile fixation of tubes in the flanges enables the required tube tension. A high voltage supply, signal readout from the anode wire, and grounding are performed individually for each tube too.

Argon with addition of 30% CO_2 under excess pressure of around 0.1 atm is used as a working gas mixture in the VD. For this gas mixture almost in the entire tube volume, the drift velocity of ionization electrons is within the saturation region and weakly depends on the electric field strength, temperature, and pressure. This eliminates main sources of systematic errors in the measured coordinate. The used mixture contains no inflammable components, which simplifies the gas system and makes operation of the detector safer. The disadvantage of this mixture is the impossibility of reaching the spatial resolution better than 100 mm due to the strong electron diffusion.

A gas system with components mixing in the flow is used to ensure the stable gas supply for the VD. A part of the gas system, which provides for the necessary concentration of the mixture components, consists of (i) two high-pressure (argon and carbon dioxide) manifolds, to which up to three 40-l bottles with the purified gas-mixture components can be connected, (ii) the pressure reducers that decrease pressure down to 1–2 atm, (iii) the gas flow controllers of the Bronkhorst company, which provide a constant flow rate of mixture components, and (iv) the mixing reservoir. The gas mixture is supplied via the manifold to collectors located on the outer surface of the KEDR detector. Each drift tube is connected to the collector by means of a teflon pipe 4 m long with inner diameter of 1 mm. If necessary, this construction enables to disconnect the failed tubes from the gas flow without disassembly of the detector.

The gas flow from the VD outlet is supplied to the gas-flow meter and then to the absolute-pressure stabilizer that sustains the constant gas pressure in the VD. The gas mixture is exhausted from the stabilizer

**Fig. 11.** A flange of the vertex detector.

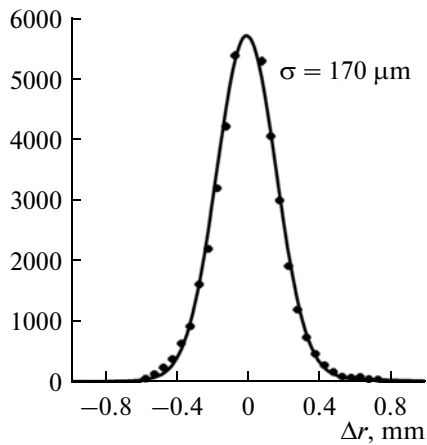


Fig. 12. The VD spatial resolution for cosmic particles.

outlet to the atmosphere through the oil bubbler in order to exclude the oxygen back-flow into the detector. Additionally, parts of the inlet and outlet flows enter the gas-mixture monitors for checking a gas gain and the mixture quality. The monitors present the tubes irradiated by γ -quanta from the ^{55}Fe isotope, which are similar to the tubes used in the VD. A gas gain is measured from the amplitude spectrum of signals of the monitors, and the mixture quality is checked.

5.2. Spatial Resolution

For the track reconstruction using the information from VD, it is necessary to know the dependence of the drift distance on the drift time $R(t)$, as well as the pedestals t_0 for each channel corresponding to the zero drift distance.

A calibration procedure was developed, which can be performed using both the data collected at VEPP-4M storage ring and the specially recorded statistics of cosmic muons.

While working with cosmic tracks at the VD, a spatial resolution of around $170\ \mu\text{m}$ was achieved (Fig. 12) with the gas gain of nearly 10^5 and the efficiency of operation of a single tube more than 99%.

During the work in the detector, the data from the VD are processed together with the drift-chamber data for reconstruction of charged-particle tracks. In addition to that, the information from the VD is used for forming the decision of the second-level trigger, which significantly suppresses the background.

5.3. Electronics

The system of VD data readout consists of (i) the chamber electronics, (ii) the pulse shapers performed in the VISHNYa standard, (iii) the digitizing electronics in the KLUKVA standard, and (iv) the circuits of control and high-voltage supply in the CAMAC stan-

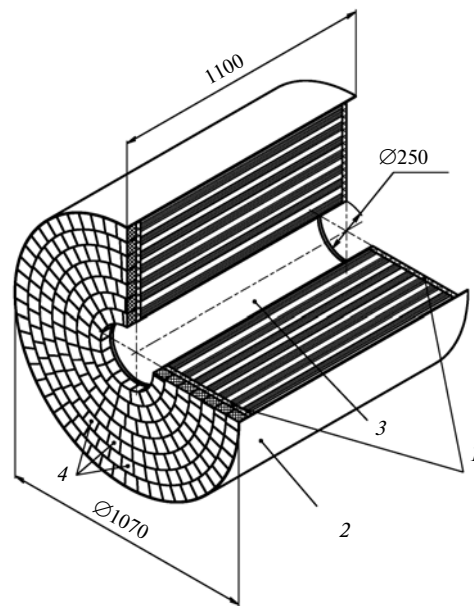


Fig. 13. Layout of the drift chamber: end plates (1), external cowling (2), internal cowling (3), and preamplifiers (4).

dard [27]. Each anode wire is connected to a preamplifier installed directly on the chamber. The preamplifiers are combined in units by 8 channels; each unit is connected via a cable 12 m long with an amplifier-shaper (AS). Two preamplifier units are plugged to a single AS block. An AS block consists of an amplifier and a discriminator connected to its output, which forms a logic signal. Then the signal enters the digitizing logics that measures the time between the AS activation and the delayed signal of the trigger.

6. DRIFT CHAMBER

Main requirements to the drift chamber (DC) are determined by physical problems; the KEDR detector was created in order to solve these problems [1, 28, 29]. These requirements include (i) a good momentum resolution in the design magnetic field of 1.8 T with a small measurement base ($L = 370\ \text{mm}$); (ii) detection and measuring particle momenta within a large solid angle; (iii) a good discrimination of particles from the measurement of ionization losses in the chamber; (iv) a small amount of substance before the calorimeter; and (v) the minimum number of electronic channels.

6.1. Construction

The drift chamber of the KEDR detector [30–34] has a cylindrical shape and occupies the space confined with two cylindrical cowlings 1100 mm long and with two end plates (Fig. 13). The internal cowling 250 mm in diameter is made of carbon-fiber composite 1.5 mm thick for reducing the multiple Coulomb scattering during the combined measurements of

Table 5. Main parameters of the drift chamber

Solid angle	$0.72 \times 4\pi$
Inner radius	125 mm
Outer radius	535 mm
Length	1100 mm
Wire length	970 mm
Number of superlayers	7:
axial	4
stereo	3
Stereo angle	± 100 mrad
Number of measurements	42
Number of cells	252
Number of wires	16032:
anode	1512
field and focusing	11772
screening	2748

momentum using the vertex detector and the drift chamber. The external cowling 1070 mm in diameter is made of glass-fiber laminate 5 mm thick. On inner surfaces of the cowlings, the foil-clad glass-fiber laminate 0.1 mm thick is glued, to which a high voltage is supplied to equalize fields in the DC edge layers and to reduce a distance between the last layers of cells and the cowling. The DC parameters are given in Table 5.

The wires are stretched between two end plates of glass-fiber laminate 20 mm thick. The rms deviation of

wire positions from the design value in both coordinates do not exceed 20 μm . A total wire tension applied to the end plates is 3.4 tons. Maximum bending flexure of the end plates under this load is 1.5 mm; the elongation of the wires is of the same order of magnitude. On completion of stretching of the wires in the DC, their tensions were measured; a spread did not exceed $\pm 5\%$ of the nominal value. A thickness of substance in the DC for a normal particle is 5.1% of X_0 .

6.2. Selection of a Cell and Working Gas

The KEDR detector uses a cell that was first applied in the drift chamber of the SLD detector [35], with certain variations. The cell comprises eight anode wires, six of which are sensitive (Fig. 14). The edge dummy anode wires serve for equalizing fields in the cell. A radial distance between anode wires is 4.5 mm. The anode wires 28 μm in diameter are made of gilded tungsten and have a tension of 100 g. A gas gain is determined by the potential on the focusing wires located at a distance of ± 3.5 mm from the anode wires. The potential distribution on the field wires creates a uniform field of 1.6 kV/cm in the drift gap. The field wires are arranged with a pitch of around 4.5 mm. The Lorentz angle for a magnetic field of 1.8 T is 3° . The cell's radial size is 36 mm; maximum drift distance is around 30 mm. The pure dimethyl ether ($\text{C}_2\text{H}_6\text{O}$) under a pressure of 1.06 atm was chosen as a working gas. A drift velocity in dimethyl ether at a working field strength of 1.6 kV/cm is 4.6 $\mu\text{m}/\text{ns}$ while a diffusion factor is close to a minimum value. Basic parameters of the cell are given in Table 6.

6.3. Momentum Resolution

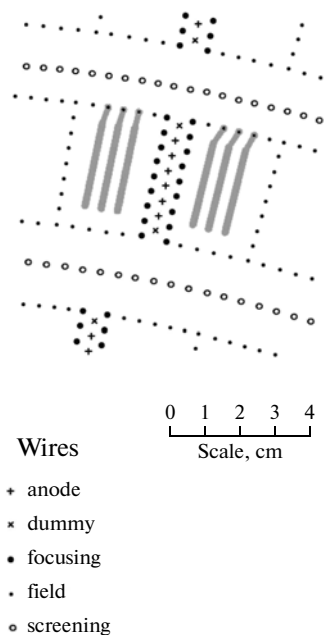
A momentum in the detector is measured using the DC and VD, where the measurement base increases from 370 to 450 mm, while a number of coordinate measurements grows from 42 to 48. The calculated momentum resolution in this case for the design magnetic field of 1.8 T is

$$(\sigma_{p_\perp}/p_\perp)^2 = (0.003)^2 + (0.0033p[\text{GeV}])^2. \quad (6)$$

In the calculation of multiple scattering, the material of wires and working gas was taken into account. While calculating a contribution of multiple scattering by wires, the trajectory with a kink at the point where a particle hit the wire was used, which decreases a value of this contribution to the momentum resolution by a factor of 1.6.

Now the spatial resolutions $\sigma_x = 115 \mu\text{m}$ in axial layers and $\sigma_x = 220 \mu\text{m}$ in stereo layers are obtained in the drift chamber. The momentum resolution at the 0.6 T working magnetic field is

$$(\sigma_{p_\perp}/p_\perp)^2 = (0.03)^2 + (0.02p[\text{GeV}])^2. \quad (7)$$

**Fig. 14.** The DC cells.

6.4. Particle Identification

For identification of charged particles in the drift chamber, a value of dE/dx on the track is used, which is calculated by summing losses over hits with the help of the modified truncated-mean method based on the dependence of resolution on the ionization density. A degree of particle discrimination in units of standard deviations is

$$S = \frac{|dE_1 - dE_2|}{\sigma}, \quad \text{where } \sigma = \frac{\sigma_1 + \sigma_2}{2}. \quad (8)$$

Here $dE_{1,2}$ are the most probable ionization losses of energy and $\sigma_{1,2}$ are the standard deviations of energy losses for two particles. The energy resolution of the drift chamber achieved in the experiment was 8.5% for the minimum ionizing particles at normal incidence, which ensures the π/K separation up to the momentum 670 MeV/c and the K/p discrimination up to 1200 MeV/c at the level of 2σ [2].

6.5. Electronics

The parallel data readout is used [36]. Electronics located directly on the chamber (see Fig. 13) consists of the linear preamplifier developed and fabricated at the BINP. Main preamplifier parameters are as follows: the input resistance is 75 Ω , the conversion slope is 3.5 mV/ μ A, the pass band is 20 MHz, the consumed power is 92 mW, and the output is paraphase (push-pull output). The possibility of gain calibration is envisaged in the layout.

The recording electronics consist of TAM boards performed in KLUKVA standard and designed for measuring the drift time and signal amplitude. The TAM board enables these measurements to be taken for four particles in a single DC cell. For the second-level trigger organization, the readout of data on operation of wires (YES-NO) to the second-level trigger interface is provided in the board.

This information is collected at input registers of the switchboard during the drift time of electrons in the DC cell.

6.6. High-Voltage Supply

A high voltage is supplied to the chamber from two sources performed in the CAMAC standard. One source with a nominal value of -2.77 kV supplies the voltage to the focusing wires that have the same potential in all superlayers. Another source supplies a voltage of -7.5 kV to the field wires.

Filters and high-voltage dividers are arranged directly on the chamber. For enhancing the reliability, each superlayer for high voltage is divided into three parts, the voltage to which is fed in the detector separately.

Table 6. Cell parameters

Parameter	Value
Number of sensitive anode wires	6
Wire diameter:	
anode (W/Au)	28 μ m
field and focusing (Ti/Au)	150 μ m
screening (Ti/Au)	70 μ m
Wire tension:	
anode and screening	100 g
field and focusing	250 g
Field strength on the wire surface:	
anode	360 kV/cm
focusing	8 kV/cm
field	15–52 kV/cm
Maximum voltage on the field wires	7.5 kV

6.7. Gas system and Temperature Measurement System

A drift velocity of electrons in dimethyl ether depends linearly on the gas density and the electric field strength. The variations in gas parameters $\Delta T = 0.3^\circ\text{C}$, $\Delta p/p = 10^{-3}$, and $\Delta E/E = 10^{-3}$ make a contribution to the error of coordinate measurement of 10 μ m for 1 cm of the drift. The DC gas system provides for the possibility of the gas density stabilization in the chamber, which is performed by means of compensation for a change in the temperature due to temperature oscillations by the appropriate change in the pressure.

An inner volume of the external pipe of the pipeline, gas panel, and the space between the end plates and outer DC lids is flushed with nitrogen to eliminate the possibility of gas accumulation and occurrence of the highly explosive concentration in case of arising a leak of dimethyl ether from the gas system. The use of nitrogen permits the oxygen leakage into the DC volume to be reduced and increases a length of absorption of electrons.

The temperature measurement system comprises 32 Sensikon sensors. The temperature sensors were calibrated with an accuracy of better than 0.1°C .

7. AEROGEL THRESHOLD CHERENKOV COUNTERS (ASHIPH SYSTEM)

The ASHIPH (Aerogel, SHifter, PHotomultiplier) system of the KEDR detector includes 160 counters: 80 barrel counters and 80 endcap counters (Fig. 15). The ASHIPH counters with light collection using the wavelength shifters, having been developed at the BINP since the 1980s, make it possible to substantially decrease the number of photomultipliers and to use the photomultiplier with a smaller area than in case of direct light collection [37–39]. The system

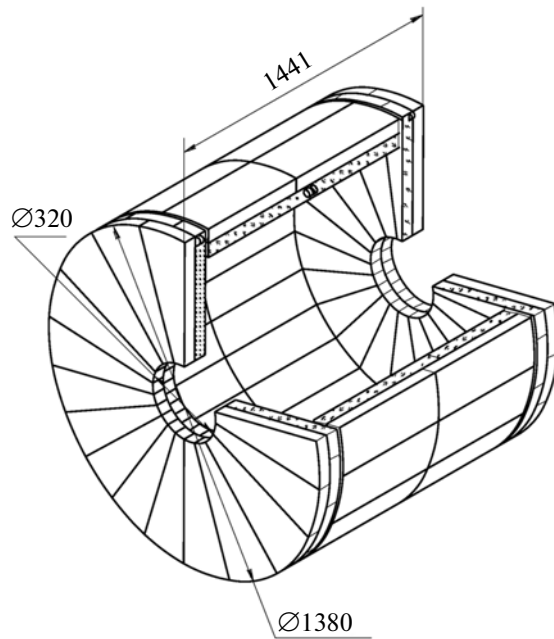


Fig. 15. Layout of ASHIPH system of the KEDR counter.

parameters are presented in Table 7. The system can operate in a magnetic field up to 1.8 T.

Constructions of the end and barrel counters are presented in Figs. 16 and 17, respectively. Walls of the counters are covered with the diffusive-reflective material based on polytetrafluorethylene (PTFE) having the 97–98% reflection coefficient from the layer 750 μm thick [40]. The Cherenkov light from aerogel is collected on the wavelength shifter, reradiated at a wavelength of ~ 500 nm, and its part ($\sim 50\%$) falls in the conditions of the total internal reflection. This part of reradiated light propagates as through a light guide to the photomultiplier connected via an optical contact to one of the wavelength shifter ends. A reflector made of PTFE is installed at the opposite end.

For computation of light-collection coefficient, a program has been developed for simulation using the Monte Carlo method. Input parameters include the measured spectral characteristics of aerogel, wavelength shifter, photomultiplier tube, and PTFE [38].

Table 7. Main parameters of the ASHIPH system

Solid angle of the system	$0.96 \times 4\pi$
Number of layers	2
Number of counters in a layer	80
Refractive index of aerogel	1.05
Momentum range of π/K discrimination	0.6–1.5 GeV/c
Amount of substance for a normal particle	$0.24X_0$
Aerogel volume	1000 L

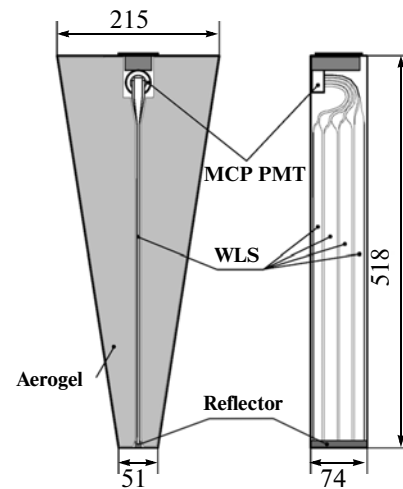


Fig. 16. Endcap counter.

An important feature of the entire system of counters is its two-layer structure. The counters are arranged in such a way lest a particle travelling from the point of beam interaction with a momentum higher than 0.6 GeV/c passed through shifters simultaneously in two layers of counters. A probability that a particle with a momentum of 0.6 GeV/c might fall into the shifter in a single layer is 10%, for a momentum of 1.5 GeV/c, 5%. This means that for identification of the most part of particles, it will be possible to use the data from two layers, which substantially improves the quality of identification.

7.1. Aerogel

From 1986, the Borekov Institute of Catalysis of Siberian Branch of the Russian Academy of Sciences and the BINP have been conducting joint works for the aerogel fabrication. The aerogel production is achieved with the refractive index $n = 1.008\text{--}1.13$ [41]. This aerogel by optical parameters is one of the world's best. Figure 18 presents the data on the absorption length for the aerogel used in the KEDR detector. The aerogel possesses the ability to absorb water from the environment. A large amount of the absorbed water leads to the mechanical damage of the aerogel; therefore all counters are pressurized during the fabrication.

7.2. Wavelength Shifters

The development of wavelength shifters was carried out jointly by the BINP and the Kargin Research Institute of Polymers (town of Dzerzhinsk). The wavelength shifter based on acrylic resin (PMMA) with addition of BBQ (benzo(de)benzo(4,5)imidazo(2,1-a)isoquinolin-7-one): 150 mg of BBQ per 1 kg of PMMA, produced as sheets 3 mm thick. Cutting, polishing, fashioning, and quality check of shifters are performed at the BINP. A wavelength shifter with

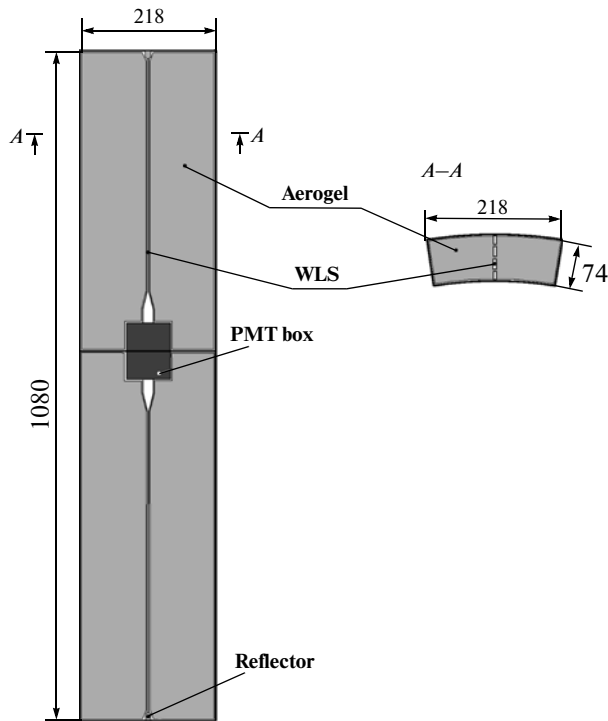


Fig. 17. Two barrel counters in a single housing.

BBQ has an absorption spectrum of 280 to 450 nm. With the 3-mm thickness, photons from this wavelength region are re-radiated at a probability close to 100%. The light is re-radiated by BBQ into the narrow peak with a maximum at a wavelength of 500 nm.

Figure 19 displays the probabilities of the photon conversion to photoelectron depending on the distance from the point of photon absorption to the photodetector (the attenuation length for the wavelength shifter sample with a section of $3 \times 17 \text{ mm}^2$ at different stages of production [38, 42] is indicated).

7.3. Photomultipliers

A photomultiplier multialkali photocathode based on microchannel plates and was chosen as a photon detector for the ASHIPH system. These devices are manufactured in Novosibirsk by the enterprises OAO “Katod” and ZAO “Ekran FEP”. The multialkali photocathode has the maximum quantum sensitivity at a maximum of the BBQ radiation spectrum. Other advantages of this device are its small overall dimensions (a height of 17 mm, a diameter of 31 mm), a gain of 10^6 , a weak sensitivity to magnetic field (the gain reduces by a factor of 3–5 in the 1.8-T field), and the comparatively low cost [38, 42–44].

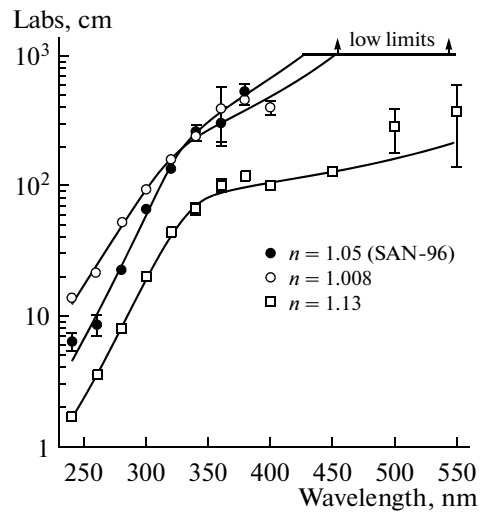


Fig. 18. The measured dependence of absorption length in aerogel as a function of the light wavelength for different aerogels.

7.4. Electronics

A charge from the photomultiplier anode is converted by the charge-sensitive preamplifier to the parphase (bipolar) signal that is brought out of the detector and is supplied to inputs of digitizing boards via a long cable (~40 m).

The dedicated electronic board A6 was developed in the KLUKVA standard, which works in the pipeline mode. Basic elements of the circuit are a 10-digit analog-to-digital converter (ADC) and a shift register. The ADC measures an instantaneous voltage value

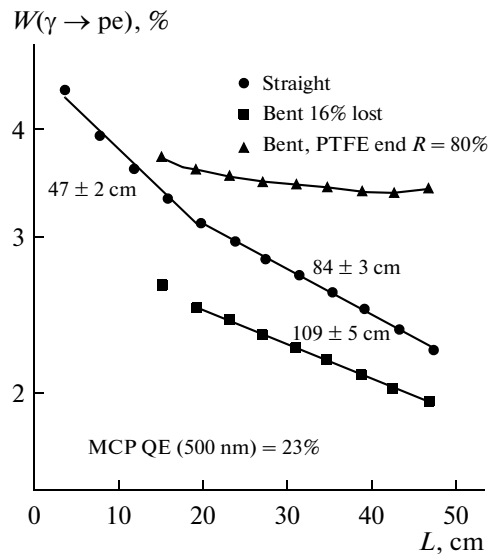


Fig. 19. The measured probability of the photon conversion to a photoelectron ($W(\gamma \rightarrow pe)$) of shifter as a function of the distance from the photodetector (the number near a curve denotes the attenuation length).

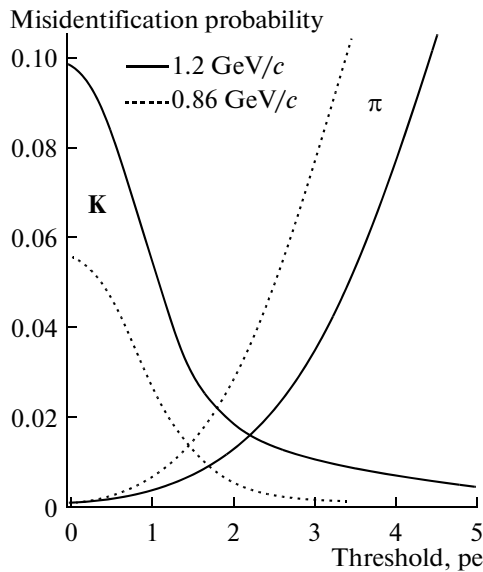


Fig. 20. The measured dependence of misidentification of pions and kaons on the amplitude for the momenta $P = 0.86 \text{ GeV}/c$ and $P = 1.2 \text{ GeV}/c$.

with a period of 50 ns. The shift register serves as data storage for the trigger-operation time. Five values of voltage are read out for each pulse; an amplitude and time of arrival of the pulse are reconstructed using them. There is a discriminator in the circuit to monitor the intrinsic noise of photomultipliers.

7.5. Testing a Counter in the Beam

In 2000, the quality of π/K separation of the ASHIPH end counter was measured in secondary beams of the proton synchrotron in the JINR (Dubna) [45]. The inhomogeneity of light collection was measured in the pion beam with a momentum of $0.86 \text{ GeV}/c$ over the entire area of the counter. The signal inhomogeneity was $\pm 15\%$.

Figure 20 displays the probabilities of misidentification of kaons and pions depending on the threshold for signal amplitude. For the momentum $0.86 \text{ GeV}/c$ with a threshold of 0.05 photoelectrons, the pion suppression factor is 900 with the 94% efficiency of kaon detection (separation is 4.7σ). With the momentum $1.2 \text{ GeV}/c$, the pion suppression factor is 1300 with the 90% efficiency of kaon detection (4.5σ).

A time resolution of the ASHIPH counter for pions with the momentum $0.86 \text{ GeV}/c$ was $\sigma_\tau = 2 \text{ ns}$ [39].

7.6. Long-Term Stability of Counters

The study of the long-term stability was conducted using 20 endcap counters that were assembled in 1999–2000. The counters were inside the detector from 2000 to 2003. Periodically, a high voltage was supplied to them, the photomultiplier noise was mea-

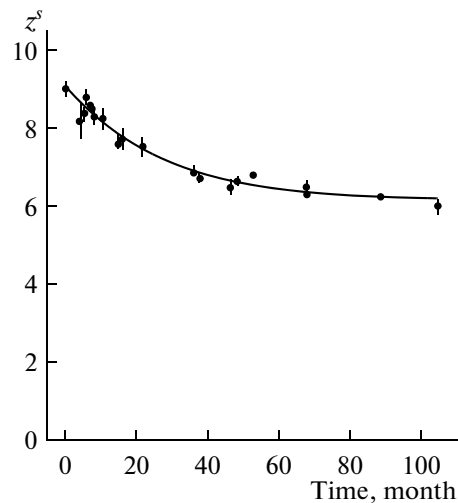


Fig. 21. The signal amplitude (number of photoelectrons) from cosmic muons as a function of time.

sured, and the amplitude spectra were recorded. All counters were tested with cosmic particles before the installation in the detector and after the removal from the detector. The time dependence of the number of photoelectrons for one of the counters is presented in Fig. 21. The signal drop as a function of time was stabilized at the level of 66% of the initial value; the number of photoelectrons has been unchanged (within $\sim 10\%$ uncertainty) for the last five years.

The disassembling of 13 counters was performed, and the deterioration of parameters was studied for aerogel, photomultiplier, wavelength shifter, and reflector individually. A mean decrease in the number of photoelectrons in the counters for three years was 38%. The deterioration of aerogel optical transparency on average leads to the decrease in the number of photoelectrons by 18%. A drop of the photomultiplier efficiency was 17%. It was established that optical properties of the aerogel are restored [41] with annealing ($\sim 5 \text{ h}$ at the temperature $500\text{--}600^\circ\text{C}$).

7.7. Status of the System

One layer of the ASHIPH system (80 counters) has been working in the KEDR detector since 2003. During the experiment, the information on the system workability is obtained on completion of each run (every 1–3 h). In 2005, a mean efficiency for Bhabha scattering events detected was 99% in the endcap counters and 88% in the barrel counters. The similar efficiency in 2010 was 97% for the endcap counters and 78% for barrel counters.

On experiment shutdown in 2011–2013, the second layer (80 counters) will be mounted and the repair of the first-layer counters will be performed.

8. TIME-OF-FLIGHT SYSTEM

Among the problems the time-of-flight system solves in the experiment are activation of the first-level trigger from charged particles, suppression of the cosmic particles background, particles identification by the time of flight, and measurement of energy losses in the material of a counter.

8.1. Construction

The time-of-flight system of the KEDR detector consists of the barrel and endcap parts. Its main parameters are presented in Table 8.

The Bicron-408 plastic scintillator is used as a material for the time-of-flight counters. The XP2262 photomultipliers are used in the system for detecting the scintillation light. The photomultipliers mounted on light guides are enclosed in magnetic shields.

8.2. Electronics

Each photomultiplier has two channels of the digitizing electronics: amplitude and time channels; additionally, signals from photomultipliers enter the first-level trigger and serve as arguments to form a start for readout of the detector data.

The electronics channel of the time-of-flight system includes the time and amplitude parts (Fig. 23). Amplitude of photomultiplier signal is measured and digitized in the amplitude channel; the time between the photomultiplier operation and the primary trigger signal, in the time channel. The electronics channel includes the splitter-discriminator (SD), the delay line of analog signal (DLA), the delay line of logical signal (DLL), the charge-time converter (QT), and the time expander (TAD). Logic signals from the QT and TAD outputs are supplied via the twisted pair to the digitizing electronics made in the KLUKVA standard. A total number of channels is 256: 128 time channels and 128 amplitude channels.

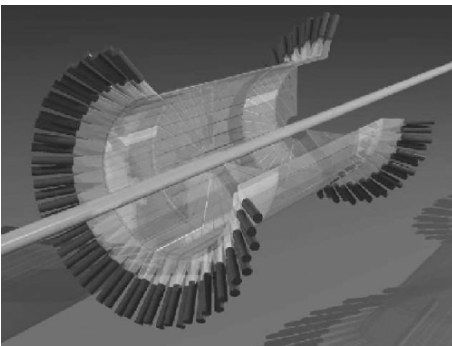


Fig. 22. The drawing of the time-of-flight system.

Table 8. Main parameters of the time-of-flight system

Barrel counters:	
solid angle	$0.71 \times 4\pi$
number of counters	32
length of sensitive part	1640 mm
scintillator thickness	10 mm
distance from the axis	715 mm
number of photomultipliers per counter	2
Endcap counters:	
solid angle	$0.26 \times 4\pi$
number of counters	$2 \times 32 = 64$
scintillator thickness	20 mm
distance from the intersection region along the axis	735 mm
number of photomultipliers per counter	1

8.3. Physical Parameters of the System

For the system calibration, experimental events of elastic e^+e^- scattering are used. The resolution in time of flight for them is 300 ps for the endcap counters and 360 ps for the axial counters. This resolution makes it possible to discriminate between kaons and pions at the 2σ level up to momenta of 600 MeV/c and to suppress cosmic ray particles effectively enough. Figure 24 presents the dependence of the inverse velocity of particles (the parameter $1/\beta$) upon the momentum for experimental multihadron events. Theoretical curves correspond to different mass hypotheses: π^\pm (lower curve), K^\pm (middle curve), p , \bar{p} (upper curve).

Figures 25 and 26 illustrate the use of particle identification by time of flight during the processing of the experimental data acquired for the ψ' meson. Figure 25 shows the experimental spectra of invariant masses of two different-charge particles with a common vertex on assumption that all particles are K^\pm . After employing the time-of-flight (ToF) selection, a peak from

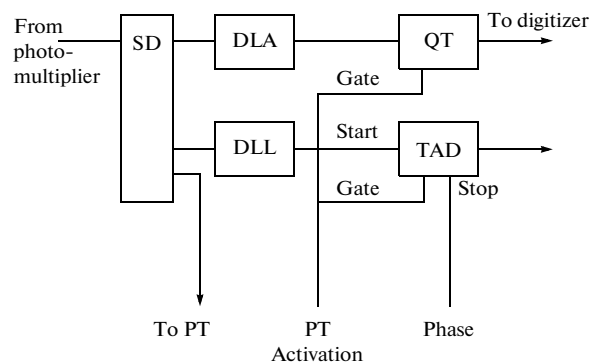


Fig. 23. Electronics channel of the time-of-flight system.

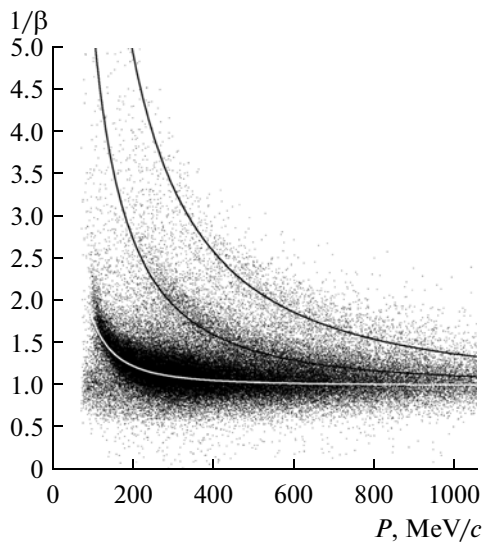


Fig. 24. Separation of particles by ToF (experiment).

$\phi \rightarrow K^+K^-$ is clearly seen; the background level is reduced by about 60 times. Similar spectra on assumption that all particles are either p and π^- or \bar{p} and π^+ are displayed in Fig. 26. After the separation by ToF, a peak of events of the process $\Lambda \rightarrow p\pi^-$ and $\bar{\Lambda} \rightarrow \bar{p}\pi^+$ is clearly seen.

9. ENDCAP CALORIMETER

The endcap calorimeter of the KEDR detector is constructed on the basis of scintillation crystals CsI(Na) with light detection by vacuum phototriodes (PT). The basic properties of crystals CsI(Na) are as

follows [8, 46]: the density $\rho = 4.51 \text{ g/cm}^3$, $dE/dx = 5.6 \text{ MeV/cm}$, $X_0 = 1.86 \text{ cm}$, Molière radius is 3.57 cm , hygroscopicity is weak, luminescence maximum is at $\lambda_{\text{max}} = 420 \text{ nm}$, refractive index for λ_{max} is 1.84, luminescence time is 630 ns , light yield is $40 \times 10^3 \text{ photons/MeV}$.

The endcap calorimeter (see Fig. 1) comprises two parts arranged around the vacuum chamber symmetrically with respect to the interaction region of e^+e^- beams. Each part includes four modules and an internal system consisting of separate counters (Fig. 27). Main parameters of the endcap calorimeter are given in Table 9.

The module is assembled of 74 units. A unit of the endcap-calorimeter module consists of two CsI(Na) crystals with sizes of $60 \times 60 \times 150 \text{ mm}$; its full length is 300 mm or $16.1X_0$. The unit layout is shown in Fig. 28. The system of internal counters located near the vacuum chamber of the storage ring contains 24 crystals with a length of 300 mm . In all, there are 1232 crystals in the calorimeter. The construction's units and their characteristics are described in more detail in [47]. The results obtained with the detector prototype are presented in [48]. The limiting capacities of this layout are investigated in [49].

9.1. Crystals and Counters

The endcap calorimeter of the KEDR detector uses CsI(Na) crystals produced by NPO "Monokristalreaktiv" (city of Khar'kov). The crystals are wrapped with the diffusion reflector made of the film of SKL porous teflon with a thickness of $70 \mu\text{m}$ and packed into a container made of aluminized mylar $20 \mu\text{m}$ thick. The kaprolon flanges are mounted at the crystal ends, which serve for fastening the mylar container and photodetectors. An optical contact between

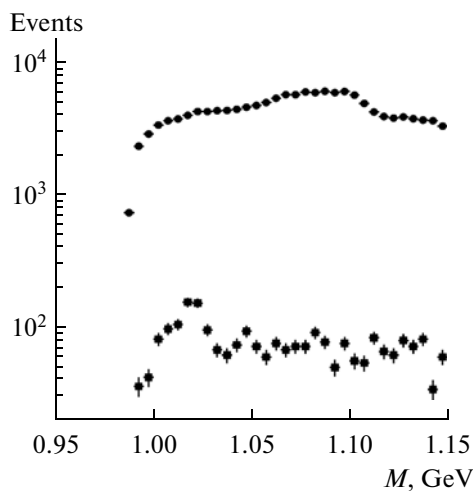


Fig. 25. Experiment. Separation of events, containing ϕ meson from the decay $\phi \rightarrow K^+K^-$. At the top: all particles. At the bottom: the same after the selection by the time of flight.

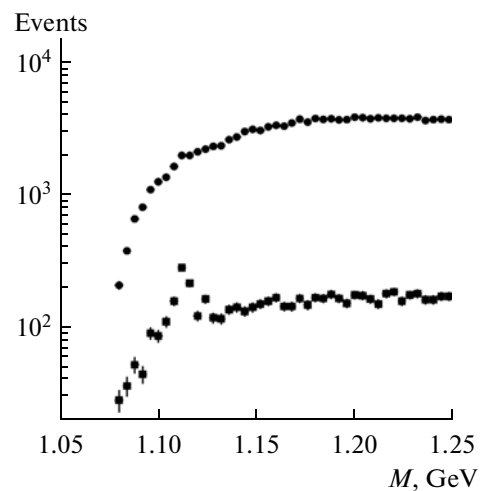


Fig. 26. Experiment. Identification of events with Λ from the decays $\Lambda \rightarrow p\pi^-$ and $\bar{\Lambda} \rightarrow \bar{p}\pi^+$. At the top: all particles. At the bottom: the same after the selection by the time of flight.

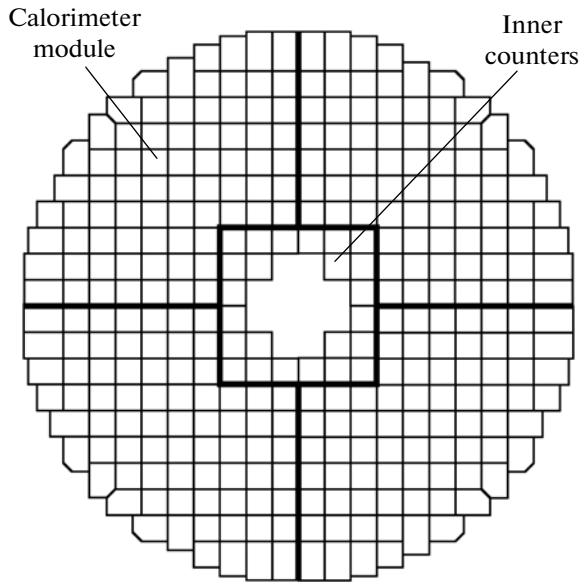


Fig. 27. Schematic layout of the endcap calorimeter of the KEDR detector.

the crystal surface and a window of the phototriode is provided by means of the optical silicon lubricating grease. The light yield of the counters with consideration for the light collection factor is around 10^4 photons per 1 MeV of the energy released in the crystal, the inhomogeneity of the light collection along the crystal length does not exceed 10%.

9.2. Phototriodes

Vacuum phototriodes capable of working in strong magnetic fields (to 2 T) are used as photodetectors in the endcap calorimeter of the KEDR detector. The phototriodes were manufactured at the “Ekran” factory in Novosibirsk [50]. They have a semi-transparent bialkali photocathode, a flat electrode—the plate that is a dynode, and an anode-grid between the photocathode and dynode. A diameter of the phototriode is 50–52 mm, and its height is 45–50 mm. A diameter of the photocathode sensitive area is 48 mm. The quantum efficiency is 10–15%, the inhomogeneity of quantum efficiency over the photocathode area is around 10%. The dynode gain is 10–15. When operating in a magnetic field of 0.6–1.0 T, the phototriode gain reduces approximately two-fold.

It should be noted that for the time elapsed after the manufacturing of the phototriodes (they were produced more than 20 years ago, moreover they were operated in the calorimeter for around 10 years), nearly 19% phototriodes went out of service or deteriorated substantially their parameters.

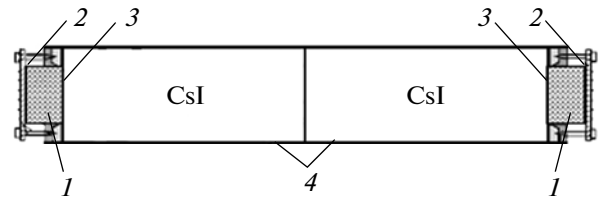


Fig. 28. A unit of the endcap calorimeter module of the KEDR detector (includes two CsI crystals with a size of $60 \times 60 \times 150$ mm). Numerals denote phototriode (1), preamplifier (2), kaprolon flange (3), and container of aluminumized LAVSAN (4).

9.3. Electronic Circuit

A circuit of the electronic section of the KEDR detector calorimeter is presented in Fig. 29.

A charge from the phototriode anode comes to the input of the charge-sensitive preamplifier. The transmission coefficient of the preamplifier is 0.22 V/pC. Then a signal is formed in the F15 amplifier-shaper board, after which it is digitized by the ADC with the peak detector A32 [51], performed in the KLUVA standard [52]. The time for signal shaping is 3 μ s.

In each board, the analog summing of all signals that come to its input is performed. This summed signal is also fed to the ADC. In addition to that, the summed signal is used for organization of the neutral trigger of the detector; for this purpose its additional shaping is performed. A front of this signal after shaping is 300 ns. On shaping completion, the signal is supplied to the comparator. If its amplitude exceeds the specified reference voltage, a logic signal is generated, which is used in the detector trigger. For checking the work of the described circuit, the logic signal from the comparator is also supplied to the ADC.

A dedicated (calibration) input is provided in every preamplifier of the calorimeter to conduct the calibration of electronic section of the endcap calorimeter and to verify its workability.

Table 9. Main characteristics of the endcap calorimeter

Solid angle	$0.21 \times 4\pi$
Polar angle	$6^\circ\text{--}38^\circ$ and $142^\circ\text{--}174^\circ$
Number of crystals	1232
Size of crystals	$60 \times 60 \times 150$ mm, $60 \times 60 \times 300$ mm
Unit length	300 mm ($16.1X_0$)
Outer radius of the calorimeter	665 mm
Mass	3.2 tons
Energy resolution (design)	3.5% at 150 MeV 2% at 1000 MeV
Spatial resolution	6–12 mm

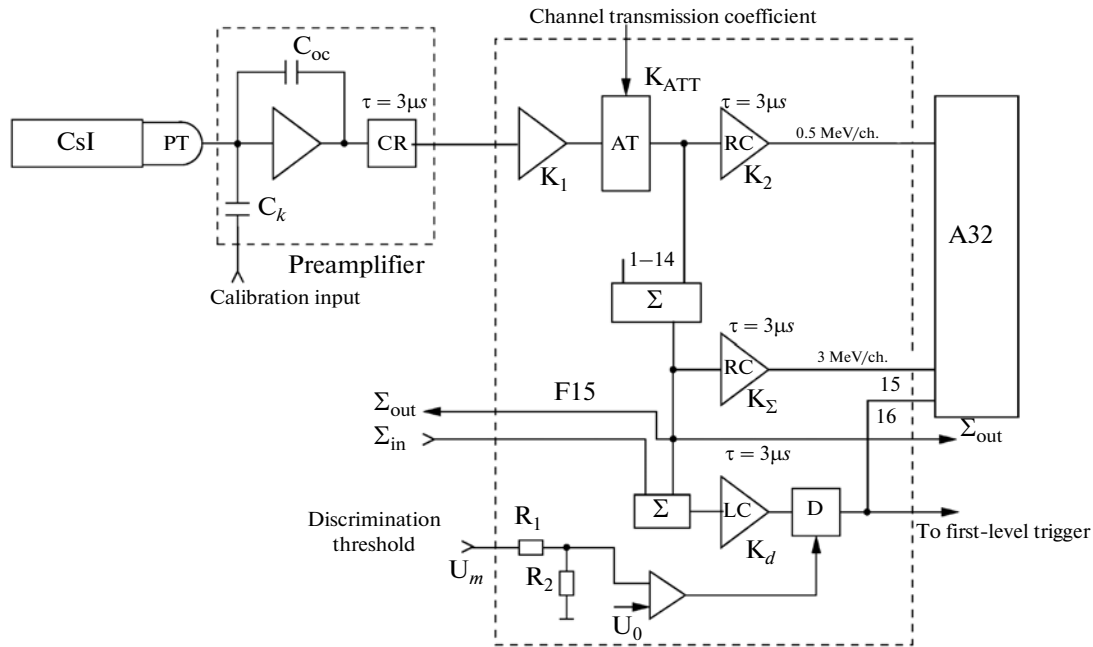


Fig. 29. Electronic circuit of the endcap calorimeter (consists of a phototriode (PT), preamplifier, amplifier-shaper F15, and ADC A32).

9.4. Calibration of the Calorimeter and the Achieved Parameters

The calorimeter calibrations include the following procedures: measuring ADC pedestals (every day); calibration of electronic section using the pulse generator (every day); calibration of the calorimeter using cosmic ray particles (1–2 times a week); absolute calibration of energy using events of elastic e^+e^- scattering (as the necessary statistics is acquired).

The following data are obtained. The stability of pedestals between the measurements is better than that of a single ADC channel, which is equivalent to 0.5 MeV of the energy released in crystals. The stability of the electronic section is 0.3–0.4%. The integral nonlinearity does not exceed 1% within the entire measurement range. Total noise of the electronic section is equivalent to 0.4 MeV of the energy released in the crystal; a fraction of coherent noise is no more than 20%.

When the cosmic calibration is conducted (between once and twice per week), an accuracy of measurement of the cosmic spectrum position is 3–4%. The obtained data permit us to assert that the time drift of the transmission coefficients of the measuring channels of the calorimeter is small. So, when cosmic calibrations performed with a time gap of two to four weeks are compared, a difference of the obtained calibration coefficients is determined by the accuracy of measurement of the cosmic spectrum position. From the data available, we draw a conclusion that on average the stability of channels of the endcap calorimeter

during the time interval between the cosmic calibrations is better by 2%.

The energy resolution of the calorimeter obtained by events of elastic e^+e^- scattering is 3.5% at the particle energy 1.5 GeV. The spatial resolution of the calorimeter at this energy is ≈ 8 mm and corresponds to the design value. The obtained energy resolution is worse than the design value (see Table 9), which is caused mainly by inaccuracy of calibration coefficients and, probably, by inhomogeneity of the light collection of crystals. The works are under way in modernization of calorimeter calibration procedures in order to achieve its design parameters.

10. BARREL CALORIMETER

As a barrel part of the electromagnetic calorimeter of the KEDR detector, the ionization calorimeter based on liquid krypton is used [53–55].

10.1. Construction

Figure 30 displays a construction of the liquid krypton (LKr) calorimeter of the KEDR detector. Its main parameters are summarized in Table 10.

The LKr calorimeter presents a set of cylindrical ionization chambers. The chamber electrodes are fabricated of sheets of fiberglass laminate (G10) with a thickness of 0.5 mm, covered on both sides by the copper foil 18 μm thick. There are a total of 35 layers of the electrodes in the calorimeter. A gap of 19.5 mm between the electrodes is set with the help of the con-

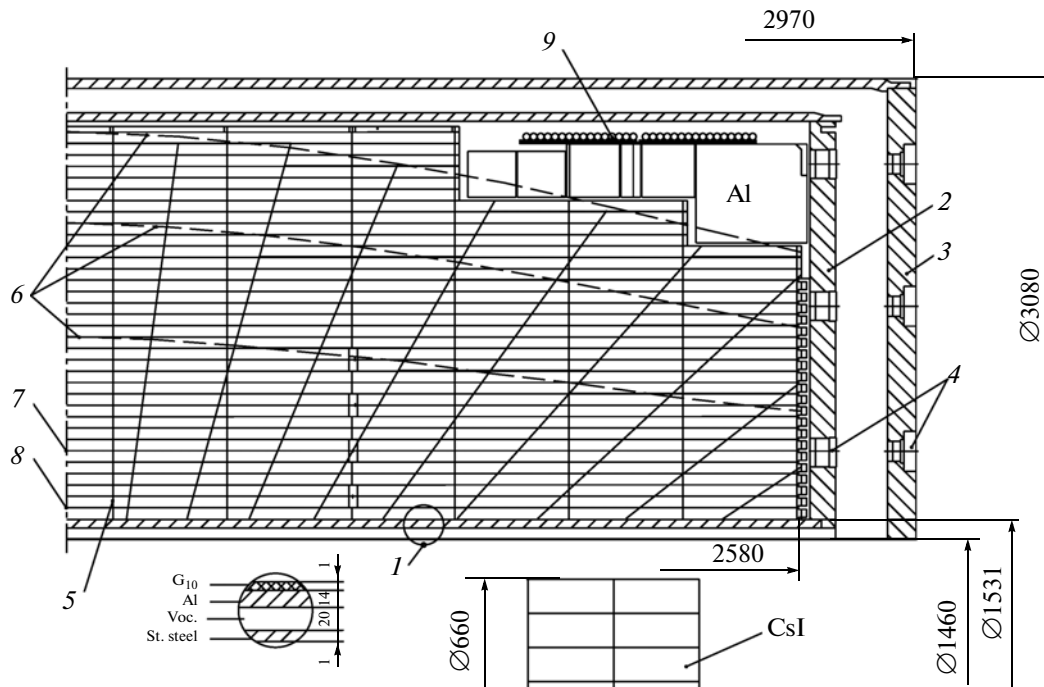


Fig. 30. Schematic layout of the LKr calorimeter: entrance wall (1), cold flange (2), warm flange (3), connectors (4), spacers (5), equal-thick lines (6), coordinate electrodes (7), high-voltage electrodes (8), and boards for wiring of high voltage and blocking capacitors (9).

struction consisting of the ring frames and the ribs crossing them along the calorimeter axis. Apart from maintaining the gap between the chamber electrodes, the frames are intended for fixing the electrodes from layer to layer. A system of electrodes is assembled in the cryostat with shield-vacuum thermo-insulator, the inner cryostat volume is manufactured of aluminum, while the outer volume is made of stainless steel. Inside the cryostat, the aluminum rings-squeezers are mounted on the outer radius of flanges for saving krypton. The glass connectors are welded into the cold and warm flanges for signal readout from the calorimeter. For thermal stabilization, the pipes are welded at the external side of the aluminum volume, through which, if necessary, gaseous nitrogen can be flushed.

Figure 31 schematically displays the system of the calorimeter electrodes. Readout of a signal for the energy measurement is performed from the high-voltage electrodes that are divided into rectangular pads connected to one another by radius in such a way that they form the cells (“towers”) of the calorimeter oriented to the interaction point.

At the radius nearest to a beam, the cells have a transverse size of $10 \times 10 \text{ cm}^2$, which increases as the distance from the beam grows. The calorimeter has three layers of these cells along the radius. The grounded electrodes of the first layer are divided into strips for measuring coordinates. Altogether there are four planes for measuring the z -coordinate and four planes for measuring the angle ϕ , which alternate with

one another. Widths of cells and strips increase along the z axis as the distance from the calorimeter center grows in order to ensure the equal resolution in polar angle.

10.2. Electronics

Electronics of the LKr calorimeter includes the following components: (i) boards with blocking capacitors installed inside the cryostat of the calorimeter and intended for readout of a signal from high-voltage electrodes; (ii) the chamber electronics mounted outside, on the calorimeter endcap flanges; (iii) the system of overcommutation of the calorimeter channels;

Table 10. Main parameters of the LKr calorimeter

Solid angle	$0.79 \times 4\pi$
Polar angle	$38^\circ - 142^\circ$
Inner radius	75 cm
Thickness	68 cm ($14.8X_0$)
Mass of LKr	27 tons
Energy resolution at 1.8 GeV (design)	2.4%
Energy resolution at 1.8 GeV (achieved)	3.0%
Resolution in mass of π^0	8 MeV
Spatial resolution	1 mm

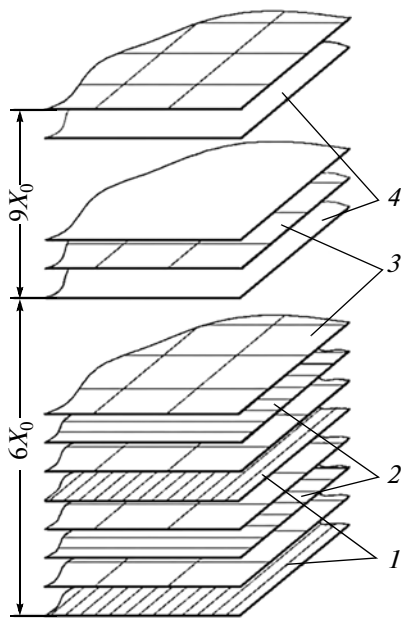


Fig. 31. Schematic of electrode structure of the calorimeter: ϕ strips (1), z strips (2), high-voltage electrodes (3), and grounded electrodes (4).

(iv) the calibration system of calorimeter electronics; (v) boards of summing for the first-level trigger of the detector; (vi) the intermediate electronics with RC-2CR shapers (one integrating and two differentiating cells); and (vii) the digitizing electronics.

A total number of channels in the readout electronics of the calorimeter is 7240, of which 2304 channels are designed for measuring the energy and 4936 channels are intended for measuring the coordinates. Measurements of the energy involve a signal read out from high-voltage electrodes, and then the blocking capacitor is required between the chamber and the measurement electronics. For this purpose, there are 48 boards of capacitors with 48 channels per board installed in the calorimeter. The nominal blocking capacitance per channel is 28 nF. The same boards serve for high-voltage wiring over the calorimeter.

The chamber electronics consists of the charge-sensitive preamplifiers based on the field-effect transistor SNJ1800D [56, 57], which are arranged on the cryostat endcaps in metallic boxes, 48 items in each box. Apart from preamplifiers, the boxes contain power-supply filters and calibration capacitors. Paraphase signals from the preamplifiers are brought out through the 96-pin connectors of PANDUIT type (two per each box). Through the same connectors, the power for preamplifiers (± 12 V) and signals from calibration generators are supplied.

A charge-sensitive preamplifier receives a pulse of current from the calorimeter chambers and integrates it on the feedback capacitor (nominal capacitance is 5 pF). The feedback resistance, sustaining the dc

mode, is 100 M Ω . Thus, the integration time constant is 500 μ s.

Signals from preamplifiers are transmitted via screened twisted pairs to the overcommutation system units that are located in the detector hall. There are dedicated calibration generators located in the same units, which create a current (close in shape to the current from a particle) through the calibration capacitors of channels. One calibration generator works for four boxes of preamplifiers. In addition to that, for spectrometric channels, the summation boards are installed in the overcommutation system units, which sum up signals from the eight neighboring channels in the first two layers and transfer the result to the first-level trigger of the detector.

The F32 boards with the RC-2CR shapers are located in the room of the data acquisition system of the detector in KLUKVA crates [36]. The two types of the shaper boards are available in the data acquisition system: F32B (with a time constant of 1.5 μ s), destined for work with spectrometric channels of the calorimeter, and F32P (with a time constant of 4.2 μ s), intended for work with coordinate channels. For increasing the dynamic range, the F32B boards have additional stages with tenfold amplification. Therefore, there are 32 shaped signals at output of these boards plus another 32 shaped signals with additional amplification. A total number of F32B boards is 72, while the number of F32P boards is 155.

The shaped signals from calorimeter are digitized by the 12-bit peak ADCs fabricated in the KLUKVA standard by 32 channels per board [51]. A range of digitization is from 0 to 2 V, digitization time is 100 μ s. Maximum integral nonlinearity is ± 3 channels.

10.3. Noise of Electronics and Radioactivity

The industrially produced krypton contains the admixture of the β -radioactive isotope ^{85}Kr with a half-life of 10.5 years and the boundary spectrum energy of 0.67 MeV. Electrons of β decay create a pointlike ionization in the gap of the ionization chamber of the calorimeter. The current signals from events of β decay are superimposed randomly on the useful signal in the calorimeter and present a source of additional noise.

Figures 32 and 33 display the distributions over noise measured in all calorimeter channels for the cases when a high-voltage supply to the calorimeter chambers is on and when it is off. The contribution to the channel noise is made by both the intrinsic noise of the calorimeter electronics and the noise from the krypton radioactivity in the first case and by the electronics noise alone in the second case. As it can be seen from these distributions, almost all spectrometric channels have the noise less than 1 MeV, while the noise of coordinate channels is less than 0.6 MeV. Subtracting quadratically the noise values measured

without high voltage from the noise values obtained under the high voltage supplied, we derive a contribution to noise from the krypton radioactivity. We have on the average 0.6 MeV for towers and 0.3 MeV for strips.

10.4. Calibration

The absence of internal amplification in the calorimeter enables the relative channel calibration to be conducted with acceptable accuracy using dedicated generators that simulate a current signal from particles at input of amplifiers. The calibration results in determination of the ADC pedestal and gains of channels. The generator calibration is performed twice a week. The measured time stability of pedestals is ± 0.3 of the ADC channel (0.3 MeV in energy units), while the relative gain stability is 10^{-3} .

Apart from the generator calibration, the calibration by the recorded events with cosmic mesons is also conducted. A main goal of cosmic calibration is to trace a variation in the calorimeter signal amplitude with time, which occurs as a result of slow krypton contamination by electrically negative impurities. A rate of reduction in the amplitude of the calorimeter signal with time is approximately 1% a month. The cosmic calibration also makes it possible to verify the workability for all calorimeter channels and to roughly perform the absolute calibration.

10.5. Calorimeter Parameters

The energy resolution of the calorimeter in the high-energy scale was measured on events of elastic e^+e^- scattering.

Figure 34 shows the distribution over the energy measured in the calorimeter for these events. The resolution at the energy of 1.8 GeV is $3.0 \pm 0.1\%$. The resolution for this energy expected from the calorimeter simulation is 2.4%. The difference is probably connected with the insufficient accuracy of the relative calibration of calorimeter channels. The energy resolution of the calorimeter in the low energy scale determines the detector resolution in reconstructed invariant mass of π^0 meson.

The energy resolution was studied using distributions over invariant mass of photon pairs (recorded in the calorimeter) from the ψ' -meson decay. Coordinates of photons were determined by the center-of-gravity method. It was found that if the coordinates are determined only from amplitudes of spectrometric channels, the resolution over the invariant mass of two photons from π^0 -meson decays is 9.6 ± 0.2 MeV. The presence of strips in the electrode structure allows the resolution to be improved to 8.4 ± 0.2 MeV [2].

It is obvious that the coordinate resolution becomes particularly important for reconstruction of high-energy particles. When the π^0 -meson energy is

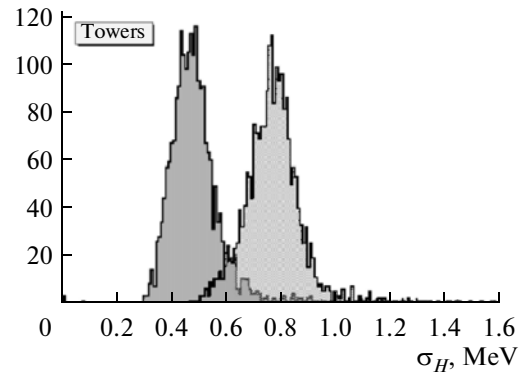


Fig. 32. Distributions for the measured noise in all spectrometric (tower) channels of the calorimeter. Left histogram corresponds to absence of high voltage on the calorimeter chambers; right histogram displays the case when the high voltage is supplied.

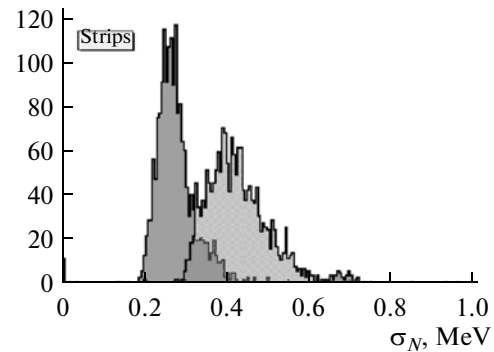


Fig. 33. Distributions for the measured noise in all coordinate (strip) channels of the calorimeter. Left histogram corresponds to absence of high voltage on the calorimeter chambers; right histogram displays the case when the high voltage is supplied.

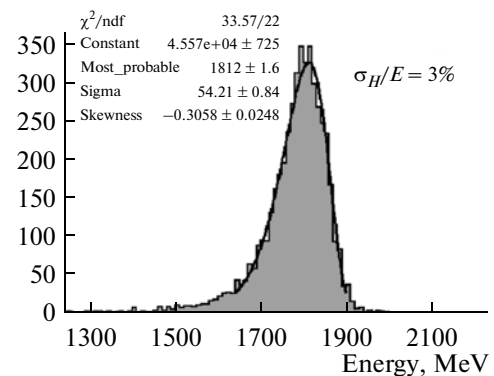


Fig. 34. Distribution over the measured energy release in the calorimeter for events of the e^+e^- scattering at the energy $2E = 3.6$ GeV, $\sigma_E/E = 3.0 \pm 0.1\%$.

Table 11. Main parameters of the muon system

Solid angle	$0.67 \times 4\pi$
Number of layers	3
Number of streamer tubes	2208
Tube length	4.5 m
Tube diameter	4 cm
Yoke thickness before a layer	23 cm (1.4 of nucl. lengths)
Mean resolution in coordinate along the tube	around 4 cm

more than 400 MeV, the following data are obtained for the resolution in the π^0 -meson mass: without using the data from the calorimeter strips, $\sigma_m = 10.2 \pm 0.2$ MeV, while with the reconstruction with the use of this information, $\sigma_m = 7.6 \pm 0.2$ MeV. Thus, a good spatial resolution of the calorimeter for photons appreciably improves the detector characteristics.

The calorimeter's spatial resolution itself was directly measured for minimally ionizing particles using events with cosmic muons [58]. In case of the muons incident perpendicular to a strip, the resolution was 0.62 ± 0.1 mm (for a layer with a strip width of 6.9 mm), which agrees well with the resolution obtained in simulation. The spatial resolution for different-energy photons was measured earlier using the calorimeter prototype [59]. The resolution obtained in this experiment is better than 1 mm almost in the entire energy region.

11. MUON SYSTEM

The muon (track length) system is designed for identification and separation of muons and pions by the difference in range in the detector material [60–62].

The muon system blocks are arranged in three layers inside the detector magnet yoke (see Fig 1).

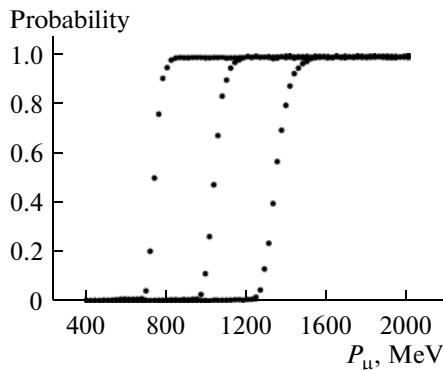


Fig. 35. The probabilities of activation of the 1st (left points), 2nd, and 3rd layers of the muon system for μ^\pm as a function of the momentum (simulation).

The system is constructed on the basis of cylindrical gas wire chambers working in the self-quenching streamer mode [63] of the so-called streamer tubes.

Main parameters of the muon system are given in Table 11.

Figure 35 and 36 present the results obtained with using KEDRSIM (see section 16) for computation of probability of operation of the muon system layers from μ^\pm and π^\pm mesons leaving the intersection region at an angle of $90^\circ \pm 5^\circ$ with respect to the beam axis at the uniform distribution over the angle ϕ .

11.1. Construction

The system consists of 2208 streamer tubes. Each tube is made of stainless steel 300 μm thick and has a length of 4.5 m and a diameter of 4 cm. The wire (anode) of gilded molybdenum 100 μm thick is stretched along the tube axis. The tube ends are closed with the insulating kapronit plugs, which fasten the anode vacuum-tightly and have holes for purging the working gas mixture.

The tubes are joined in blocks (Fig. 37). In each block, the tubes are fixed with the help of four duralumin matrices, two of which are located near the tube ends, while another two are arranged at a distance of 1/3 of tube length from the ends. Boards of chamber electronics and high-voltage wiring covered with protective housings are mounted on the end matrices. A block has the connectors for power supply, high voltage supply, calibration signals, for control of threshold of discriminators, an output signal connector, and pipes for working gas mixture input and output.

To reduce the damage from failure of an individual channel, tubes in the block are arranged in two layers with offset by a tube radius. To minimize the number of electronic channels, the anode wires are chained together, four in a chain (six in certain chains). Tubes are joined, as a rule, in an alternating manner, to

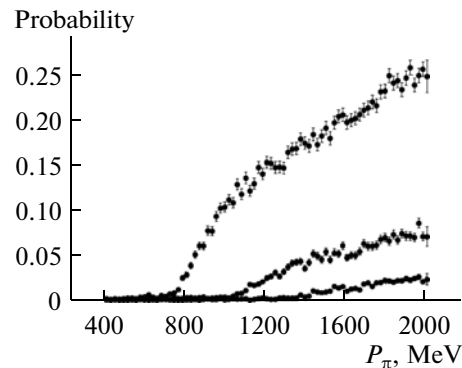


Fig. 36. The probabilities of activation of the 1st (left points), 2nd, and 3rd layers of the muon system for π^\pm as a function of the momentum (simulation).

reduce the probability of operation of several tubes of the same channel from one particle.

The system blocks are installed in the gaps of the detector magnet yoke in three layers. According to the octahedral shape of the yoke, blocks are grouped in octants.

11.2. Technology of Manufacturing

Mechanical assembling of a block is performed according to the following procedure: matrices, inside which the tubes are placed, are secured at the particular table; the tubes are carefully washed on the inside with water, and then with spirit; next, the anode wire is passed inside the tube and run through the holes in the plugs, in which the pins are inserted; the plugs are pressed in the tube ends by a special piston. The plugs preliminarily are rejected according to the surface charge current at high voltage. A circular collar 0.3 mm high is pressed out on the outer surface of the plug, while directly before the pressing, the silicone (organic-silicon) adhesive KS-5 is applied to the plug edges. This technology ensures the reliable pressurization of the joint, which is not broken with the temperature change in wide limits, and also the fastening of tubes with creation of reliable electric contact. The anode wire is stretched at an effort of 300 g and secured in the plugs with the help of pins. The pins are fabricated from the tinned capillary pipe made of annealed copper with an outer diameter of 1.6 mm and inner diameter of 220 μm . After stretching of all wires in the block, the insulated conductors are soldered to the pins. A site of pin mounting into the plug is also sealed with the KS-5 adhesive. Gas openings in plugs are connected by a PVC pipe.

After the mechanical assembling, the block tightness and wire tension are checked. For tightness check, the block is inflated with air up to the excess pressure 0.2 atm; in this case the leakage must be no more than 0.02 L/h. Since the characteristic flowrate of gas mixture through the block is 0.1 L/min and the pressure drop is almost absent, the real leakage is found to be substantially less than the value measured in testing. The wire tension is measured using the resonant method. The wires, whose measured tension is less than 100 g, are replaced.

At the next stage, the mounting of boards of wiring of high voltage and calibration signal, the assemblage of the chamber electronics, the soldering-up of cables, and the tuning of the chamber electronics are performed. Then the block is flushed with air and subjected to training by the reverse high voltage. After this, the block is flushed with the working gas mixture, and the rate curves and noise distributions over anode wires are measured.



Fig. 37. A block of the muon system at the test-bench. Protective housing is removed.

11.3. Gas mixture

Different gas mixtures for the self-quenching streamer mode were studied at the BINP [60, 61]. The gas mixture argon + carbonic acid gas + n-pentane is used in the muon system of the KEDR detector. At different periods of operation the ratio of components somewhat varied: (63:30:7), (68:25:7), and (60:32:8). With these concentrations of pentane this mixture is explosion-proof.

To obtain the working gas mixture, carbonic acid gas is flushed through n-pentane that occupies the temperature- and pressure-stabilized vessel. The pentane concentration in the mixture is determined by the pressure of saturated pentane vapors at the given temperature, therefore the temperature is stabilized with an accuracy of $\pm 0.1^\circ\text{C}$. Then the required argon amount is added to the mixture. Flows of argon and carbonic acid gas are regulated by the Bronkhorst controllers.

The prepared gas mixture is supplied in parallel to the system octants. Inside the octant, the purging is performed sequentially by blocks, from the inner layer to the outer one. Tubes of each block are flushed sequentially.

Since the system blocks were manufactured more than 20 years ago, their tightness often leaves much to be desired. Under these conditions, the requirements for continuity of purging of the working gas through the muon system sharply grow. In practice, the maximum time of the purging stop without the substantial deterioration of system parameters is around a day (by the end of the 2009–2010 season), after which the gaslocks of the spoiled gas form in the system, for removal of which it will take up to several weeks.

The gas-mixture quality is the necessary condition for high efficiency of recording. Unfortunately, faults of purging took place repeatedly during the experimental seasons.

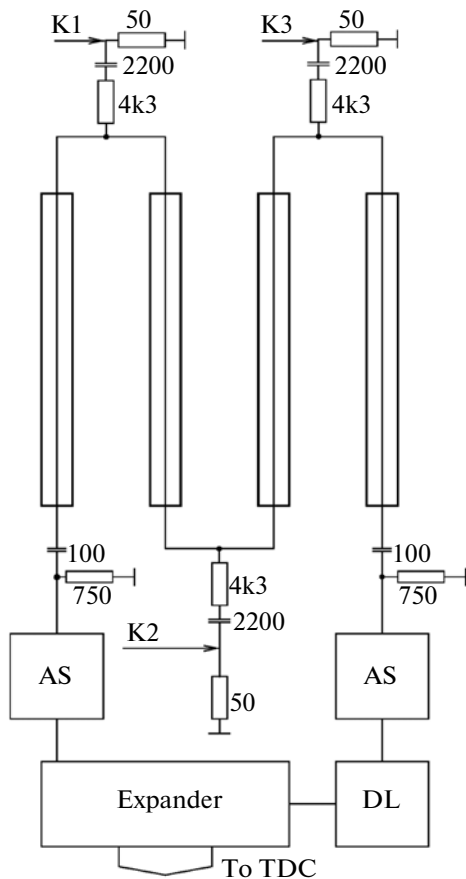


Fig. 38. A block-diagram of the electronic channel of muon chambers.

11.4. Electronics

The chamber electronics provides for determination of the longitudinal coordinate of the particle passage by a difference in time of signal arrival at the ends of a chain of tubes. A block-diagram of the electronic channel is shown in Fig. 38. Signals from the wire ends via the high-voltage decoupling enter the amplifiers-shapers. When an input signal exceeds the preset threshold, the former generates a logic signal of the specified duration. The input thresholds of AS discriminators can be regulated individually by means of trimming resistors within a range of 5–50 mV; additionally, thresholds of all ASs of the same block can be shifted simultaneously by the external control voltage. The AS threshold “start” is set approximately to 25 mV; “stop”, to 20 mV (thus, if “start” has operated, then “stop” has operated too).

The AS “start” is sent to the expander input directly, whereas the “stop” signal goes to the expander through the delay line (DL). The delay line is made of the twisted pair, its length is selected in such a way that the “stop” signal would always arrive later than the signal “start” would. Duration of the “start” signal is chosen such that before its termination, the

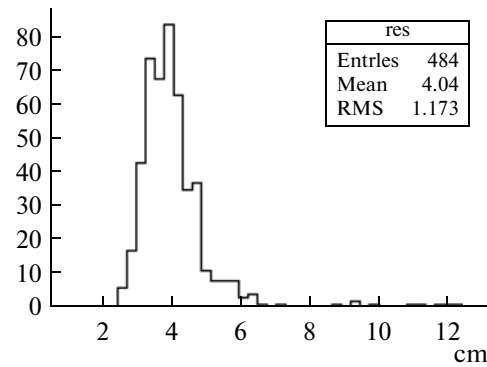


Fig. 39. The longitudinal coordinate resolution of the muon system channels (experiment in May, 2010).

“stop” signal would always have time to come to the expander. Amplitude of the “stop” signal is increased to compensate for attenuation in the delay line.

The expander generates at output the paraphase logic signal whose duration is several times greater than the time between the leading edges of “start” and “stop”. Parameters of the delay line and expander are selected such that a range of output signal duration would be approximately 2–8 μ s. An output signal is transmitted via a cable of screened twisted pair to the time-to-digital converter (TDC), which is the TP-board of the KLUKVA standard [64]. Measurements of signal duration are performed using the method of direct counting with a discreteness of 2.5 ns.

A number of the operated tube in a chain and a longitudinal coordinate of the hit are determined from the TDC time. A mean resolution of the system in longitudinal coordinate is 4 cm (Fig. 39). A transverse coordinate is determined by the position of the operated tube. The more accurate measurement of the transverse coordinate is unnecessary due to multiple scattering of particles in the detector material.

A high voltage required for the chamber operation in the self-quenching streamer mode is supplied independently to each system octant and further is distributed among blocks in parallel. A value of the working voltage is 4200 V, a width of plateau is around 400 V.

Faults of the chamber electronics and breakdowns in high-voltage cables are main causes of reduction in the muon-system efficiency. By the end of the 2009–2010 season, around 5% of system channels were faulty, around 5% more channels were partly operational (do not measure the hit coordinates).

11.5. The Calibration and Parameters of the System Obtained in the Experiment

The system calibration consists in determination of TDC time instants corresponding to the tube ends. It can be conducted with the help of the generator and by time spectra collected with cosmic particles.

The generator calibration is used mainly for check of electronics workability. The calibration constants are obtained from fitting the time spectra recorded in dedicated runs. Then they are refined by experimental runs. The longitudinal coordinate resolution is measured from direct tracks reconstructed in the muon system. A mean channel resolution of the muon system in the detector is around 4 cm (see Fig. 39).

The system efficiency is measured in experimental runs. The events are selected, in which tracks are reconstructed in the muon system. The system layers are used for cross tagging; so, e.g., for measuring the intermediate-layer efficiency, the tracks are used which have hits in the inner and outer layers. The measured efficiency is stored in the database and used during the analysis of experimental data. For example, in May 2010, a mean efficiency of the first layer was 97.6%, of the second layer was 98.3%, and of the third layer was 90.5% [2].

12. LUMINOSITY MONITOR

12.1. Introduction

The collider luminosity determines the frequency of observation of physical processes as

$$\frac{dN}{dt} = \mathcal{L}\sigma_{vis},$$

where \mathcal{L} is the luminosity, while σ_{vis} is the visible (effective) cross section in which the kinematics of the process, geometry, and efficiency of the detecting system are taken into account.

The VEPP-4M on-line luminosity is measured by the well-known process of the single bremsstrahlung (SBS) $e^+e^- \rightarrow e^+e^-\gamma$. The process cross section was first calculated in the 1960s in [65, 66]. The SBS photon spectrum has the form

$$\frac{d\sigma}{dx} = 4\alpha r_0^2 \frac{1}{x} \left[\frac{4}{3}(1-x) + x^2 \right] \left(L - \frac{1}{2} \right), \quad (9)$$

where $\alpha = 1/137$, $x = \omega/E_b$, ω is the photon energy, E_b is the beam energy, $L = \ln(4E_b^2(1-x)/m_e^2 c^4 x)$.

In this process one of the beam particles loses a part of energy by emitting a photon, while the particle travelling in the opposite direction almost does not change its motion. The emitted photons fly within a narrow cone along the direction of motion of the initial particle with the angle $\theta \sim m_e/E_b = 1/\gamma$. Determination of the counting rate from the electron and positron beams yields two independent measurements of luminosity. The energy spectrum of emitted photons at $\omega < E_b$ has the form $dN_\gamma/d\omega \sim 1/\omega$. The SBS spectrum edge corresponding to $\omega = E_b$ is used for amplitude calibration and measurement of resolution of the luminosity monitor.

In the 1980s, the more accurate measurements and calculations performed at the BINP [67, 68] demonstrated the appreciable influence on the emission mechanism from such parameters as beam size and impact parameter for the interaction of beams. As a result, the differential cross section of soft photon radiation reduces as compared with (9) (under our conditions, the correction is more than 5% for $\omega < 100$ MeV). With a beam size taken into account a total cross section for photons (with $\omega > \omega_{min}$) detected by the luminosity monitor decreases by 1–2% in the region of ψ -meson energy [69].

A cross section of SBS registration is approximated by the following formula:

$$\sigma_{vis} = C \left(\ln \frac{1}{T} - \frac{3}{8} T^2 + T - \frac{5}{8} \right), \quad (10)$$

where $T = \omega_{min}/E_b$. The expression in parentheses is an integral from formula (9) in the approximation $L = \text{const}$. The coefficient C , calculated by means of numerical integration of cross section (9) with consideration for the correction [68], changes smoothly from $C = 0.52 \times 10^{-25} \text{ cm}^2$ to $C = 0.63 \times 10^{-25} \text{ cm}^2$ with the energy variation from $E_b = 1.5 \text{ GeV}$ to $E_b = 5.5 \text{ GeV}$ and is well approximated with a polynomial. With the fixed beam energy, C weakly depends on the threshold: within the interval $\omega_{min} = 300 \pm 50 \text{ MeV}$, the change is no more than 1%. For the beam energy region 1.5–5.5 GeV and for the threshold $\omega_{min} = 300 \text{ MeV}$, the cross section of SBS registration varies within the limits of $(0.6–1.5) \times 10^{-25} \text{ cm}^2$. Thus, for the luminosity $10^{30} \text{ cm}^{-2} \text{ s}^{-1}$, the counting rate is around 100 kHz, which is enough for on-line measurements of luminosity.

12.2. Apparatus of Luminosity Monitor

The luminosity monitor of the KEDR detector presents two electromagnetic calorimeters located at the axis of colliding beams on each side of the intersection region at a distance of around 18 m (Fig. 45). Upon selecting the calorimeter design, the following factors were taken into consideration.

- For the SBS scattered electron and the bremsstrahlung photon, the relation $E'_e + \omega = E_b$ is fulfilled with a high precision. The accurate measurements of the bremsstrahlung photon energy ω will make it possible to tag the SBS particles fallen in the system of scattered electron tagging (see section 13), which gives the opportunity to reduce the background while studying two-photon processes.

- With work in the high-energy region (5 GeV), the VEPP-4M luminosity will amount to (several unities) $\times 10^{31} \text{ cm}^{-2} \text{ s}^{-1}$. In this case the load from photons with energy more than 100 MeV reaches 5 MHz, while the radiation load may be 1000 Gy for a year of work.

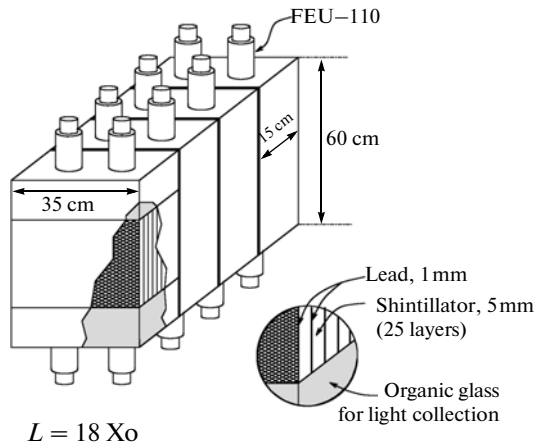


Fig. 40. The layout of scintillation sandwiches of the luminosity monitor at the VEPP-4M e^+e^- collider.

The available crystal scintillators (NaI, CsI) cannot operate under these conditions. A sandwich, consisting of interleaved plates of scintillation plastic (de-excitation time is ≈ 3 ns) and lead, was chosen as a calorimeter. The calorimeter construction was optimized to obtain a good energy resolution. The sandwich arrangement is shown in Fig. 40.

Each calorimeter consists of four identical units. A unit contains 25 layers of lead (1 mm thick) and plastic scintillator (5 mm thick). The light guides in the form of rectangular blocks of organic glass are glued to the scintillator plates at both sides. Each sandwich unit is viewed by four photomultiplier tubes (FEU-110) to ensure good light collection. Light emitting diodes that serve for check of photomultiplier workability are

glued into the light guides. A total radiation length of the sandwich is $18X_0$.

Signals from four units are summed and the resulting signal proportional to the photon energy is supplied to the discriminator with the fixed threshold. The luminosity is calculated from the frequency of discriminator operation. Measurements from the electron and positron sides yield statistically independent results.

For data recording, amplitude signals are converted to logic signals whose length is proportional to the input charge. Lengths of all signals are measured by the TP-boards in the KLYukVA standard [64]. A typical spectrum of SBS signals at $E_b = 1845$ MeV is given in Fig. 41. The pedestal width and shape are determined by superposition of “tails” from previous signals. The right spectrum edge is widened due to the coincidence of γ quanta from the same turn. By spectrum form, it is possible to check on-line the monitor workability and the stability of the threshold $T = \omega_{\min}/E_b$ (see (10)).

The calculated resolution of the sandwich $\sigma(\omega)/\omega$ is determined by the following contributions: the sampling fluctuations $4.2/\sqrt{\omega}$ %, the longitudinal leakages $1.0/\sqrt[4]{\omega}$ %, and the photoelectron statistics $3.0/\sqrt{\omega}$ %, where ω is the photon energy in GeV. With $\omega = 1$ GeV, the expected resolution is 5.3%. A real resolution of the sandwich was measured by SBS events using the system of scattered electron registration (SSET, see section 13.). When scattered particles hit the SSET the photon energy is defined by the formula $\omega = E_b - E'_e$ with an accuracy better than 1%. The results are displayed in Fig. 42. Somewhat worse resolution as com-

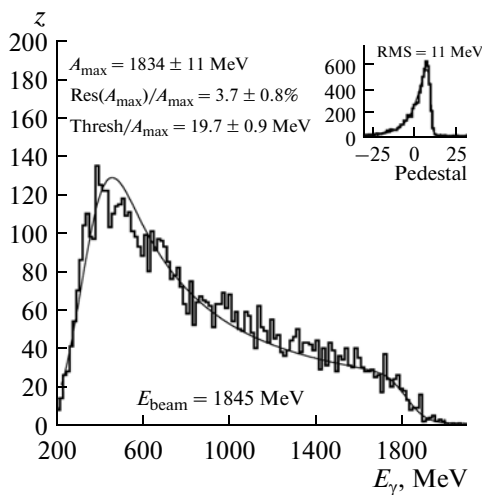


Fig. 41. The SBS spectrum used for measuring the ω_{\min} threshold.

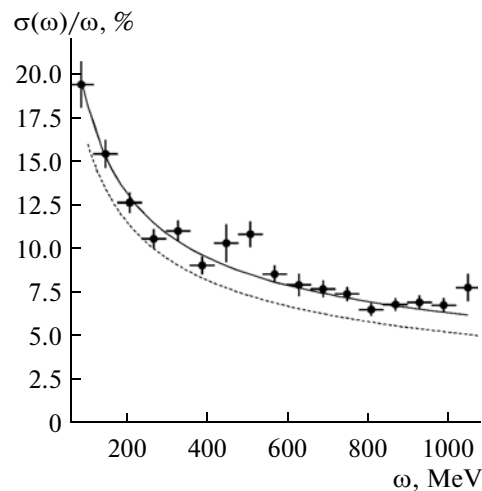


Fig. 42. Resolution of the luminosity monitor (LM) for SBS photons. Dots with bars denote experimental data, solid line presents the fit with $\sigma(\omega)/\omega[\%] = \sqrt{5.8^2/\omega(\text{GeV}) + 2.4^2}$, dotted line shows the design resolution.

pared to the design value is caused by calibration inaccuracy, signal superposition, and photomultiplier instability due to the change of the instant SBS rate.

12.3. On-Line Measurements of Luminosity

The collider luminosity in the experiment is defined by the formula

$$\mathcal{L} = \frac{(f - f_{bg})}{\sigma_{vis}} (1 + \delta),$$

where f is the frequency of monitor operation, f_{bg} is the SBS background on the residual gas, σ_{vis} is the calculated cross section of SBS registration (10), an experimentally measured, δ is the correcting factor related to the losses of SBS photons.

To tune the accelerator parameters, it is desirable to measure the luminosity with a period of ~ 10 s at the relative accuracy better than 5%. The main factors contributing to the accuracy of measurements are listed below.

- The SBS photons are removed from the VEPP-4M vacuum chamber through the window in the tungsten receiver of synchrotron radiation. With $E_b \leq 2$ GeV, the window size exceeds the SBS spot size ($\sim 1/\gamma$) by three to four times. In case of the central position of the spot, this leads to losses of $\sim 10\%$ of photons at the window edges. In reality, the losses may grow to 20–30% due to the orbit displacement in the intersection region. Because of difficulties with measuring the orbit position in the colliding bunches mode, only partial compensation for this effect was possible.

- A value of the threshold T (10) can be measured with good accuracy in each run (see Fig. 41). Because of nonlinearity of the sandwich response, the absolute accuracy of the threshold measurement $\Delta T/T$ is estimated as 10%. A contribution of the threshold error to the systematic accuracy of luminosity measurement is around 5%.

- At luminosity higher than $10^{30} \text{ cm}^{-2} \text{ s}^{-1}$, the probability of simultaneous hits of several photons into the sandwich becomes significant. Depending on the relation of T and \mathcal{L} , the counting rate can drop (two photons are counted as a single photon) or increase (two soft photons cause the trigger). In our case, a correction due to both effects is $\Delta \mathcal{L} \approx -(2-3)\mathcal{L}\%$.

- The SBS background on the residual gas f_{bg} is about (3-5)% and varies depending on the collider energy, currents of beams, and a vacuum system condition. Periodic measurements of the counting rate with the separated collider beams ($\mathcal{L} = 0$) allows to retain its contribution to the luminosity error at the level of 0.5%.

To ensure the independence of luminosity measurements on the main detector, all corrections to \mathcal{L} were determined only by data from the luminosity

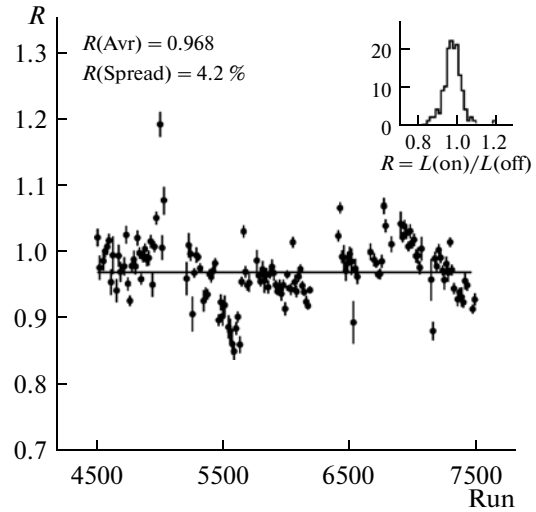


Fig. 43. A ratio of integrated luminosity from on-line measurements to that from Bhabha events as a function of the run number during 1.5 year of data taking.

monitor and SSET. The relative accuracy of luminosity measurements can be estimated by comparing measurement from the electron and positron sides $R = \mathcal{L}^- / \mathcal{L}^+ - 1$. According to results of the data taking during 1.5 year, the quantity $R = \mathcal{L}^- / \mathcal{L}^+ - 1$ had an average of $(-3)\%$ and a spread of around 3%. For the relatively short experiments (about one month), the spread of R might decrease to 1%. Thus, an accuracy of one measurement of \mathcal{L}^- or \mathcal{L}^+ may be estimated as 3%. The statistical error in this case is less than 1% per every second. This accuracy is quite sufficient for the collider tuning.

The independent estimation of the absolute accuracy of luminosity measurement was performed by comparing the integral luminosity determined by monitors with the luminosity measured from the number of Bhabha events in the endcap calorimeter of the KEDR detector. The results of comparison are shown in Fig. 43. The quantity $R = \mathcal{L} / \mathcal{L}(\text{Bhabha}) - 1$ has an average of -3.2% and a spread of 4.2%. The “distant” points appear with a substantial deviation of the angle in the intersection region from the optimal value. Taking into consideration the intrinsic error in the luminosity determination by Bhabha events (2–3%), we confirm a conclusion that for the major part of runs, an accuracy of luminosity measurement by SBS is $\Delta \mathcal{L} / \mathcal{L} \approx 3\%$.

13. SYSTEM OF SCATTERED ELECTRON TAGGING

13.1. Introduction

Together with the processes of single-photon annihilation $e^+e^- \rightarrow \gamma^* \rightarrow X$ (Fig. 44a), the two-photon processes $e^+e^- \rightarrow e^+e^-X$, proceeding via a channel with two virtual photons $\gamma^*\gamma^* \rightarrow X$ (Fig. 44b), are of great

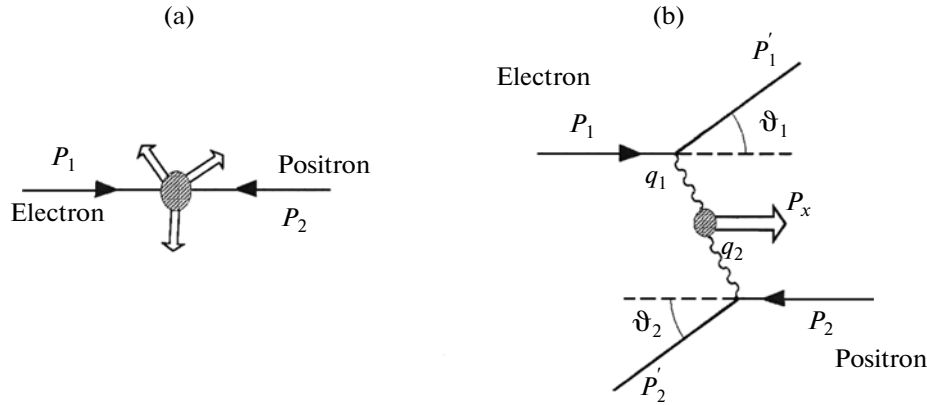


Fig. 44. (a) Annihilation of electron and positron. (b) Two-photon interaction of electron and positron.

interest. These processes make it possible to use the e^+e^- colliders for studying C -parity finite states which are not produced in the single-photon channel. Reviews of theoretical statements and state-of-the-art of two-photon physics can be found in [70–72].

The expression for the differential cross section of the process (see Fig. 44b) contains masses of virtual photons q_i^2 (see (11)). It reaches maximum when q_i^2 is close to zero. Therefore the most of the processes are characterized by small transverse momenta of participating particles and the produced system. In particular, the scattered electrons fly mainly along the beam to the nearest magnetic element of the accelerator structure.

There are two basic approaches to studying these processes. In the first case, the parameters of the produced system are reconstructed only from the products of reaction, which are registered in the central part of the detector. The smallness of the system’s transverse momentum is the main parameter for separating these events. It is the so-called no-tag method applied at the majority of detectors. It works sufficiently well for investigation of few-particle finite states of the produced system X .

If the detector can register both scattered beam particles (for brevity, we shall call them SE—scattered electrons), then we can determine parameters of the produced system regardless of the central part. It is the so-called double-tag method. The invariant mass of the produced system $M_{\gamma\gamma}$ and squares of masses of virtual photons q_i^2 with small angles of SE scattering are expressed by the simple formulas

$$M_{\gamma\gamma}^2 \approx 4\omega_1\omega_2 = 4(E_b - E_{e^-})(E_b - E_{e^+}), \quad (11)$$

$$q_i^2 \approx -E_b(E_b - \omega_i)\vartheta_i^2, \quad i = 1, 2,$$

where ω_i is the energy of virtual photons, E_{e^+}, e^- are the SE energies, ϑ_i are the SE angles, E_b is the beam energy.

In the intermediate case, the registration of a single SE (the single-tag method) gives the additional information for kinematic reconstruction in the central part of the detector and helps in the background suppression.

A majority of detectors can register SE only when the scattering angle $\geq 10^\circ$. In this case, the registration efficiency is no more than several percent, while a resolution in photon energy $\sigma(\omega)/E_b \sim 1\text{--}5\%$. The efficiency can be substantially increased with the help of the dedicated system of scattered electron tagging (SSET) that can measure the energy of SEs emerging out of the intersection region along the axis of beams.

In 1984–1985, the similar system worked on the MD-1 detector at the VEPP-4 collider. The system description and results of its work can be found in [73]. The new system of SE registration developed for the KEDR detector has the appreciably larger efficiency and an order of magnitude better resolution in invariant mass. Physical principles of the SSET project were published in [74,75]. A detailed description of the system is given below.

13.2. General Description

13.2.1. Principle of operation. Using a doublet of quadrupole lenses, which is intended for obtaining a small β -function in the intersection region, and the bending magnets, we designed the two-arm focusing magnetic spectrometer for measuring the SE energy (Fig. 45). Electrons and positrons that have lost a part of energy are ejected from the equilibrium beam orbit by the transverse magnetic field of bending magnets. In the focusing spectrometer, the particles with a certain energy irrespective of the outgoing angle fall at the fixed point on the curve of focusing. This idea underlies the SSET construction of the KEDR detector. The optical analogy of the tagging system is shown in Fig. 46.

In order to trace the focus displacement, the tagging system is divided into four separate units arranged along

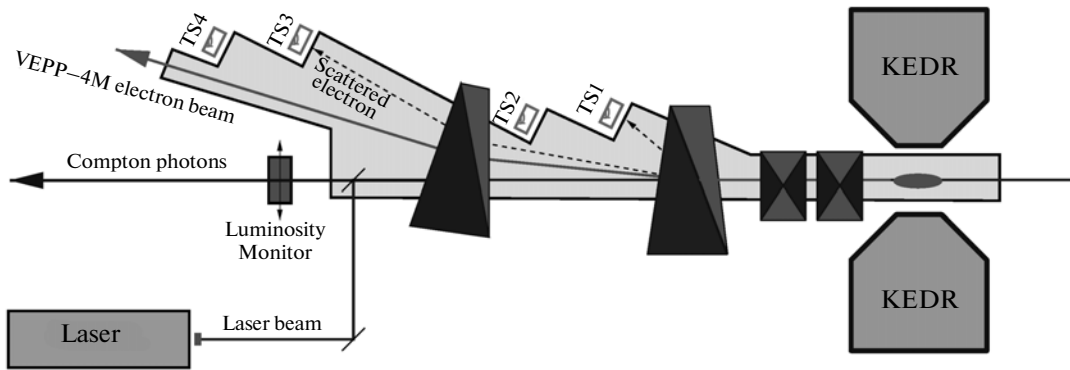


Fig. 45. Layout of the VEPP-4M experimental straight section for electron direction (top view). Behind the KEDR detector, the focusing lenses and bending magnets are placed, following which the SSET units (TS1–TS4) are located. On the left, the luminosity monitor (LM) and the scheme of the laser beam insertion for obtaining the Compton photons are shown.

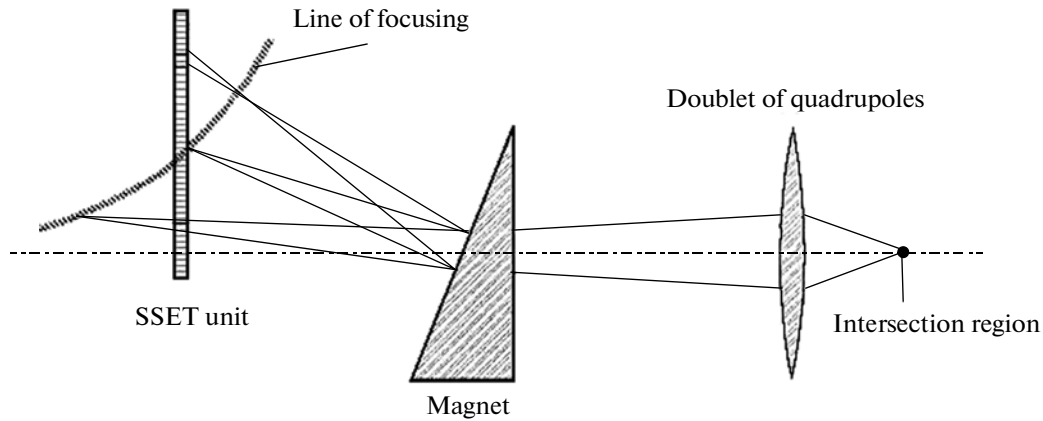


Fig. 46. Optical analogy, explaining the principle of SSET operation.

the vacuum chamber at a distance of 9–17 m from the intersection region, as is shown in Fig. 45. Each unit has its intrinsic energy of focusing E_f that is a characteristic SE energy, where the compensation for angular spread is optimal (Table 12). A contribution of angular spread to the energy resolution is minimal near the center and grows at the unit edges (Fig. 47).

There is a scintillation counter behind each unit, which is triggered by SE. Signals from these counters are used in the trigger for forming the arguments SE1 and SE2 (see section 14).

The SE energy, further denoted as E_s , is reconstructed from the track coordinate measured in SSET. The angle is used for selecting good tracks on the background of showers. An error of the SE energy measurement is determined by the coordinate resolution of the unit, the size of intersection region, the residual contribution of angular spread, and the scattering by the exit window foil and tube walls. The design energy resolution for emitted photons with all factors taken into account is shown in Fig. 47. Line 2 corresponds to the modified SSET with the use of GEM (see below).

Table 12. Design parameters of SSET units

Unit	Working area	Range of E_s/E_b		E_f/E_b	$\langle \sigma(ES)/E_b \rangle$ for 90% of SEs	$\langle \sigma(\omega)/\omega \rangle$ for 90% of photons
TS1	7.7 cm	0.39	0.59	0.59	0.996%	1.29%
TS2	4.3 cm	0.60	0.72	0.66	0.245%	0.64%
TS3	8.9 cm	0.73	0.85	0.79	0.141%	0.67%
TS4	15.8 cm	0.87	0.98	0.89	0.114%	0.81%

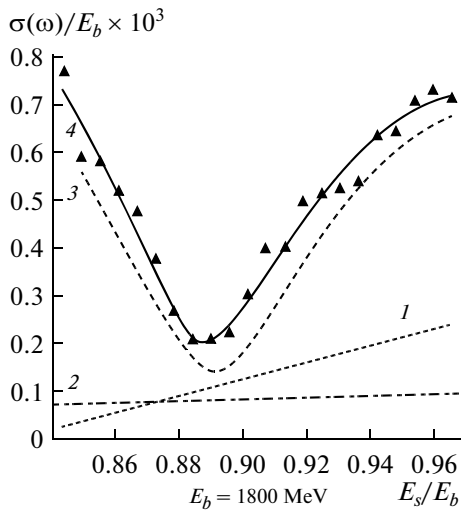


Fig. 47. The design resolution $\sigma(\omega)/E_b$ for TS4 (dots and line 4). The contributions are shown from: energy spread in the beam (1); measurement of track coordinate with an accuracy of 0.1 mm (2); angular spread in the beam (3).

13.2.2. Construction of coordinate blocks. The system consists of two sets each of four units disposed bilaterally with respect to the intersection region. Each coordinate unit is constructed as a unified rigid module. Three units have a width of around 90 mm, while one unit is 180 mm wide. The vertical system size 200 mm is deliberately redundant because the majority of scattered electrons fall within a band of ± 10 mm with respect of the orbit plane. The SSET was designed for operation under conditions of great background of the single bremsstrahlung (up to several MHz). It had to ensure a high radiation resistance and multi-track reconstruction. A hodoscope of drift tubes (independent fast and reliable detectors) was chosen.

A schematic drawing of the unit is shown in Fig. 48. Each unit contains six dual layers of vertical drift tubes that measure the SE departure from the beam axis in the orbit plane. Each layer consists of two rows of stainless-steel tubes with a wall thickness of 90 μm and a radius of 3 mm spaced at 8 mm. The tubes are secured in the openings flanges of fiberglass laminate. A distance between the layers is 48 mm. Walls of the tubes ensure the sufficient protection against the soft synchrotron radiation, their contribution to the coordinate resolution due to multiple scattering is about 0.1 mm for 1800 MeV energy.

Anode wires are made of gilded tungsten wire 28 μm in diameter and are fastened in pins with a tension of 70 g. The pins protrude from the fiberglass-laminate flanges and are connected to the chamber electronics. A contribution of the mechanical accuracy of manufacturing to the coordinate resolution is

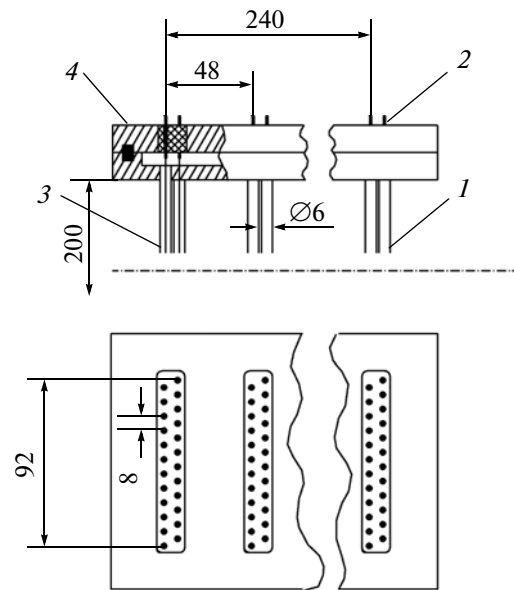


Fig. 48. Schematic diagram of the drift tube hodoscope. Numerals denote drift tube (1), anode pin (2), anode wire (3), and flange (4). The coordinate resolution of the track in the center of the unit is 0.25–0.35 mm.

around 50 μm . The anode wires are shifted relative to the tube centers by 300 μm , here a sign of displacement in the neighboring dual layers is opposite. This allows the “left-right” uncertainty in beam reconstruction to be eliminated. The chosen construction provides for 6–12 measurements of SE coordinate, which is quite enough for reconstruction of complicated events.

13.2.3. Gas mixture. All tubes in a coordinate unit form a common gas volume. For this purpose, the upper and lower flanges of the system are made double. The tubes are glued with the help of the conducting glue into the holes of the lower part, while the glass-fiber-laminate inserts with openings for pins are glued into the upper part. A gas mixture is supplied into the sealed gap between the flanges.

The SSET operates under conditions of high counting rate of emerging beam particles of the synchrotron radiation. With the luminosity $10^{31} \text{ cm}^{-2} \text{ s}^{-1}$, a total charge in the most irradiated areas can reach 1–2 C/cm for a year of operation, which may lead to the radiation ageing. Therefore the mixture $\text{CF}_4 + 10\% \text{ iC}_4\text{H}_{10}$ distinguished for its radiation resistance was selected to be used in the system. In addition to that, the electronics were adjusted to the low gas gain, around 10^5 . A dose of 7 C/cm was reached for the system prototype without the appreciable reduction in the gas gain. This guarantees four to five years of reliable operation at maximum luminosity. Additionally, to decrease the effects of ageing, the possibility of vertical displacement of units is envisaged.

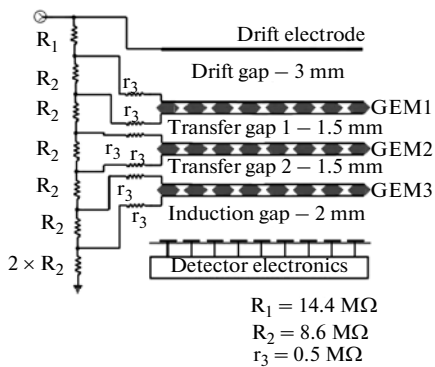


Fig. 49. A circuit of the GEM-SSET detector with a high-voltage divider. A working voltage on the detector is 3.3–3.6 kV.

13.2.4. Recording of signals. A high voltage is supplied to anode wires through the $0.3 \text{ M}\Omega$ resistors for channel-to-channel signal decoupling. The wire signal is supplied to the preamplifier input through the 0.6-nF blocking capacitor that transmits useful signals without distortion. Each unit is supplied from a separate high-voltage source. The working voltage is selected for each unit individually (until a good efficiency to the track is obtained) and amounts to 1.9–2.2 kV.

Chamber electronics is performed in the form of standard mechanically protected modules that are put with contact sockets on anode pins and secured to the SSET flanges. Each module of chamber electronics comprises 12 independent channels. A signal from the wire is amplified with the help of the low-noise preamplifier and then is supplied to the amplifier-shaper, whose threshold is controlled by the external voltage. The signal duration after the preamplifier is around 30 ns, dead time after the operation is around 60 ns, and the minimum threshold permits the operation from a single initial electron to be performed. The total number of the system channels is 1440.

An output logic signal is supplied to the counting room for measuring the drift time. Time is measured with the help of the T-board [64] with a discreteness of 2 ns with the maximum drift time around 30 ns. The counting in each channel begins on signal arrival and continues until the general signal “stop” comes from the trigger. If “stop” does not come after 512 counts (the time of the beam revolution), then “reset” is performed, after which the channel is again ready for receiving the next signal. A contribution of electronics to the coordinate resolution is 0.12 mm. The efficiency of the majority of tubes is 95–100%. For the most part, the efficiency loss occurs due to faults of electronics and (at high counting rate) from the cross-talk between the neighboring channels. Even with the 90% efficiency of every tube, the track loss probability is no more than 1%. A resolution of a single tube is 0.2–0.5 mm depending on voltage. The resulting res-

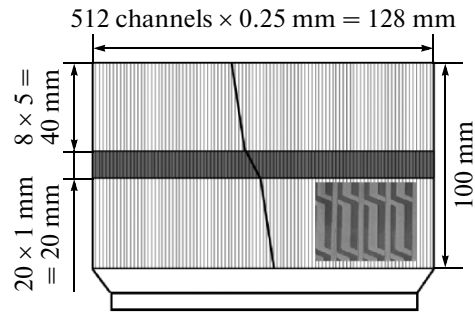


Fig. 50. The readout board design with a variable angle of strip slope. The magnified scheme of two-layer readout structure is shown in the inset. Straight strips are main channels, bent strips are stereo channels.

olution for the track coordinate at the unit center is 0.25–0.35 mm for conditions of low counting rate. Under conditions of a real experiment, the resolution is around 0.4 mm due to cross-talk and signal pile-up. A horizontal angle resolution is around 3 mrad.

13.3. Detectors based on three-GEM stage. For modernization of the tagging system, it was decided to equip each module with two-coordinate high-resolution detector arranged in front of the drift tube hodoscope. For this purpose, a comparatively new detector type based on multistage gas electron multipliers (GEM) was selected [76]. This enables the SSET coordinate and energy resolutions to be improved. A resolution for vertical SE angle is appreciably less than the natural SE spread, therefore the SE vertical coordinate can be used for suppressing the background of single bremsstrahlung.

Detectors based on gas electron multipliers for SSET (GEM-SSET) include a cascade of three GEMs located 1.5 mm apart, as is shown in Fig. 49.

Each GEM has hexagonal structure of holes $80 \mu\text{m}$ in diameter spaced at $140 \mu\text{m}$. The distance between the bottom GEM and the readout strip structure is 2 mm; the distance from the top GEM to the high-voltage drift electrode is 3 mm. To minimize the damage from breakdowns and short-circuits, the electrodes of each GEM are divided into vertical segments 10 mm wide with a shift by 5 mm for the GEM top and bottom (according to Fig. 49) sides. Every segment is connected to the high-voltage divider through the $0.5 \text{ M}\Omega$ series resistor.

The strip structure (Fig. 50) ensures the two-coordinate readout of the signal, at which the channels in the accelerator orbit plane are arranged 0.5 mm apart, while the channels in the perpendicular direction are 1 mm apart in the central part of the detector ($\pm 10 \text{ mm}$ around the orbit plane) and spaced at 5 mm beyond the central part. A vertical coordinate is determined by a difference in channel numbers in the direct and stereo layers. This scheme ensures a good resolu-

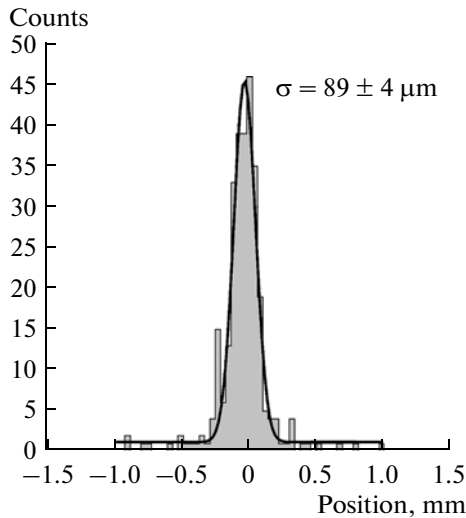


Fig. 51. Distribution of difference between the measured and interpolated track coordinates in the middle detector out of three GEM-SSET detectors under study. A spatial resolution of a single detector is $\approx 73 \mu\text{m}$.

tion in vertical near the horizon maintaining a good multi-track identification.

Two types of GEM-based detectors were fabricated similar to SSET units based on drift tubes. Stations TS4 (see Fig 45.) are equipped with detectors with a size of sensitive area of $256 \times 100 \text{ mm}^2$; stations TS1–TS3 were equipped with detectors with a size of $128 \times 100 \text{ mm}^2$. Large detectors have 512 channels in each layer; the TS1–TS3 detectors contain 256 channels in each layer. The detectors operate with the gas mixture $\text{Ar} + 25\% \text{ CO}_2$.

Each strip of the readout structure is connected to input of the uncased chip that contains 128 analog channels including the low-noise amplifier-shaper as well as the analog multiplexer that enables the content of all channels to be read out sequentially at a frequency of 1 MHz. The detector electronics comprises four or eight such chips, depending on the number of channels. At every collision of electrons and positrons, an output signal of amplifiers-shapers in all channels is stored. If a signal from the first-level trigger comes after this, a process of readout and digitization is triggered.

The readout and digitization occur under control of two control units, one on the electron side, another on the positron side. The readout and digitized data from the control unit memory are transmitted to a computer via Ethernet lines at a rate of 100 Mbit/s. Once an event has been read out of detectors, digitized, and transmitted to a computer controlling the system operation, pedestals are subtracted from the data, the channels containing no data are removed (suppression of zeros), and the remaining useful portion of the data is transferred to the central computer of the data acquisition system. The total time for event

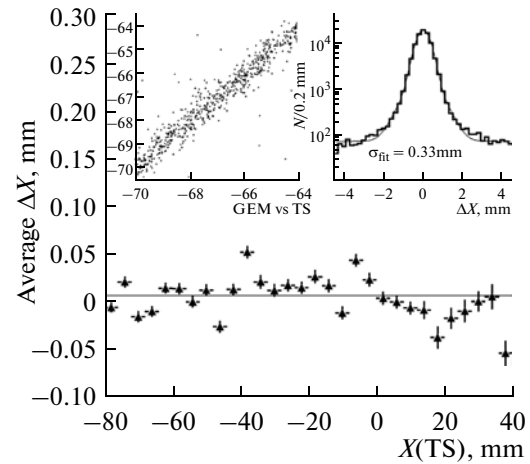


Fig. 52. The comparison of the old and refined values of the track coordinate is illustrated in the figure. The correlations of both measurements X and their difference are presented in the insets. In the distribution over ΔX , 90% of events lie inside the Gaussian distribution with $\sigma = 0.33 \text{ mm}$.

processing without taking into account the time spent for the data transfer to the data acquisition system is no more than 2 ms. The more detailed description of arrangement of the GEM-SSET detectors and the system of control and data acquisition is presented in [77–79].

Basic characteristics of GEM-SSET detectors were measured at the dedicated test-bench on cosmic particles [78]. The test-bench consisted of three identical GEM-SSET detectors and two triggering scintillation counters. Two detectors were used for track localization, while the middle detector was applied for investigation of characteristics. Figure 51 displays the distribution of the difference between the measured event coordinate in the detector under study and the calculated coordinate of the point where the track crosses the detector plane. A width of the distribution $\sigma_{\text{meas}} = 89 \mu\text{m}$, which corresponds to the resolution of a single chamber $\sigma_{\text{det}} \approx \sigma_{\text{meas}}/\sqrt{3/2} \approx 73 \mu\text{m}$ in the orbit plane. The similarly measured resolution in vertical direction is $220 \mu\text{m}$ for the central zone. The efficiency of GEM detectors under the working voltage is 95–98%.

New detectors are used for refining parameters of tracks. A track from SSET continues to GEM-SSET, the nearest two-dimensional tag is fixed to it, and the track refitting is performed with account for the added data. In this case the plane of measurements of the transverse coordinate X is shifted from the SSET unit center to the GEM-SSET plane. Apart from the improvement of the coordinate resolution from 0.3 to 0.1 mm, this shift reduces a contribution from multiple Coulomb scattering in the exit window foil of the vacuum chamber and in tubes. The results of using

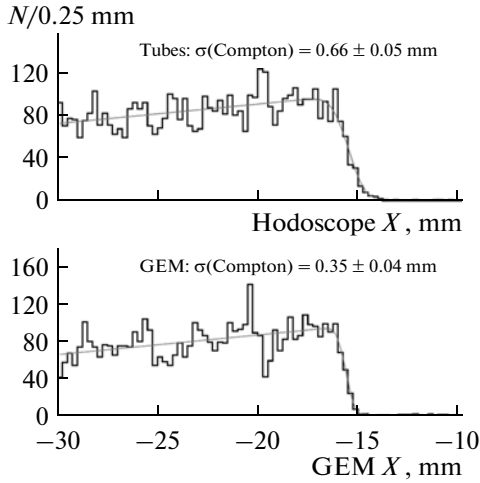


Fig. 53. Event distribution over the SE coordinate X_r measured in SSET. The use of GEM-SSET substantially improves the resolution. The edge width 0.35 mm corresponds to the energy resolution $\sigma(E_S)/E_b = 0.25 \times 10^{-3}$.

together the hodoscope and GEM-SSET are shown in Fig. 52. The old track coordinate $X(TS)$ and the new one $X(GEM)$ are compared. According to the coordinate difference ΔX , 90% of events fall inside the Gaussian distribution with $\sigma = 0.33$ mm (this value increases to 0.45 mm for high counting rate). A systematic difference for the most part of detector is no more than 0.1 mm. In some local regions (detector edge and boundaries of high-voltage segments), the systematics may grow to 0.5 mm. This, in particular, is revealed in periodic (with a pitch of 5 mm) “deeps” in the observed spectra (Fig. 53, lower part). Now the work in improvement of the track reconstruction algorithm is in progress.

13.4. Measuring Energy Resolution of SSET

In order to achieve the high energy resolution in SSET, it is necessary to know geometry of the entire system with an accuracy of around 0.1 mm. Meanwhile, during the tuning of the collider energy, a beam orbit may displace by a value of around 1 mm. For precise SSET calibration, a dedicated system has been used in the experiment, which is based on the process of the Compton backscattering (by 180°) of monochromatic laser photons by beam electrons. This system makes it possible to directly calibrate the dependence of SE coordinate on its energy and additionally to measure the energy resolution.

A spectrum of scattered photons is the relatively flat plateau with a sharp edge with the maximum energy (at head-on collision):

$$\omega_{\max} = \frac{4\gamma^2\omega_0}{1 + 4\gamma\omega_0/m_e}, \quad (12)$$

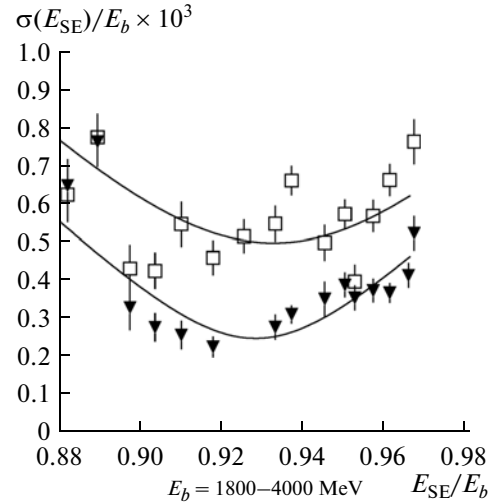


Fig. 54. The energy resolution $\sigma(E_S)/E_b$ measured at the Compton spectrum edge at different beam energies. Square symbols are obtained using tubes alone; triangular symbols correspond to application of GEM.

where ω_0 is the energy of the initial photon, m_e is the electron mass, $\gamma = E_b/m_e$ is the relativistic factor of a beam. Thus, using optical lasers with $\omega_0 = 1-2$ eV, we obtain photons with $\omega_{\max} = 40-800$ MeV at $E_b = 1.5-5.0$ GeV.

The SE energy lies in the range from $(E_b - \omega_{\max})$ to E_b . The distribution over the SE coordinate measured in SSET (in the orbit plane) is shown in Fig. 53.

Since energy of laser photons is known with a precision of $\sigma(\omega_0)/\omega_0 \sim 10^{-7}$, while the beam energy can be determined with a precision better than 10^{-4} , we obtain a possibility of precise calibration of the coordinate–energy dependence. The spectrum edge degradation near the energy $(E_b - \omega_{\max})$ is fully determined by the SSET energy resolution. For the first time, the SSET parameters were measured using this method during the test runs on calorimeter prototypes for the BELLE detector in 1996–1999 [80–82]. However since then, the VEPP-4M magnetic system near the intersection region was changed, therefore a new energy calibration was required.

A new system of laser calibration was assembled and put into operation in 2010. Two lasers produced photons with energies of 1.165 and 2.33 eV. By varying the beam energy within the limits of $E_b = 1.8-4.0$ GeV, we measured the SSET resolution at ten points corresponding to energies of scattered laser photons from 50 to 500 MeV. Figure 54 presents the resolution measurements taken with the hodoscope alone (squares) and with the use of GEM-SSET (triangles). The appreciable improvement of resolution can be seen for the modernized system. The dots drop-outs are explained by local errors of measuring the SE coordinate and influence of the lost particle showers from the beam pipe.

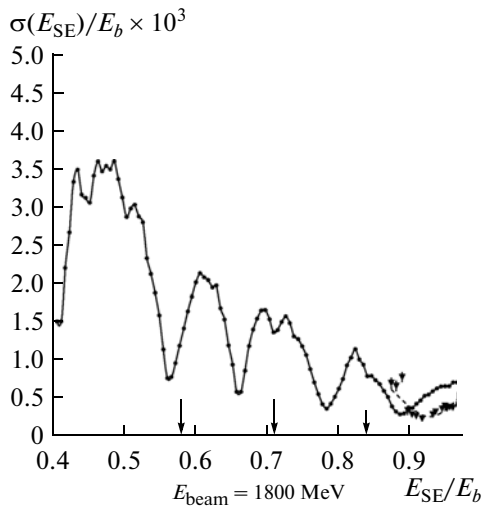


Fig. 55. The energy resolution of SSET for a scattered electron at $E_b = 1.8$ GeV. Dots with bars display the resolution measured in the experiment. Boundaries of SSET units are marked by arrows.

13.5. Physical Parameters

Parameters of the registration system depend in rather a complicated way on the VEPP-4M magnetic structure, accelerator beam parameters, and energy of a scattered electron. Results of energy resolution calculation for SE are given in Fig. 55 for the beam energy 1.8 GeV; dots with bars show the measured resolution. The difference of measurements from the calculation indicates that the collider model used in calculations is somewhat different from the real collider. The adjustment of the magnetic-system parameters used in calcu-

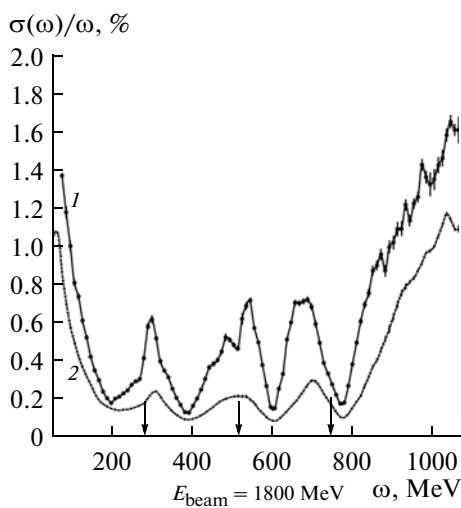


Fig. 56. The energy resolution $\sigma(\omega)/\omega$ for an emitted photon: for virtual photons in two-photon events (1) and for real photons in SBS events (2).

lations is necessary, which is planned to do in the new season.

Figure 56 displays the expected resolution in photon energy. The upper curve characterizes the resolution for two-photon processes, while a lower curve corresponds to real photons of single bremsstrahlung. The resolution for real photons is significantly better than resolution for virtual photons due to the smaller angular spread of the emitted photons. As it can be seen from the plots, the tagged photons can be obtained with a resolution around 0.3% within a wide energy region. These photons may be used for calibration of calorimeters [59, 81] and for physical experiment [83, 84].

The relative resolution for energy of 5 GeV deteriorates by 1.5–2.0 times because the angular and energy spreads in the beam grow as the square of energy.

The calculated energy resolution in the invariant mass $M_{\gamma\gamma}$ for events with registration of two SEs is shown in Fig. 57. Due to the presence of non-Gaussian tails, the resolution was determined with a width of the distribution $\Delta M = M_{\gamma\gamma} - M_{MC}$ as $\sigma = \text{FWHM}/2.36$. Here $M_{\gamma\gamma}$ is calculated by Eq. (11), M_{MC} is the invariant mass of $\gamma\gamma$ system in simulation. The expected resolution is on the order of magnitude better than those of other similar systems.

Figure 58 illustrates the efficiency of registration of the $\gamma\gamma$ event with a good measurement of energy ($\Delta M < 2.5\sigma$) for the beam energies 1.8 and 5 GeV as a function of the invariant mass of the produced $\gamma\gamma$ system.

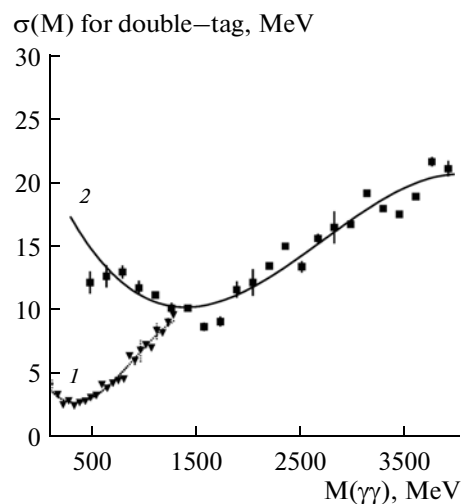


Fig. 57. The expected resolution in the invariant mass in the $\gamma\gamma$ system in the double-tag experiment for $E_b = 1.8$ GeV (1) and $E_b = 5$ GeV (2).

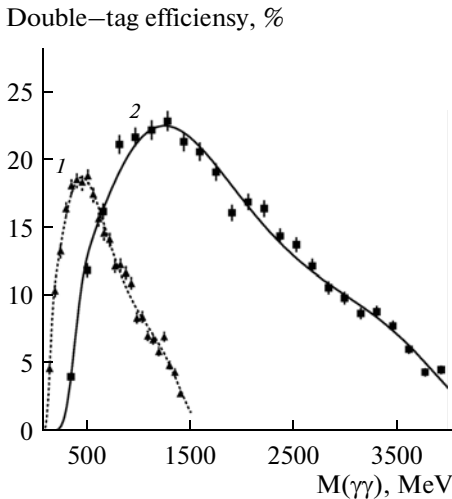


Fig. 58. The probability of double-tag reconstruction of the $\gamma\gamma$ event at $E_b = 1.8$ GeV (line 1) and $E_b = 5$ GeV (line 2).

14. TRIGGER

The trigger’s task is to select from the entire bulk of events only those corresponding to the processes under study. All remaining events are background ones and must be if possible rejected, while the counting rate at the trigger output should be acceptable for processing the data stream on computers and for subsequent writing to the disk.

The hardware trigger of the KEDR detector [85] has the two-level structure. It includes the first-level (primary) trigger (PT) and second-level (secondary)

trigger (ST). The third-level trigger is a software one. The time diagram of trigger operation is shown in Fig. 59.

14.1. Algorithm of Trigger Operation

The primary trigger of the KEDR detector makes a decision within 450 ns (see Fig. 59). This time is less than an interval between beam collisions in the VEPP-4M ring (620 ns); therefore PT has no dead time.

The first-level trigger of the KEDR detector has only one signal—“PT decision” (“PT”). It arises if the current event corresponds to the selection requirements. The “PT” signal is synchronized with the rf signal “Phase” of the accelerator and is a time tag, with respect to which arrival time of the signals from detector channels is measured. The pulse “PT” is also a signal to the beginning of the second-level trigger operation (see Fig. 59), which has much more time for decision making and uses the information from all track subsystems of the KEDR detector and calorimeters. Duration of the total ST work is 18 μ s.

The second-level trigger of the KEDR detector has two decisions: “ST+” and “ST-“ (see Fig. 59). If ST finds no required signatures in the event, then following 18 μ s after the “PT” signal arrival, it outputs the signal “ST-“. In reply to this, a pulse “Reset” is generated in the data acquisition system (DAQ), by which the data are cleared in all information boards (IBs), the PT and ST itself are reset. The time and amplitude measuring that has begun are aborted, and DAQ together with the triggers are again ready for the reception and processing of a new event. If ST classifies this

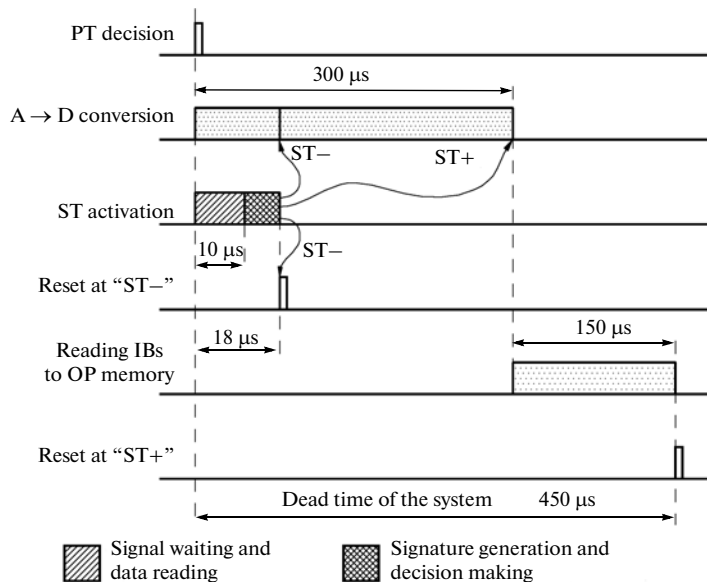


Fig. 59. The timing diagram of communication between the activation of the trigger and the data acquisition system of the KEDR detector.

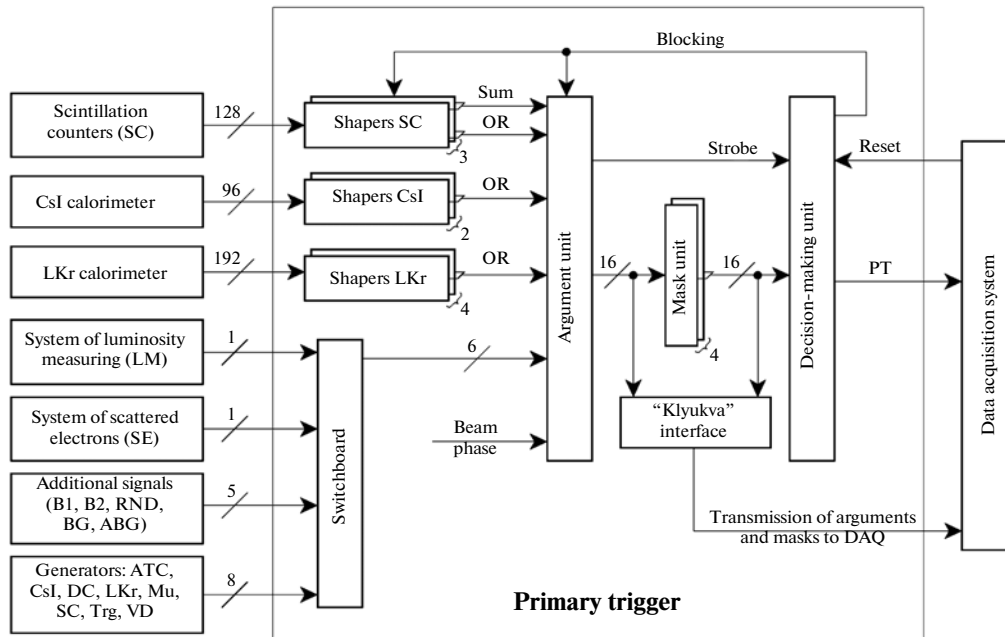


Fig. 60. Block diagram of the primary trigger.

event as useful, then it issues a signal “ST+” with a delay of 300 μ s, rather than immediately, to provide time for digitizing units of electronics to complete measurements of time and amplitudes. By the signal “ST+”, the process of data readout to the memory of output processors (OPs) is triggered. Once all the data from all IBs are read, a signal “Reset” is generated and the system is preparing to accept a new event from the detector.

14.2. First-Level Trigger

Units of PT electronics are arranged near the detector. It is optimal in view of the time of receiving the “PT decision” signal. They are performed in the CAMAC standard and occupy two crates and a half.

Three subsystems of the KEDR detector are signal sources for PT: (i) the time-of-flight system based on scintillation counters (SC), (ii) the endcap calorimeter based on crystals of cesium iodide (CsI), and (iii) the barrel calorimeter filled with liquid krypton (LKr).

The PT units form three sums of the number of operated counters (one for the barrel part and two for the endcap parts) from the SC signals and a pulse with 470-ns duration from the logic OR of all channels. Moreover, if for the barrel part, a sum of all inputs, at which a signal has appeared, is simply calculated, then for the endcap counters the sums for non-adjointing hit channels are calculated. This is associated with a small geometric size of the end SCs near the beam and, as a consequence, with an increased probability of hitting two adjoining counters from a single particle passed through.

A size of trigger channel in the calorimeter must be consistent with the size of the shower of particles developing in the detector. Therefore individual CsI crystals are combined in groups containing from 24 to 28 CsI crystals, which are called supertowers (SuT). In total, there are 48 SuTs, 24 in each endcap. Analog pulses from individual crystals are summed to generate a signal from SuT. Further it is split into two signals. One of them is used in the ST, while another is supplied to the discriminator with a regulated threshold for the PT. The background load of CsI crystals depends strongly on a distance from the beam axis. Therefore all SuTs are divided in three groups in the form of different-radius rings, and for each ring there is a particular threshold for the PT discriminators. Two signals from CsI are used in the PT: one from each endcap, both being logic OR of all discriminators.

In the barrel electromagnetic LKr calorimeter, towers of the first two layers are combined in supertowers for using in the trigger. There are in total 192 SuTs, each consisting of eight LKr towers: $2 \times 2 \times 2$ in all three coordinates (r, ϕ, z). Signals from them generated in 1 μ s are supplied to the discriminators with regulated threshold. This large time of generation is chosen to decrease the discriminator noise. However, since this time is larger than the time of signal registration in the PT (350 ns), then low-amplitude signals from LKr SuTs are not used in the PT. Therefore, the LKr threshold in the PT is determined rather by time than by the discriminator threshold and amounts to 300 MeV. There is only a single signal in the PT from the LKr calorimeter: OR of all discriminators of supertowers.

Table 13. Arguments of the first-level trigger

No.	Argument	Argument expansion
1	CSI1	OR of ST signals of left end of CsI calorimeter
2	CSI2	OR of ST signals of right end of CsI calorimeter
3	LKR	OR of ST signals of LKr calorimeter
4	SC1	OR of scintillation counter signals
5	SCB1	OR of SC signals in the barrel part
6	SCE1	OR of SC signals in the endcaps
7	SCE2	≥2 SCs in the same end or in both endcaps
8	SC2	≥2 SCs in the entire detector
9	SC3	≥3 SCs in the entire detector
10	SC4	≥4 SCs in the entire detector
11	LM	Attribute of triggering of luminosity monitor of the accelerator
12	SE	Attribute of triggering of the system of scattered electrons
13	ABG	Anti background – the absence of triggering of the CsI supertowers nearest to the beam
14	BG	Inversion of the previous signal
15	B1	Signature of the first bunch of particles
16	B2	Signature of the second bunch of particles
17	RND	Random argument—signal with a frequency of ~3 Hz
18–25	GEN_...	8 generator arguments for detector systems serving for verification of registration electronics

In total, the PT receives 128 signals from SCs, 48 from the CsI calorimeter, 192 from the LKr calorimeter, 7 signals from other detector systems, and 8 signals from the generators. From these signals, the event signatures called arguments are formed using which the selection of useful events occurs. The arguments included in the PT are given in Table 13.

The PT electronics can operate simultaneously with 16 arguments in all. Therefore, the first ten described arguments are always present in the trigger, while the remaining 15 arguments are switchable. That is only six of them can be used in the trigger simultaneously.

The formed arguments are compared with the pre-set masks. A mask is the word, consisting of 0 and 1, in which every bit corresponds to one of the arguments. For the mask operation, it is necessary the presence of all arguments, to which 1 corresponds in the mask. Thus, a mask is, in essence, a logic product of arguments. The presence of redundant arguments, not included in the mask, is admissible. A mask can have the form $SC2 * CSI1 * ABG$; this means that the trigger will select only the events, in which two SCs (SC2) and at least one supertower in the left part of the CsI calorimeter (CSI1) have operated simultaneously and there have been no operations of the CsI crystals nearest to the beam (ABG).

Results of comparing arguments with masks are united by OR; otherwise, masks create a logic sum (the PT formula). At present, in data taking from beams, the following formula is used:

$$B1 * B2 + SC2 + CSI1 * SC1 * ABG + CSI2 * SC1 * ABG + CSI1 * CSI2 + LKR + RND + LM + SE * CSI1 + SE * CSI2 + SE * SC1$$

To generate the PT positive decision, the operation at least one product (one mask) in the formula is necessary. Maximum number of masks in the PT is 16. The comparison of masks and arguments occurs in mask units. The comparison results are transferred to the “Decision Unit” that generates the signal “PT”.

The information on operation of PT arguments and masks is transmitted to the DAQ KLUKVA in order that readout of these data together with the information on the event was possible.

14.3. Second-Level Trigger

The second-level trigger (Fig. 61) is installed in the KEDR counting room, where all digitizing electronics of the detector is concentrated. It occupies five CAMAC crates, and several tens more second-level trigger interface (SLTI) units are distributed over the KLUKVA crates. The second-level trigger receives

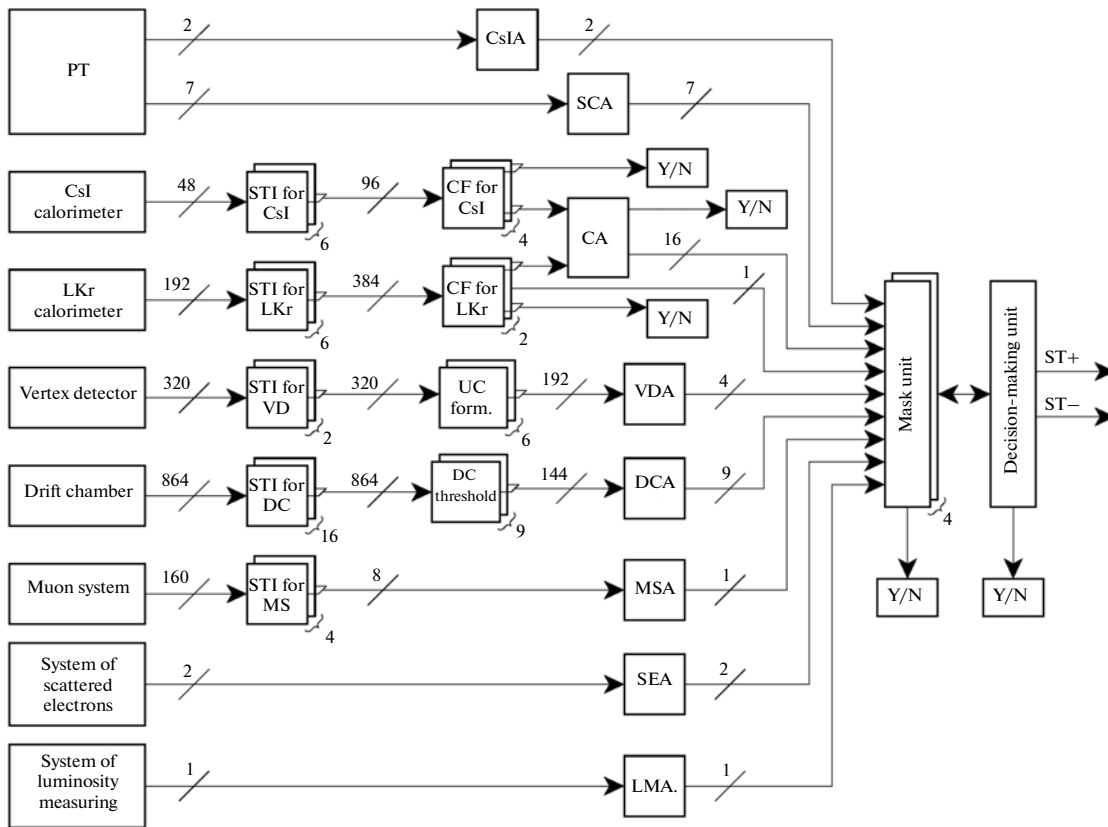


Fig. 61. Block diagram of the secondary trigger.

signals from all subsystems of the KEDR detector with the exception of aerogel Cherenkov counters.

From 312 drift tubes of the vertex detector (VD), the trigger's 192 universal cells (UCs) gathered in three superlayers are formed. The vertex-detector argument unit (VDA) determines a number of non-adjacent UCs in each VD superlayer. Then a total sum is calculated and the arguments VD2, VD3, VD4, and VD5 are produced with the help of majority-vote logic. They mean that no less than 2, 3, 4, or 5 UCs operated respectively.

From the drift chamber (DC), the data from axial layers only arrive to the ST. Now only three of them are used: the first, third, and fifth DC layers. Units of digital DC discriminators (DCD) count a number of operated wires in each DC cell and compare it with the preset threshold. A cell is considered to be activated if there are signals in it from two or more wires. Signals on DC cells activation enter the DC argument unit (DCA) that determines a number of operated non-adjacent cells in each layer. Next, the majority-vote logic generates the arguments DC11, DC12, DC13, DC21, DC22, DC3, DC31, DC32, and DC33. The first numeral in the argument name means a layer number, while the second one denotes the minimum guaranteed number of operated non-adjacent cells. For example, the argument DC22 indicates that no

less than two non-adjacent cells have been activated in the second layer.

Arguments of scintillation counters are formed by the SC argument unit (SCA). Six event signatures are provided for this system. The intermediate PT signals are used for generating arguments. First, these are signatures of the number of activated SC channels: SC2, SC3, and SC4. They are used both in the first-level trigger itself and in the second-level trigger. The following arguments are also formed in the ST.

- ASCB is the signature that for 500 ns after the interaction moment, no scintillation counters have operated in the cylindrical (barrel) part. This argument is required for anti-coincidence in case of the GEOM signal activation in the barrel calorimeter.

- ASCE is the same for the endcap SCs. This argument is needed for anti-coincidence in case of the endcap calorimeter operation.

- SC1F is the signature of the SC signal coincidence with the beam phase with a resolution time of 60 ns. Since a period between beam collisions is 620 ns, the use of this argument allows suppression of cosmic rays by a factor of 10 and more.

From analog signals of 48 SuTs of the CsI calorimeter, logic signals on excess of two thresholds (P1 and P2) are generated for the ST. For each of the calorim-

eter endcaps and for every threshold, a number of activated clusters is counted in cluster-finder (CF) units (CsI CF).

For the LKr calorimeter, 192 signals from SuTs are also compared with two thresholds. The results of discriminator operation are used in LKr CF. The argument GEOM is also calculated in LKr CF. If there is at least one activated cell within any 240° angle of ϕ , then the argument GEOM is set to 1.

Six numbers that are sums of spots from four CsL CFs and two LKr CFs enter the calorimeter argument (CA) unit. Here they are used to evaluate sums of number of clusters for each threshold: individually for the endcap calorimeter and together in both calorimeters. Next, from the obtained information, the arguments are generated: ST11, ST12, ST13, ST14, SE11, SE12, SB11, SB12, ST21, SE21, SB21, ST22, and SB22. The second letter in names of these arguments indicates to the system: “T” denotes the entire calorimeter, “E” means the endcap calorimeter alone, and “B” stands for the barrel calorimeter. The first numeral refers to the threshold P1 or P2. The second numeral denotes the number of clusters. Another argument, STEE, appears if there is a SuT with the threshold P2 in both endcaps.

In the muon system, the data from the first layer only are used in the ST, from which a simple argument—logic OR of the layer cells is generated.

For the system of scattered electron registration (SSET), two arguments SE1 and SE2 are formed in the ST. The first one appears if at least one scintillation counter of SSET on any side has operated, while the second argument appears if counters on both sides have operated.

The system of luminosity measuring transmits to the ST only one argument—LM that is logic OR of the signals from the left and right parts of the luminosity monitor.

In all, the ST has 64 arguments that are generated by the appropriate units. Now 43 of them are used, the rest are reserved for future application. The number of masks included in ST electronics is 48 but only 39 of them are checked now for the sake of shortening the time of operation.

During the operation, the ST forms a lot of intermediate information that is to be read together with the event. These are 64 arguments, 48 masks, sums of spots from six CFs, 384 bits on the SuT activation with thresholds P1 and P2 in the LKr calorimeter, and 96 bits from CsI CFs. These data are needed to check the functioning of the trigger and electronics that supply signals from detectors and measurements of the channel operation frequency.

Dead time of the trigger. The operation time of the KEDR detector PT is less than a period of beam collision; therefore, it processes every beam event and has no dead time. Its contribution to loss of events (counting errors) occurring due to dead time is zero.

A value of counting losses of the KEDR detector DAQ and trigger are determined by the formula

$$\text{Losses} = \tau_{\text{ST}} F_{\text{PT}} + \tau_{\text{IB}} F_{\text{ST}}.$$

Here F_{PT} and F_{ST} are the activation frequencies of the PT and ST respectively, τ_{ST} is the ST dead time, τ_{IB} is the information-board dead time, in which the time of data digitization and readout in the output processor is included.

The PT and ST counting rates with the fixed formulas depend on energy and beam current, as well as on the background situation at the accelerator. In the course of scanning ψ' and $\psi(3770)$, the detector load from the background events was 50 kHz. Here, mean frequencies of PT and ST operations were 3.5 and 50 kHz. This implies that two stages of the triggers suppressed the background by a factor of 1000. In this case the ST losses are 6.3%, the DAQ losses are 2.3%. Thus, total DAQ losses are 8.6%, while its efficiency is 91.5%.

The identification efficiency for the useful events in the trigger depends on the event type. For the physical processes investigated at the KEDR detector, it amounts to 98–99%.

15. DATA ACQUISITION SYSTEM

15.1. Layout of Data Acquisition System

Electronics of the data acquisition system at the KEDR detector is based on the KLYuKVA standard developed at the BINP. The number of electronic channels without the GEM system is around 15 thousands; the GEM system contains 5120 analog channels of slow control. Events are recorded at a frequency of 50–100 Hz. An average size of the event recording is 2–4 kB; around 160 bytes from them fall at GEM. A data stream is divided into separate files (“runs”) containing approximately 300 thousand events each (around one gigabyte).

After writing, the run files are compressed with the help of the standard archiver bzip2 [86], which enables their sizes to be nearly halved. The primary data are stored in three copies at independent data storages. A total volume of a single copy of compressed raw data received by the summer 2012 is 3.8 TB.

15.2. Electronics

The electronic equipment of the data acquisition system may be divided into the chamber, recording and processing apparatus.

The chamber electronics is arranged at a minimum distance from the detector and serves for amplification of primary signals and their shaping. The recording apparatus receives signals from the chamber electronics, converts them to the digital form, and selects the useful information and stores it. In the processing apparatus, the complete or partial processing of the

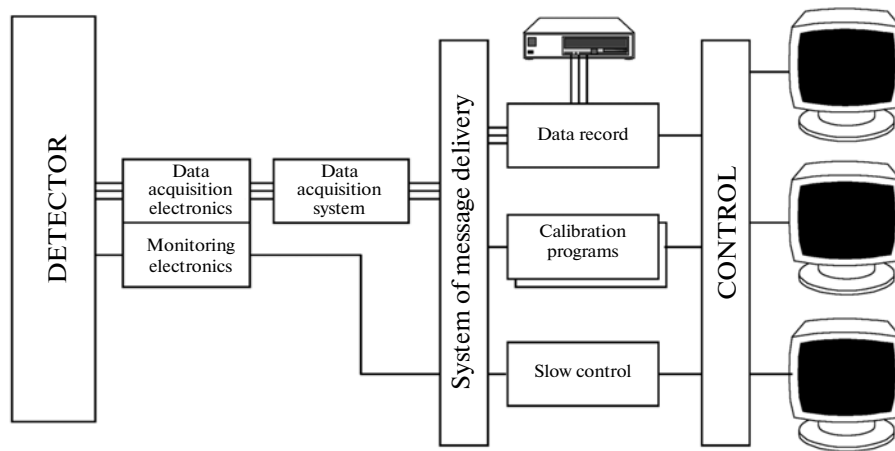


Fig. 62. Block diagram of the experiment software.

data arriving from the recording electronics and its accumulation on the long-term storages (disks and tapes) occurs.

The data acquisition system of the detector is based on the dedicated crates of the KLYuKVA standard developed in the BINP for the KMD-2, KEDR, and SND detectors [52, 36, 51]. Each dedicated crate contains 16 information boards (IB) designed for digitization of incoming data and the servicing boards: ST interface (STI), replicator of service signals (RSS), and the output processor (OP).

Synchronization and control of the system of several dedicated crates is performed by the separate CAMAC module called SCC (Synchronization and Control Center) whose signals are supplied to KLYuKVA modules through the RSS boards.

15.3. Computer Infrastructure

Data acquisition and the cryogenic and slow control at the KEDR detector is provided with 17 computers under control of OS GNU/Linux and 2 VAX/VMS computers.

In the absence of access to external resources, there are 20 computers under control of GNU/Linux for the data analysis and processing, which are located directly on the territory of the counting room of the KEDR detector and in the neighborhood.

A part of computers is chosen exclusively for execution jobs in the batch mode. The Sun Grid Engine software [87] is used as a system for batch job control.

All computers used for data acquisition are connected to a dedicated Ethernet network with a bandwidth of 100 Mbit/s.

To ensure access to data of disk servers, the network file system (NFS) is used everywhere. The user directories with files are mounted to all computers allocated for analysis. Within the KEDR detector infrastructure, approximately 13 TB of disk space is also available

using NFS, which are divided among four file servers, on which raw data, simulation files, and the files obtained as a result of analysis are stored.

Apart from public resources, there are separate servers intended exclusively for the data backup (7 TB) and for the KEDR detector database.

15.4. Software

A software layout of experiment with the KEDR detector is given in Fig. 62.

The experiment software is divided in several layers:

- low-level real-time processes that directly interact with the detector apparatus;
- a system of data acquisition, filtering and data storage;
- application programs of calibration and monitoring;
- a management system linking all tasks of application level.

The system level of the software consists of several components:

- a system of application task management, which provides run of application-level programs, their maintenance, operator's access to their data and functions;
- means of intertask communication (system of message sending), providing for means of exchange of data and control signals between tasks including those at different computers of the facility;
- means of software and hardware interface (data acquisition system, system of slow control).

A flowrate of experimental data from the detector apparatus after the preliminary hardware selection reaches 1 Mbit/s. A requirement of real-time processing is imposed only on the tasks that directly interact with the detector apparatus. In implementation of application-level tasks, possible delays in data transfer

via the local network are taken into account and additional mechanisms are used to guarantee that the high-level software will not interfere with the privileged processes related to data acquisition.

Run of all software applications of the experiment monitoring and control is coordinated using a dedicated system of process control. The system enables an operator from any computer of the facility to gain access to the data of any running process, to transmit and receive data, and to run and suspend tasks. The operator gains access to the system by means of the custom PILOT code. In the system of process control, about 40 application programs of different purpose are registered.

Based on the recorded data, the electronic logbook of data taking is filled; the daily, weekly, and seasonal reports are generated automatically. The collected and recorded integral luminosity, the detector efficiency, the mean instantaneous luminosity of the accelerator facility, a fraction of time spent for different processes of the facility (energy calibration, calibration of detector systems, preventive maintenance, data taking), as well as registered faults of detector and accelerator systems are indicated in the reports.

15.5. Monitoring of the Detector Operation

Checking of status of the detector systems is performed with the help of a set of monitoring programs, being run on different computers of the experimental facility. In case of an arising of emergency situation, e.g., at overload of power supply sources or deviation of any parameter beyond the preset range, the monitoring programs send the message ALARM to the system. The latter writes the information on the arisen event into the logbook in the database and issues an audible signal appropriate to the event. Signaling relating to faults of a particular system can be turned off by the operator (e.g., when the detector system is switched off).

Control of serviceability of apparatus of the detector systems and variations in system parameters that are important for data processing is performed using the dedicated package of calibration programs. In the course of experiment, the calibration of systems is conducted once to twice a week in intervals between the data taking runs. The calibration results are stored in the database and used in reconstruction of the collected statistics.

15.6. Database

PostgreSQL [89] is used as DBMS for the KEDR detector database [88]. The selection of the standard non-specialized general-purpose relational DBMS for storing the experiment data has paid its way completely. The DBMS PostgreSQL proved to be sufficiently flexible and effective for satisfying the demands available. The presence of ready-to-use variant has

saved time (with another option would be spent for implementation of the dedicated DBMS), while its open architecture, in particular, allowed us to transfer to VAX/VMS the library providing interface for access to the database.

By summer 2012, a physical database volume was 31 GB, and the size of the compressed reserve copy was 6.6 GB. In all, for the time of existence of the KEDR detector database over ten million entries was made, which corresponds to nearly two billion numbers. A key to a standard entry is time, which makes it possible to correlate the entry with the run number, information on which is also introduced into the database simultaneously with the file writing. The slow control data are visualized through Web-interface.

In addition to the numerical information, binary and text objects can be also stored in the KEDR experiment database.

16. SIMULATION

For simulating the KEDR detector functioning, the KEDRSIM package of simulation programs was developed. It is created on the basis of the package GEANT 3.21 [90] and contains the detailed description of the detector material, as well as subprograms of signal digitization with consideration for peculiarities of functioning of the data acquisition system for each detector subsystem. A result of the package run is the data in the same format as in the experiment. Apart from this, the package provides recording the additional information on interactions of the particles produced in the detector with its material, which helps in analysis of experimental data.

The primary simulation (event generators) now includes more than 50 different generators of multiple productions of hadrons, the J/ψ , ψ' , $\psi(3770)$ decays, Bhabha scattering, production of $\tau^+\tau^-$ pairs, two-photon production of leptons and hadrons and some others.

To use simulation effectively in the analysis of experimental data, a bulk of events for simulation of basic processes is recorded into the simulation archives in the format of the KEDR raw data.

Based on the ROOT library of classes [91], an environment was developed for analysis of the experimental and simulation data and a program of events displaying during the accumulation of experimental data and their subsequent processing was written.

CONCLUSIONS

The KEDR detector has been conducting from 2002 a regular data taking on the VEPP-4M collider. For the time elapsed, a large series of precision measurements is performed, which improved appreciably the accuracy of parameters of particles in the PDG tables. Among them are measurements of masses, total

and lepton widths of ψ mesons [92, 94, 97, 98], measurement of the τ lepton mass [93], measurement of masses of the charged and neutral D mesons [95], as well as search for narrow resonances in the regions $2E = 2.95\text{--}3.1$ GeV [96].

ACKNOWLEDGMENTS

We thank many workers of the BINP for their assistance in designing, constructing the KEDR detector, and in ensuring the long-term successful detector functioning. We are grateful to Italian physicists from Dipartimento di Fisica dell'Università and Sezione INFN (Milan), from Dipartimento di Fisica dell'Università and Sezione INFN (Bologna), from Dipartimento di Elettronica Università di Pavia and Sezione INFN (Milan) for their participation in the development and fabrication of a unique liquid krypton calorimeter of the KEDR detector.

This work was supported by the Ministry of Education and Science of the Russian Federation, Siberian Branch of the Russian Academy of Sciences (Integration projects no. 100 and 103), by the Russian Foundation for Basic Research (grants 10-02-00871-a, 10-02000904-a, 11-02-00558-a, 11-02-01064-a, 12-02-00023-a), and by grants of the Russian Federation President for Leading Scientific Schools (NSh-6943.2010.2 and NSh-5320.2012.2).

REFERENCES

1. V. V. Anashin, et al., "Status of the KEDR detector," Nucl. Instrum. Methods Phys. Res., A **478**, 420–425 (2002).
2. V. V. Anashin, et al., Preprint No. IYaF 2010-40 (Budker Inst. of Nuclear Physics, Siberian Branch, Russian Academy of Sciences, Novosibirsk, 2010). <http://www.inp.nsk.su/activity/preprints/index.ru.shtml>
3. V. Petrov, "Status of the VEPP-4M electron-positron collider," in *Proceedings of the 4th Asian Particle Accelerator Conference*, (Indore, India, 2007), pp. 112–114. <http://cern.ch/AccelConf/a07/PAPERS/TUPMA008.PDF>
4. V. Smalyuk, "Status of the VEPP-4M collider at BINP," in *Proceedings of XXI Russian Particle Accelerator Conference*, (Zvenigorod, Russia, 2008), pp. 79–81. <http://cern.ch/AccelConf/r08/papers/MOBAU03.pdf>
5. A. N. Aleshaev, et al., Preprint No. IYaF 2011-20 (Budker Inst. of Nuclear Physics, Siberian Branch, Russian Academy of Sciences, Novosibirsk, 2011). <http://www.inp.nsk.su/activity/preprints/index.ru.shtml>
6. A. D. Bukin, et al., "Absolute calibration of beam energy in the storage ring. Phi-meson mass measurement," in *Proceedings of V International Symposium on High Energy Physics and Elementary Particle Physics*, (Warsaw, 1975), pp. 138–162.
7. V. E. Blinov, et al., "Review of beam energy measurements at VEPP-4M collider: KEDR/VEPP-4M," Nucl. Instrum. Methods Phys. Res., A **598**, 23–30 (2009).
8. N. Nakamura, et al., "The review of particle physics," Journal of Physics G **37**, 075021 (2010).
9. A. A. Sokolov and I. M. Ternov, "On polarization and spin effects in the theory of synchrotron radiation," Dokl. Akad. Nauk SSSR **153**, 1052–1054 (1963).
10. A. E. Bondar, et al., "Polarization measurement in storage rings of the Institute of Nuclear Physics (Novosibirsk)," in *Proceedings of 12th International Conference on High Energy Accelerators*, (Fermilab, Batavia, Illinois, 1983), pp. 240–243.
11. O. V. Anchugov, et al., "Application of accelerator physics methods in experiments for precision measurement of particle masses at the VEPP-4 facility with KEDR detector," Prib. Tekh. Eksp., No.1, 20–33 (2010).
12. V. N. Baier, V. M. Katkov, and V. M. Strakhovenko, "On polarization influence on effects of internal scattering of electrons in storage rings," Dokl. Akad. Nauk SSSR **241**, 797–800 (1978).
13. S. A. Nikitin and I. B. Nikolaev, Preprint No. IYaF 2010-42 (Budker Inst. of Nuclear Physics, Siberian Branch, Russian Academy of Sciences, Novosibirsk, 2010). <http://www.inp.nsk.su/activity/preprints/index.ru.shtml>
14. N. I. Zinevich and E. I. Shubin, Preprint No. IYaF SO AN SSSR 84-11 (Budker Inst. of Nuclear Physics, Siberian Branch, Russian Academy of Sciences, Novosibirsk, 1984).
15. Ya. S. Derbenev, A. M. Kondratenko, and A. N. Skrinsky, "Radiative Polarization at Ultra-High Energies," Part. Acc. **9**, 247–265 (1979).
16. S. A. Nikitin, Preprint No. IYaF 2005-54 (Budker Inst. of Nuclear Physics, Siberian Branch, Russian Academy of Sciences, Novosibirsk, 2005). <http://www.inp.nsk.su/activity/preprints/index.ru.shtml>
17. R. Klein, et al., "Measurement of the BESSY II electron beam energy by Compton-backscattering of laser photons," Nucl. Instrum. Meth. A **486**, 545–551 (2002).
18. N. Yu. Muchnoi, et al., "Fast and precise beam energy monitor based on the Compton backscattering at the VEPP-4M collider," in *Proceedings of 10th European Particle Accelerator Conference (EPAC 06)*, (Edinburgh, Scotland, 2006), pp. 1181–1183.
19. S. G. Pivovarov, Candidate's Dissertation in Physics and Mathematics (Budker Inst. of Nuclear Physics, Novosibirsk, 2001).
20. A. Dubrovin, *Mermaid user's guide* (Novosibirsk, 1994).
21. P. N. Evtushenko, A. I. Rogozin, and Yu. A. Tikhonov, Preprint No. IYaF 99-3 (Budker Inst. of Nuclear Physics, Siberian Branch, Russian Academy of Sciences, Novosibirsk, 1999). <http://www.inp.nsk.su/activity/preprints/index.ru.shtml>
22. *Cryogenic support system of the KEDR detector STAG-1200/120-120/4,5. Technical specifications 2082 364215 1017 00 2 TO* (NPO Kriogenmash, 1991) [in Russian].
23. V. Aulchenko, et al., "Vertex chamber for the KEDR detector," Nucl. Instrum. Methods Phys. Res., A **283**, 528–531 (1989).
24. V. P. Nagaslaev, Candidate's Dissertation in Physics and Mathematics (Budker Inst. of Nuclear Physics, Novosibirsk, 1997).

25. B. O. Baibusinov, et al., Preprint No. IYaF 97-68 (Budker Inst. of Nuclear Physics, Siberian Branch, Russian Academy of Sciences, Novosibirsk, 1997). <http://www.inp.nsk.su/activity/preprints/index.ru.shtml>
26. E. M. Baldin, et al., Preprint No. IYaF 2000-005 (Budker Inst. of Nuclear Physics, Siberian Branch, Russian Academy of Sciences, Novosibirsk, 2000). <http://www.inp.nsk.su/activity/preprints/index.ru.shtml>
27. V. M. Aulchenko, et al., "Data acquisition systems and triggers for the detectors in INP," Nucl. Instrum. Methods Phys. Res., A **409**, 639–642 (1998).
28. V. V. Anashin, et al., "Project of the KEDR detector," in *Proceedings of International Symposium on Coordinate Detectors in High Energy Physics*, (Dubna, 1988), pp. 58–66 [in Russian].
29. V. V. Anashin, et al., *KEDR status report No. RX-1308* (Novosibirsk, 1990).
30. S. E. Baru, et al., "The KEDR drift chamber," in *Proceedings of Fifth International Conference on Instrumentation for Colliding Beam Physics*, (Novosibirsk, 1990), pp. 41–42.
31. S. E. Baru, et al., "The KEDR drift chamber," Nucl. Instrum. Methods Phys. Res., A **323**, 151–156 (1992).
32. S. E. Baru, et al., "Status of the KEDR drift chamber," Nucl. Instrum. Methods Phys. Res., A **379**, 417–420 (1996).
33. S. E. Baru, et al., "The KEDR drift chamber based on dimethyl ether," Nucl. Instrum. Methods Phys. Res., A **409**, 23–25 (1998).
34. S. E. Baru, et al., "Status of the KEDR drift chamber," Nucl. Instrum. Methods Phys. Res., A **494**, 251–254 (2002).
35. SLD Design Report, SLAC-Report-373 (1984) and updates; W. B. Atwood, et al., Performance of the SLD central drift chamber prototype, Nucl. Instrum. Methods Phys. Res., A **252**, 295 (1986).
36. V. M. Aul'chenko, S. E. Baru, and G. A. Savinov, Preprint No. IYaF 88-29 (Budker Inst. of Nuclear Physics, Siberian Branch, Russian Academy of Sciences, Novosibirsk, 1988).
37. A. P. Onuchin, et al., "The aerogel Cherenkov counters with wavelength shifters and phototubes," Nucl. Instrum. Methods Phys. Res., A **315**, 517–520 (1992).
38. M. Yu. Barnyakov, et al., "Aerogel Cherenkov counters for the KEDR detector," Nucl. Instrum. Methods Phys. Res., A **453**, 326–332 (2000).
39. A. Yu. Barnyakov, et al., "The status of the KEDR ASHIPH system," Nucl. Instrum. Methods Phys. Res., A **518**, 597–601 (2004).
40. A. R. Buzykaev, et al., "Project of aerogel Cherenkov counters for KEDR," Nucl. Instrum. Methods Phys. Res., A **379**, 453 (1996).
41. A. F. Danilyuk, et al., "Recent results on aerogel development for use in Cherenkov counters," Nucl. Instrum. Methods Phys. Res., A **494**, 491–494 (2002).
42. M. Yu. Barnyakov, et al., "Development of aerogel Cherenkov counters with wavelength shifters and phototubes," Nucl. Instrum. Methods Phys. Res., A **419**, 584–589 (1998).
43. A. Yu. Barnyakov, et al., "R&D of microchannel plate phototubes," Nucl. Instrum. Methods Phys. Res., A **567**, 17–20 (2006).
44. A. R. Buzykaev, et al., "Aerogel Cherenkov counters with wavelength shifters and micro-channel plate photo-tubes," Journal of Non-Crystalline Solids **225**, 381–384 (1998).
45. A. Yu. Barnyakov, et al., "Test of aerogel counters for the KEDR detector," Nucl. Instrum. Methods Phys. Res., A **478**, 353–356 (2002).
46. M. E. Globus and B. V. Grinev, *Nonorganic scintillators. New and traditional materials* (Akta, Kharkov, 2000) [in Russian].
47. V. M. Aulchenko, et al., "Experience with CsI(Na) crystals for calorimetry," Nucl. Instrum. Methods Phys. Res., A **379**, 502–504 (1996).
48. V. M. Aulchenko, et al., "CsI calorimeters for KEDR and CMD-2 detectors," in *Proceedings of 5th International Conference on Instrumentation for Colliding Beam Physics*, (Novosibirsk, 1990), pp. 318–330.
49. D. N. Grigoriev, et al., "Study of a calorimeter elements consisting of a CsI(Na) crystal and phototriode," Nucl. Instrum. Methods Phys. Res., A **378**, 353–355 (1996).
50. M. P. Bes'chastnov, et al., "The results of vacuum phototriodes tests," Nucl. Instrum. Methods Phys. Res., A **342**, 477–482 (1994).
51. V. M. Aul'chenko, L. A. Leont'ev, and Yu. V. Usov, Preprint No. IYaF 88-30 (Budker Inst. of Nuclear Physics, Siberian Branch, Russian Academy of Sciences, Novosibirsk, 1988).
52. S. E. Baru, et al., Preprint No. 88-26, IYaF (Budker Inst. of Nuclear Physics, Siberian Branch, Russian Academy of Sciences, Novosibirsk, 1988).
53. V. M. Aulchenko, et al., "Investigation of the electromagnetic calorimeter based on liquid krypton," Nucl. Instrum. Methods Phys. Res., A **289**, 468–474 (1990).
54. V. M. Aulchenko, et al., "Liquid krypton calorimeter for KEDR detector," Nucl. Instrum. Methods Phys. Res., A **316**, 8–13 (1992).
55. V. M. Aulchenko, et al., "Liquid krypton electromagnetic calorimeter," Nucl. Instrum. Methods Phys. Res., A **327**, 194–198 (1993).
56. V. M. Aulchenko, et al., "Development of the liquid krypton EM calorimeter of KEDR detector," in *Proceedings of the Third Conference on Calorimetry in High Energy Physics* (Batavia, Illinois, 1990), pp. 233–242.
57. P. Antoni, et al., "Space and energy resolutions in a liquid krypton E.M. calorimeter," Nucl. Instrum. Methods Phys. Res., A **315**, 491–493 (1992).
58. V. M. Aul'chenko, et al., Preprint No. IYaF 2004-29 (Budker Inst. of Nuclear Physics, Siberian Branch, Russian Academy of Sciences, Novosibirsk, 2004). <http://www.inp.nsk.su/activity/preprints/index.ru.shtml>
59. V. M. Aulchenko, et al., "The test of the LKr calorimeter prototype at the tagged photon beam," Nucl. Instrum. Methods Phys. Res., A **394**, 35–45 (1997).
60. V. M. Aul'chenko, et al., Preprint No. IYaF 85-122, (Budker Inst. of Nuclear Physics, Siberian Branch, Russian Academy of Sciences, Novosibirsk, 1985). <http://www.inp.nsk.su/activity/preprints/index.ru.shtml>
61. V. Aulchenko, et al., "Muon system based on streamer tubes with time difference readout," Nucl. Instrum. Methods Phys. Res., A **265**, 137–140 (1988).
62. V. M. Aul'chenko, et al., Preprint No. IYaF 2000-48 (Budker Inst. of Nuclear Physics, Siberian Branch, Rus-

- sian Academy of Sciences, Novosibirsk, 2000). <http://www.inp.nsk.su/activity/preprints/index.ru.shtml>
63. G. D. Alekseev, V. V. Kruglov, and D. M. Khazins, "Self-quenching streamer discharge in a wire chamber," *Fiz. Elem. Chastits At. Yadra* **13** (3), 701 (1982).
 64. V. M. Aul'chenko, B. O. Baibusinov, V. M. Titov, Preprint No. IYaF 88-22 (Budker Inst. of Nuclear Physics, Siberian Branch, Russian Academy of Sciences, Novosibirsk, 1988).
 65. G. Altarelli and F. Buccella, "Single photon emission in high-energy e^+e^- collisions," *Nuovo Cimento A* **34** (5), 1337–1346 (1964).
 66. V. N. Baier, V. S. Fadin, and V. A. Khoze, "On bremsstrahlung of photons at collisions of high energy electrons," *Zh. Eksp. Teor. Fiz.* **51** (4), 1135–1142 (1966).
 67. A. E. Blinov, et al., "Large impact parameters cut-off in the process $e^+e^- \rightarrow e^+e^-\gamma$," *Phys. Lett. B* **113**, 432 (1982).
 68. V. N. Baier, V. M. Katkov, and V. M. Strakhovenko, "A role of geometric factors in the process of bremsstrahlung on colliding e^+e^- beams," *Yad. Fiz.* **36**, 163 (1982).
 69. V. A. Tayurskii, Preprint No. IYaF 2008-35 (Budker Inst. of Nuclear Physics, Siberian Branch, Russian Academy of Sciences, Novosibirsk, 2008). <http://www.inp.nsk.su/activity/preprints/index.ru.shtml>
 70. V. M. Budnev, et al., "The two-photon particle production mechanism. Physical problems. Applications. Equivalent photon approximation," *Phys. Rep.* **15**, 181–282 (1975).
 71. S. J. Brodsky, "Exclusive photon-photon processes," in *Proceedings of XI International Workshop on Gamma-Gamma Collisions*, (Egmond Aan Zee, Netherlands, 1997), p. 197. E-Print: hep-ph/9707444.
 72. D. Urner, "Review of two photon interactions," in *Intersections of Particle and Nuclear Physics: 8th Conference CIPANP2003*, (AIP Conference Proc., 2004), Vol. 698, pp. 566–570. E-Print: hep-ex/0309045.
 73. S. E. Baru, et al., "Experiments with the MD-1 detector at the e^+e^- collider VEPP-4 in the energy region of Υ mesons," *Phys. Rep.* **267**, 71–159 (1996).
 74. V. M. Aul'chenko, et al., Preprint No. IYaF 91-49 (Budker Inst. of Nuclear Physics, Siberian Branch, Russian Academy of Sciences, Novosibirsk, 1991).
 75. A. E. Bondar', Candidate's Dissertation in Physics and Mathematics (Budker Inst. of Nuclear Physics. Novosibirsk, 1994).
 76. F. Sauli, "GEM: A new concept for electron amplification in gas detectors," *Nucl. Instrum. Methods Phys. Res., A* **386**, 531–534 (1997).
 77. V. M. Aulchenko, et al., "Upgrade of the KEDR tagging system," *Nucl. Instrum. Methods Phys. Res., A* **494**, 241–245 (2002).
 78. V. M. Aulchenko, et al., "Triple-GEM detectors for KEDR tagging system," *Nucl. Instrum. Methods Phys. Res., A* **598**, 112–115 (2009).
 79. V. M. Aulchenko, et al., "Operation of the triple-GEM detectors in the tagging system of the KEDR experiment on the VEPP-4M collider," *J. of Instr.* **6**, 07001 (2011).
 80. V. M. Aulchenko, et al., "Study of the BELLE CsI calorimeter prototype with the BINP Tagged Photon Beam," *Nucl. Instrum. Methods Phys. Res., A* **379**, 491–494 (1996).
 81. H. S. Ahn, et al., "Study of characteristics of the BELLE CsI calorimeter prototype with a BINP tagged photon beam," *Nucl. Instrum. Methods Phys. Res., A* **410**, 179–194 (1998).
 82. H. Ikeda, et al., "A detailed test of the CsI(TL) calorimeter for BELLE with photon beams of energy between 20 MeV and 5.4 GeV," *Nucl. Instrum. Methods Phys. Res., A* **441**, 401–426.
 83. Sh. Zh. Akhmadaliev, et al., "Delbruck scattering at energies of 140–450 MeV," *Phys. Rev. C* **58**, 2844–2850 (1998).
 84. Sh. Zh. Akhmadaliev, et al., "Experimental investigation of high-energy photon splitting in atomic fields," *Phys. Rev. Lett.* **89**, 061802 (2002), e-Print: hep-ex/0111084.
 85. S. E. Baru, et al., "Trigger of the KEDR detector," *Instr. and Exp. Techn.* **54**, 335–349 (2011).
 86. bzip2. <http://bzip.org>
 87. Oracle grid engine. <http://www.oracle.com/us/products/tools/oracle-grid-engine-075549.html>
 88. E. M. Baldin, Candidate's Dissertation in Physics and Mathematics (Budker Inst. of Nuclear Physics, Novosibirsk, 2010).
 89. PostgreSQL. <http://www.postgresql.org/>
 90. R. Brun, et al., *GEANT 3.21, detector description and simulation tool* (CERN Program Library Long Writeup, W5013. CERN. Geneva, 1993).
 91. R. Brun and F. Rademakers, "ROOT: An object oriented data analysis framework," *Nucl. Instrum. Methods Phys. Res., A* **389**, 81–86 (1997).
 92. V. V. Anashin, et al., "Results on J/ψ , $\psi(2S)$, $\psi(3770)$ from KEDR," *Nuclear Physics B (Proc. Suppl.)* **181–182**, 353–357 (2008).
 93. V. V. Anashin, et al., "Tau mass measurement at KEDR," *Nuclear Physics B (Proc. Suppl.)* **189**, 21–23 (2009).
 94. V. V. Anashin, et al., "Measurement of $\Gamma_{ee}(J/\psi) * B(J/\psi \rightarrow e^+e^-)$ and $\Gamma_{ee}(J/\psi) * B(J/\psi \rightarrow \mu^+\mu^-)$," *Physics Lett. B* **685**, 134–140 (2010).
 95. V. V. Anashin, et al., "Measurement of D^0 and D^+ meson masses with the KEDR detector," *Phys. Lett. B* **686**, 84–90 (2010).
 96. V. V. Anashin, et al., "Search for narrow resonances in e^+e^- annihilation between 1.85 and 3.1 GeV with the KEDR detector," *Physics Lett. B* **703**, 543–546 (2011).
 97. V. V. Anashin, et al., "Measurement of main parameters of the $\psi(2S)$ resonance," *Phys. Lett. B* **711**, 280–291 (2012).
 98. V. V. Anashin, et al., "Measurement of $\psi(3770)$ parameters," *Phys. Lett. B* **711**, 292–300 (2012).

Translated by M.V. Samokhina